On the use of multiple high intensity laser pulses in ion acceleration experiments

Graeme Gordon Scott

Department of Physics

University of Strathclyde

A thesis submitted for the degree of

Doctor of Philosophy

2015

Declaration of authenticity and author's rights

This thesis is the result of the authors original research. It has been composed by the author and has not been previously submitted for examination which has led to the award of a degree.

Signed: 

Date: 23/07/15

Abstract

Compact laser driven ion sources have inspired cautious optimism that they may provide an alternative to conventional accelerators for existing applications, such as in medicine, or aid the realisation of new ones such as fusion energy. However, the sources must be developed, with increased conversion efficiency of laser to proton energy being high on the list of requirements. Recent reports in the literature have shown that record conversion efficiencies can be achieved with double pulse interactions, and this thesis proceeds with this theme.

The double pulse operation of the plasma mirror is characterised for the first time, in terms of the post interaction far field quality, and integrated reflectivity. The main pulse reflectivity is significantly enhanced to 96 % and the far field remains of high optical quality up to five picoseconds after the prepulse interaction, within the regime for conversion efficiency enhancement. These observations are explained by perturbations of the quasi-near field intensity distribution seeding nonuniformities in the plasma expansion of the plasma mirror surface.

A novel plasma half cavity target geometry is investigated which utilises the high fraction of laser energy reflected from an ionised surface and refocuses it such that a double pulse interaction is attained. This new geometry is found to double the laser to proton energy conversion efficiency, compared with planar foil interactions and to modify the low energy region of the proton spectrum.

For pulse separations of tens of picoseconds, a long time delay regime is identified for planar foil interactions, where a significant reduction in maximum proton energy and conversion efficiency is reversed, and return to that expected for single pulse interactions. This is explained by the main pulse interacting with bulk target expansion induced by the prepulse. Increased electron temperatures from enhanced absorption in the preplasma are found to mitigate the detrimental effects on ion acceleration, associated with rear surface density scale lengths.

Role of the Author

Throughout this PhD study, the author gained experience in the design, implementation and leadership of experimental campaigns on several of the highest powered laser systems in Europe. Primarily, the author's own work involved use of the PHELIX laser at the GSI facility, but also engaged in collaborations at the Central Laser Facility using the Vulcan and Astra-Gemini lasers, which have resulted in some of the publications listed on pages v-vi.

Chapter 4: The experimental setup was devised by V. Bagnoud and B. Zielbauer of the PHELIX group. The author, with previous experience of fielding plasma mirrors at the facility, was involved in the collaboration to characterise the single pulse operation of the plasma mirror interaction and played a significant role in the accomplishment of this experimental work.

The author recognised the opportunity to adapt the setup to characterise the plasma mirror double pulse interaction. The author led the implementation and direction of this experimental investigation.

The data analysis and interpretation that features in this chapter was carried out by the author, which is being prepared for peer review.

Chapter 5: The author played a significant role in the planning of this experimental campaign with major assistance from J.S. Green. The author also played a significant role in the implementation of the experiment and the fielding of diagnostics. The complex target alignment was performed by D.C. Carroll and J.S. Green while the author gained experience in these experimental methods.

Prior to experimental investigation, the author carried out predictive PIC modelling in order to estimate the dimensions of interest for the cavity. The expertise of the Target Fabrication Group of the Central Laser Facility was crucial for manufacturing these targets, the concept of which was devised by D. Neely.

Experimental data analysis was carried out by the author, as well as the

particle in cell modelling and interpretation. This led to the work being submitted for peer review in *Applied Physics Letters*. The author drafted this work and led correspondence with editors, leading to its successful publication.

Chapter 6: The author played an advanced role in this work from conception data analysis. With major assistance from D. Neely, the author was involved in identifying objectives and drafting of an experimental proposal for competitive access to facility time. Much of the detailed planning and logistics of the experiment were taken care of by the author with assistance from J.S. Green.

The author took a leading role in coordinating a small team in the implementation of the experiment. The author also played a leading role in making the major decisions with regard to the direction of the experimental work within the framework of achieving the goals set out in the experimental proposal.

The data analysis, PIC simulation and interpretation that features in this chapter is the work of the author.

Offline, the author dedicated time to diagnostic development, and a technique of increasing the dynamic range of radiochromic film by scanning in the ultraviolet region of the spectrum is described in chapter 3, which was successfully published in *Physica Medica*. The author also used the University of Birmingham cyclotron proton beam to calibrate the radiochromic film for use in the experiments described in this thesis, with major assistance from J.S. Green, F. Fiorini, D. Parker and S. Green.

Publications

Multi-pulse enhanced laser ion acceleration using plasma half cavity targets. GG Scott, JS Green, V Bagnoud, C Brabetz, CM Brenner, DC Carroll, DA MacLellan, APL Robinson, M Roth, C Spindloe, F Wagner, B Zielbauer and P McKenna and D Neely. *Applied physics letters*, **101**(2), 024101 (2012).

Optimisation of plasma mirror reflectivity and optical quality using double laser pulses. GG Scott, V Bagnoud, C Brabetz, RJ Clarke, JS Green, RI Heathcote, HW Powell, B Zielbauer, TD Arber and P McKenna and D Neely. *New journal of physics*, **17**, 033027, (2015).

Fast electron transport patterns in intense laser-irradiated solids diagnosed by modeling measured multi-MeV proton beams. DA MacLellan, DC Carroll, RJ Gray, N Booth, B Gonzalez-Izquierdo, HW Powell, GG Scott, D Neely and P McKenna. *Laser and particle beams*, **31**(3), 475 (2013).

Annular fast electron transport in silicon arising from low temperature resistivity. DA MacLellan, DC Carroll, RJ Gray, N Booth, M Burza, MP Desjarlais, F Du, B Gonzalez-Izquierdo, D Neely, HW Powell, APL Robinson, DR Rusby, GG Scott, XH Yuan, CG Wahlström and P McKenna. *Physical review letters*, **111**(9), 095001 (2013).

Instrumentation for diagnostics and control of laser-accelerated proton (ion) beams. PR Bolton, M Borghesi, CM Brenner, DC Carroll, C De Martinis, A Flacco, V Floquet, J Fuchs, P Gallegos, D Giove, JS Green, S Green, B Jones, D Kirby, P McKenna, D Neely, F Nuesslin, R Prasad, S Reinhardt, M Roth, U Schramm, GG Scott, S Ter-Avetisyan, M Tolley, G Turchetti, JJ Wilkens. *Physica medica*, **30**(3), 255 (2014).

Investigation of terahertz radiation production from intense laser-solid interactions. XH Yuan, Y Fan, DC Carroll, DA MacLellan, F Du, N Booth, M Burza, M Chen, RJ Gray, YK Jin, YT Li, Y Liu, D Neely, HW Powell, GG Scott, C-G Wahlström, J Zhang, P McKenna and ZM Sheng. *High Power Laser Science and Engineering*, **2**, e5 (2014).

Azimuthal asymmetry in collective electron dynamics in relativistically transparent laser-foil interactions. RJ Gray, DA MacLellan, B Gonzalez Izquierdo, HW Powell, DC Carroll, CD Murphy, L Stockhausen, DR Rusby, GG Scott, R Wilson, N Booth, DR Symes, SJ Hawkes, R Torres, M Borghesi, D Neely and P McKenna. *New journal of physics*, **16**, 093027 (2014).

Tunable mega-ampere electron current propagation in solids by dynamic control of lattice melt. DA MacLellan, DC Carroll, RJ Gray, N Booth, M Burza, MP Desjarlais, F Du, D Neely, HW Powell, APL Robinson, GG Scott, XH Yuan, CG Wahlström and P McKenna. *Physical review letters*, **113**, 185001 (2014).

Buffered spectrally-peaked proton beams in the relativistic transparency regime. NP Dover, MJV Streeter, CAJ Palmer, H Ahmed, B Albertazzi, M Borghesi, DC Carroll, J Fuchs, R Heathcote, P Hilz, KF Kakolee, S Kar, R Kodama, A Kon, DA MacLellan, P McKenna, RJ Gray, SR Nagel, M Nakatsutsumi, D Neely, MM Notley, R Prasad, GG Scott, M Tampo, M Zepf, J Schreiber and Z Najmudin. *CoRR*, 1406.3540, (2015). (*In review*).

Measurement of the angle, temperature and flux of fast electrons emitted from intense laser-solid interactions. DR Rusby, L Wilson, RJ Gray, R Dance, N Butler, DA MacLellan, GG Scott, V Bagnoud, B Zielbauer, P McKenna and D Neely. (2015). (*In review*).

Role of lattice structure and low temperature resistivity on fast electron beam filamentation in carbon. RJ Dance, NMH Butler, RJ Gray, DA MacLellan, DR Rusby, GG Scott, B Zielbauer, V Bagnoud, H Xu, APL Robinson, MP Desjarlais, D Neely and P McKenna. (2015). (*In review*).

Utilising proton and x-ray beams from laser-solid interactions for applications. CM Brenner, GG Scott, S Mirfayzi, DR Rusby, C Armstrong, L Wilson, A McClymont, M Notley, R Clarke, P Oliver, A Higginson, N Butler, A Alejo, H Ahmed, C Murphy, S Kar, P McKenna, R Allott, C Hernandez-Gomez, V Bagnoud, B Zielbauer, H Powell, R Heathcote, B Gonzalez-Izquierdo and D Neely. (2015). (*In review*).

Acknowledgements

```
all = (family,friends,colleagues);
for i =1:(length(all(:)));
    acknowledgement = ['Thankyou ' all(i) '!'];
    disp(acknowledgement);
end
```

With the number of people that have helped me over the past years, its near impossible to thank you all in these pages, but I hope that in knowing you appear at least once in my acknowledgement routine, my virtual thanks will be enough!

At risk of achieving the opposite effect by leaving this section insultingly brief, there are of course some people without which I could never have achieved this.

I'll be eternally grateful to my supervisor David, for allowing me to pursue my own research path and having the patience to let me dwell on topics for longer than others might have. I'm certain that David appreciated more than me how much longer and windy these paths would be, but this taught me many important lessons on navigating the uncharted world of research, as well as giving me ample opportunity to go off on the odd tangent. David's metaphors and fables have been a constant source of amusement and motivation in equal measures and some of them will live with (and some will haunt) me forever! His analogies show the unbelievable depth to which he appreciates physics in general and inspires me to reach a level where it seems this simple to me. Given the chance I'll always try to step back from a problem and wonder, '*Can I ask a silly question?*'.

Since first speaking with Paul, his drive and vision was something that I knew I wanted to be a part of, and I'm glad that I had the opportunity. Although, supervising from such a distance, his ability to seamlessly integrate with discussions on my work and progress was extraordinary. I was always gratefully for the

strong insights that this perspective allowed him to observe and for the resultant advice and wisdom he's offered. I also know Paul has been operating in the background, shielding me from many a thankless chore to ensure things run smoothly with my external placement.

When I arrived I was lucky to join an experienced and level headed group in James Green, David Carroll, Ceri Brenner and Rob Clarke, who gave me swathes of assistance in doing much of my early work, and without them most of my early research would not have happened. I learned a huge amount about the field from them but they are also model scientists in their openness to discussing new ideas and approaches, and I've always tried to implement their positive traits into my own approach.

Our group has recently been complimented with the addition of Dean and Lucy, and I know the hard work ethic involved in ensuring no award of the 'Slacker of the day' trophy, will keep our group a productive and fun place to work. I look forward to continuing to work with them over the years to come, as I do with our extended group at Strathclyde, although it'll be poorer for lacking Haydn, the other half of the Quality Polis, although I know that the guys remaining are more than capable of maintaining his spirit.

Our neighbouring plasma physics department has majorly contributed to my development, the doctoral training sessions affectionately branded *Hard Sums* by Alex Robinson, in particular has been invaluable in providing me with a much more developed theoretical understanding of plasma physics. Raoul's unwavering patience in explaining some of the subtleties of all things PIC code, Linux and discussion on whether $\sum_{n=1}^{\infty} n = -\frac{1}{12}$, or not, has been a particular pleasure. On the coding front, the Dr. Scott on the other side of my corridor, Robbie, has given me much appreciated advice and assistance, as has Chris Brady from the other side of a barrage of emails.

Everyone at the CLF in general has given me plenty of help with just about every facet of my work, the target area staff, target fabrication, design, electrical and mechanical engineering, as well as being a thoroughly helpful and friendly

bunch of people to work with and its been a pleasure to work in this environment.

The PHELIX laser, where most of my experimental work was carried out, was virtually a second home and the staff there made it feel like one too. None more so than Bernhard, whose assistance and friendship was not only confined to the lab, but which extended to evening meals out, weekend trips and an all hours taxi service, made our stay feel like a holiday. I'll always be grateful for the hospitality I received in Germany, also from Vincent, Florian, Christian and Alex and will always look forward to going back.

It's not only my colleagues that I have to thank, but some close friends have kept me sane through the process, not to say that everyone I've mentioned previously doesn't fit into this category too. With Dan and Steve, its been a blur of the Three Geeks Challenge, the odd beer festival, Town Ultras and teapots and I look forward to it continuing. The Prince of Wales pub quiz has been a regular fixture of ours, that's been a constant highlight of the week with everyone involved with the team, whose name I advisedly abbreviate to QOMF for the purpose of this publication...

Its a pleasure that I've managed to keep touch with my longest standing croney, Stuart. Being a chemist, he gives me an retreat to get my mind well away from science (sorry!) and onto important things like losing all my money on *certainties* at Cheltenham. Many of the stories I have involving him would be too risky for a best man's speech, so I'll leave it at that here, but its been a laugh as always.

To my many long existing friends and new ones I've found along the way, including all the '05 uni gang and Javier to name a few, cheers!

My Mum is probably the only person that has any idea of the ups and downs I went through over the course of this PhD. As it turns out, a sound bit of auld Ayrshire advice can, on occasion, trump the popular wisdom of a national laboratory, and without her on the end of a phone nearly four hundred miles away, I don't know if I would have made it to the end.

My Nanna and Pappa have been a constant rock and have given me a huge ammount of support over the years. My Pappa is where the brains of the family come from, and as I like to tell my Mum, it skips a generation. I'm hoping to get up to watch Killie with him a bit more often now.

I think Eddie has a fair bit to answer for, as far as the existence of this thesis goes. He always tried got me interested in nature and how things work, but I fear after the encounter with the wasps nest I was always going to opt for the more sterile environment of a steel and aluminium lab as opposed to the biology route.

Having a big family, I'm very lucky as despite my generally awful record at keeping in touch, there's always somebody keeping in touch with me, which I hugely appreciate. Its always great to see you all when I get the chance to come back up the road, and I'm hoping that will be far more regularly than it has been up until now. Thanks David, Amy and Allan, Charlie, Gavin, Shirley and Dad. There's no preferential listing there, welcome to an academic author list, the auld yins go at the end and the rest pretty much in alphabetical order. In future references you'll need to be abbreviated to *David et al.*, but that's just how it goes.

To the rest of my extended family, who are far too numerous to mention here while keeping my publication charge finite, thanks to you all.

In its entirety, I dedicate this thesis to my Mum, Elizabeth Rogers.

Nobody will ever do more for me or mean as much.

Contents

List of figures

List of tables

Symbols used

Greek

$\delta\tau$	time delay *p. 85*
δx	perturbation height *p. 72*
δ_s	skin depth *p. 17*
ϵ_0	permittivity of free space *p. 12*
η	refractive index *p. 26*
η_2	nonlinear refractive index *p. 40*
γ	Lorentz factor *p. 17*
γ_K	Keldysh parameter *p. 14*
λ	wavelength *p. 18*
λ_D	Debye length *p. 15*
$\ln\Lambda$	Coulomb logarithm *p. 14*
μ_0	permeability of free space *p. 16*
∇	$\hat{x}\frac{\partial}{\partial x} + \hat{y}\frac{\partial}{\partial y} + \hat{z}\frac{\partial}{\partial z}$ *p. 16*
ν	collision frequency *p. 20*
ω	angular frequency *p. 12*
ϕ	potential *p. 13*
π	Euclidean circle circumference to diameter ratio *p. 12*
ρ	charge density *p. 16*
σ_x	standard deviation in perturbation height *p. 72*
τ	duration *p. 14*
τ_M	Mora model time scaling factor *p. 31*
θ_i	angle of incidence *p. 21*
φ	phase *p. 72*
ξ	Denisov function *p. 22*

Roman

a_0	normalised vector potential *p. 18*
a_B	Bohr radius *p. 12*
B	magnetic field *p. 17*
$B_\int$	B integral *p. 40*
c	*celeritas lucis p. 6*
$C(f)$	Vlasov - Fokker - Planck collision operator *p. 58*

c_s ion sound speed *p. 30*

E electric field *p. 16*

E energy *p. 6*

e elementary charge *p. 12*

e_N Euler's number *p. 12*

F combined reflected energy fraction *p. 85*

F force *p. 16*

f fraction *p. 21*

$f/\#$ focal length to diameter ratio *p. 44*

f_{VFP} Vlasov - Fokker - Planck distribution function *p. 58*

h Planck's constant *p. 12*

I intensity *p. 13*

i imaginary unit *p. 17*

j current density *p. 16*

K kinetic energy *p. 12*

k wave vector *p. 16*

k_B Boltzmann's constant *p. 15*

l_{ss} scale length *p. 20*

m mass *p. 6*

n number density *p. 14*

n_q principle quantum number *p. 127*

OD optical density *p. 47*

P pressure *p. 30*

p momentum *p. 17*

P_{crit} critical power *p. 26*

q charge *p. 17*

R reflected energy fraction *p. 67*

r radius *p. 85*

R_∞ Rydberg constant *p. 127*

T temperature *p. 14*

t time *p. 16*

U potential energy *p. 12*

v velocity *p. 17*

x, y, z Cartesian coordinate *p. 16*

Z atomic number *p. 14*

Z^* effective charge state *p. 20*

Special

$\hbar$ $\frac{h}{2\pi}$ *p. 12*

$\mathscr{I}$ specularly reflected intensity *p. 72*

$\mathscr{R}$ Rayleigh criteria *p. 72*

Subscripts

0	initial/unperturbed *p. 15*
a	atomic *p. 13*
abs	absorbed *p. 21*
c	cold *p. 124*
cal	calorimeter *p. 67*
coh	coherent *p. 72*
$coll$	collision *p. 14*
$crit$	critical *p. 17*
e	electron *p. 12*
eff	effective *p. 74*
g	grid *p. 58*
h	hot electron *p. 29*
i	ion *p. 20*
ib	inverse Bremsstrahlung *p. 74*
inc	incident *p. 67*
ion	ionisation pulse *p. 67*
$ionis$	ionisation *p. 12*
l	laser *p. 12*
m	melting *p. 116*
osc	oscillatory *p. 18*
p	plasma *p. 16*
$pond$	ponderomotive *p. 19*
$probe$	probe pulse *p. 67*
res	resonant absorption *p. 74*
s	shock *p. 116*
$targ$	target *p. 47*
$trans$	transmitted *p. 47*
x, y, z	Cartesian coordinate *p. 21*

Chapter 1

Introduction

In his annual presidential address to the Royal Society, as well as championing the increased uptake of peer reviewed publication in the Society's journal, Ernest Rutherford challenged the academic community to advance the emerging technology of high electromagnetic field production. Rutherford's hope was that manipulation of these high fields could lead to the realisation of high energy particle acceleration, that could be used to further probe the atomic nucleus, the discovery of which had earned him the Nobel prize in 1908. He also knew that this would open the door to many fields of research that he had not yet foreseen.

> *It has long been my ambition to have available for study a copious supply of atoms and electrons which have an individual energy far transcending that of the α and β-particles from radioactive bodies.*
>
> - Ernest Rutherford, 1927 [1].

Appropriately, the Rutherford Appleton Laboratory, where the bulk of my PhD studies have been spent, is named after Rutherford himself, and has its foundations in researching high energy proton acceleration by linear accelerators. The Central Laser Facility was later established at the site in 1975, with laser fusion related research as its primary objective [2]. At the time, few would have envisaged the contribution that a laser driven approach to ion acceleration could go on to promise, enabled by the lasers that would later be developed there.

1.1 Overview

Laser accelerated ions have been observed since the 1960's [3] from interactions at relatively low intensities of 10^{10} Wcm^{-2}, compared with those reported in this thesis, and long pulse durations of tens of nanoseconds. These lasers can create low temperature collisional plasmas, giving rise to an ion population which has few, if any of the desirable properties of the ion beams reported here.

The major breakthrough in laser technology which allowed ultrahigh intensity pulses to be produced was made in 1985, by applying a radar technology concept [4] to laser amplification. Since the adaptation of this technique of chirped pulse amplification [5], achievable focussed laser intensities have increased exponentially over the last two decades up to nearly 10^{22} Wcm^{-2} today. At these intensities, electrons are accelerated to velocities approaching the speed of light. If the laser irradiates a thin foil, the relativistic electrons can be ejected from the target, setting up large electric fields at its surfaces, in which ions can be accelerated. Due to the strength of these fields, protons can be accelerated to tens of MeV in energy in a distance of only a few microns, a feat that a conventional accelerator would require many metres to achieve. The compact nature of these plasma accelerators is one of their many attractive features, as their sizes are limited in real terms only by the laser system. Not only is the accelerator's small footprint attractive, but the proton beams are also of high quality and can be readily focussed because of their high laminarity and small source sizes. This is an important requirement for many applications.

Plans exist to improve laser technology, and the 10^{24} Wcm^{-2} intensity regime should be readily accessible before the end of the decade, with the lasers in development at the large European, Extreme Light Infrastructure [6], collaboration for example. This should make it possible to achieve higher proton energies than currently attainable, which some applications, such as hadron therapy demand. Progress in laser technology will also enable these petawatt class lasers to operate at up to ten shots per second instead of the one shot per hour, which is typical

of many modern high energy systems. This will enable greater statistics to be gathered in experiments, and will allow the capabilities of these accelerators to be demonstrated to industry, which would surely require these higher repetition rate systems.

1.2 Motivation

At some point, every physicist has been asked to justify their research, whether that be to the general public or the academic community. Fortunately, I never need to look far for inspiration as to why researching a laser driven approach to ion acceleration might be useful, and its wide range of potential applications is one of the things that attracted me to the field.

The most exciting of these applications may lie with the potential for laser driven ion beams to be applied in various ways to the world of healthcare [7, 8, 9], and the potential for them to help achieve the realisation of a clean abundant energy source, in nuclear fusion [10, 11]. A brief summary of these most exciting applications, for me, is presented over the coming pages, but other than this there is the potential for the beams to be applied to neutron production [12], as a conventional accelerator injector [13], for isochoric heating of matter [14], and in radiography [15]. An extensive discussion of the applications and required laser driven proton beam parameters can be found in the literature [13, 16].

With their unique properties, the laser driven ion beams share much in common with the early laser, which was described as a solution looking for a problem. As lasers have come to be involved in our every day lives, and are used for everything from communications to manufacturing, laser driven proton beams may too come to be widespread in many of our future technologies.

None of these problems will be directly resolved by this thesis on its own, but the major breakthroughs of *Crick and Watson*, *Einstein* or *Mendeleev* that dominate the public perception of science are few and far between. What I hope this thesis will provide, is a step in a greater journey of progression of the field.

1.2.1 Health

Perhaps one of the most exciting applications of laser driven ion beams is that they may enable hadron therapy to become more widespread than currently.

The concept of hadron therapy is one that is easily explained by figure 1.1. Ions deposit their energy in matter in a way very differently from other types of ionising radiation. As they penetrate deeper into a material, their energy loss per unit distance increases, and the bulk of an ions energy is deposited in a localised area just before it is stopped, known as a Bragg peak. Higher energy ions penetrate deeper into materials, and so if the ion energy can be controlled, the region where the maximum energy deposition occurs can be selected and targeted, with comparatively little energy being deposited in the regions surrounding the Bragg peak.

In hadron therapy, high energy ions can be used to kill localised tumours, deep seated in the body, where it would be impractical or impossible for surgery to reach. By controlling the ion energy, a lethal dose can be delivered to the tumour, whilst the surrounding tissue receives a non lethal dose. Figure 1.1 contrasts this to medical x-rays which deposit the bulk of their dose a short distance into the body, and decreases as they penetrate deeper. In order to deliver a non lethal dose to surrounding tissue, the x-rays must be delivered from different directions to minimise the exposure to healthy tissue, whilst the tumour accumulates dose. In practice this concept can also be applied to hadron therapy to further minimise the exposure of surrounding tissue.

In reality, an extended region would almost always need to be irradiated, and so instead of using one Bragg peak, several would be required, which is referred to as a spread out Bragg peak, but the same concepts apply. The exponential spectrum of the laser accelerated ions therefore may be advantageous for achieving this [17], where a conventional accelerator needs to generate the number of required Bragg peaks individually, adding a level of complexity to the task.

Hadron therapy has generally been available since the early 90's using conventional accelerators, and one of the many benefits of this is that a great deal of

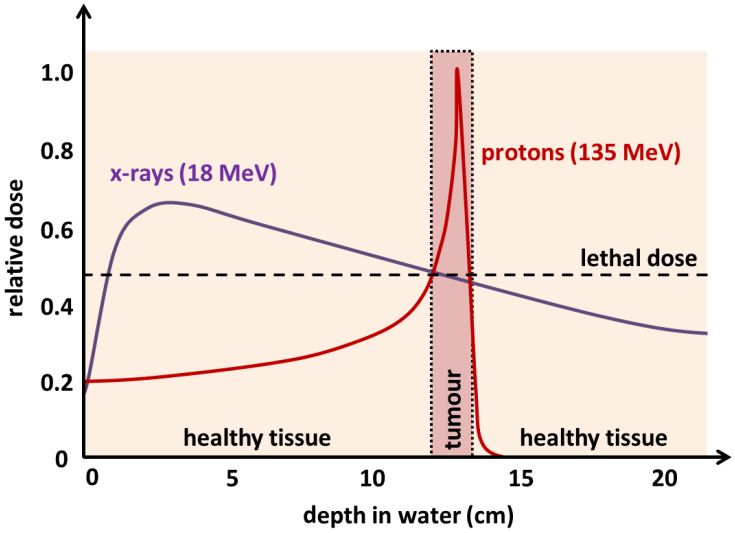

Figure 1.1: The concept of hadron therapy is illustrated by showing how a 135 MeV proton deposits energy with depth as compared to an 18 MeV x-ray. By choosing the proton energy the majority of its energy can be deposited at the site of a tumour. This is in contrast to medical x-rays which deliver the bulk of their dose to healthy tissue. Source data from *Orecchia et al.* [20].

the ion beam requirements for treatment have been identified. The laser driven ion accelerator therefore has the benefit of having target parameters to aim for. Conventionally accelerated proton beams have however been finely tuned over many years, and laser sources have some considerable ground to cover to match the beams in use today. The primary objectives for the laser driven approach are to produce a proton beam with with energy of up to 200 MeV in an efficient way to match that of conventional accelerators. The energy requirement is one aspect that may be most easily addressed by investigating the scaling as the next generation of ultrahigh powered lasers become available, but methods to increase conversion efficiency is already at the forefront of the research objectives in the field. As well as this, some of the key requirements such as focusability [18] and energy selection [19] have been demonstrated to be achievable.

The scale of the laser acceleration method offers the real intrinsic advantage over conventional accelerators. In ion beam therapy centres at the moment, large facilities are required to house the ten metre diameter synchrotrons, rising to twenty five metres for carbon beam delivery. This is a significant draw back as

it becomes increasingly difficult to incorporate the ion beam therapy centres into existing hospitals. If the therapy centres are exiled to regions far away from the hospitals, their already stretched resources must be divided.

This is not the only medical application of laser accelerated proton beams, and they have been suggested as a possible use for isotope production of fluorine, $^{18}_{9}\mathrm{F}$ [9], for positron emission tomography, and technetium, $^{99m}_{43}\mathrm{Tc}$ [21], as a radioactive tracer. To induce the necessary nuclear reactions, a threshold proton energy exists in the MeV range, which is routinely achievable using current lasers. In order to make sufficient quantities of isotope however, higher repetition rate lasers are required to deliver the necessary average beam current, and increased conversion efficiency of laser energy to protons would make the laser driven approach competitive.

1.2.2 A clean energy source

At a time when the top of most political agendas is the quest for green, carbon neutral and clean energy, an equally exciting prospect for the application of laser driven ion beams is that they may enable us to attain nuclear fusion, which is surely the ultimate energy source.

In some sense, at the nuclear level every element wants to be the element Iron. This is because the short range attractive nuclear force which holds the nucleus of the atom together can best counter the repulsive electrostatic forces between the component protons, in nuclei of this size. Figure 1.2 shows this in what is known as the binding energy per nucleon, as a function of the number of nucleons. As elements nuclei get closer to iron, a small amount of its mass is lost and converted to energy, as Einstein's famous equation, $E = mc^2$, describes. The mass loss is only very small, but because the energy density is large, a large amount of energy can be released. The energy per nuclear reaction typically releases millions of times more energy than is released by a single chemical reaction, such as the burning of coal or gas, and this is part of the reason why nuclear power is so attractive.

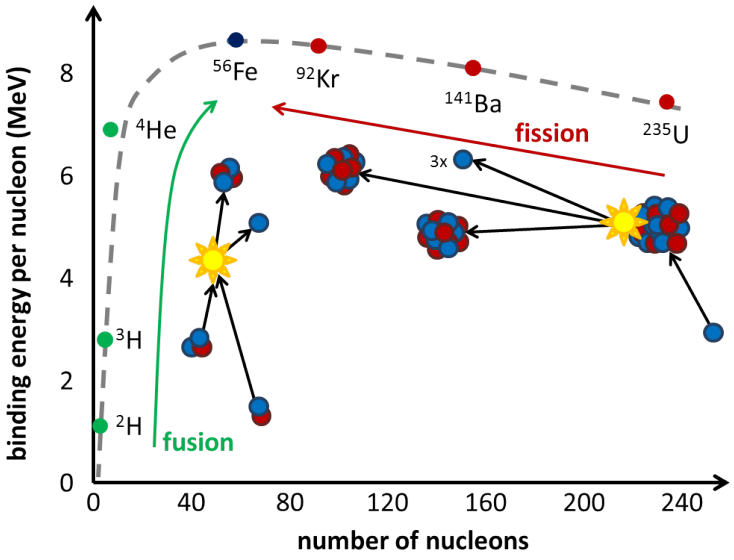

Figure 1.2: Binding energy per nucleon for the naturally occurring elements. Energy can be released by splitting large atoms into smaller ones in nuclear fission, or by merging light elements into larger ones in nuclear fusion.

There are therefore two ways that nuclei can become closer to iron and release energy. Heavy nuclei can be split into smaller ones, in a process called fission, or small nuclei can be combined into a heavier one in a process called fusion. The nuclear power plants of today work through nuclear fission to produce their energy. While this is attractive as a carbon neutral energy source, everyone is aware of the hazardous by products which can remain radioactive for many thousands of years, prompting the need to construct vast spent nuclear fuel repositories such as Onkalo in Finland [22].

The alternative is to convert lighter atoms than iron into heavier ones. This presents a new challenge as the mutual electrostatic repulsion of the light nuclei requires the particles to have temperatures of around a hundred million degrees so that they can get close enough to each other for the short range nuclear force to come into effect, creating a helium nucleus and a neutron, as in the nuclear equation 1.1. These temperatures are so vast that they only naturally occur at the centres of stars, and this highlights the challenge of the task.

$$^{2}_{1}\mathrm{H} + ^{3}_{1}\mathrm{H} \rightarrow ^{4}_{2}\mathrm{He}\ (3.5\ \mathrm{MeV}) + ^{1}_{0}\mathrm{n}\ (14.1\ \mathrm{MeV}) \tag{1.1}$$

Inertial confinement fusion is the laser driven approach to achieving nuclear fusion in the laboratory. In this scheme, lasers are used, either directly, or indirectly via the x-rays they produce, to irradiate a small deuterium tritium capsule about a millimetre in size and with a density a fraction of that of plastic. The capsule is compressed to tens of microns and with densities between ten and a hundred times that of lead. In the ideal case, the fuel will be compressed uniformly in all directions to form a small hotspot in the centre, surrounded by the denser imploding fuel shell. Initially it is only this hotspot in the centre which is heated to the temperature required to initiate fusion reactions, however, the energetic helium nucleus produced in the reaction deposits its energy in the fuel, heating it further and propagating a burn wave through the fuel.

The fact that no external forces are used to confine the fuel in this method, leads to its name; the fuel inertia, or its tendency to resist motion, alone is required to hold the fuel together while it burns. This coupled with some assumptions on the requirements of the energy gain from the fuel burn (as it is worth remembering that the final aim is to build a power plant, rather than pursuing this purely for its scientific interest), leads to the realisation of some criteria on the nature of this confinement. Most commonly this is given as the ρR condition, or the condition that the compressed fuel density multiplied by its radius must exceed 3 g cm^{-2} [23]. This ensures that a significant fraction of the fuel is burned in the short time that the reactions take place, but also places restraints on the minimal compression required to ignite the small masses necessarily burned due to the high energy density of the fuel.

At the moment, this scheme is being researched at the National Ignition Facility (NIF), in the so called indirect drive mode. *Fuel gain* has recently been demonstrated there [24], where more fusion energy has been yielded by the fuel than x-ray energy deposited in it. The authors however cite controlling the hotspot shape via more symmetrical implosion as a priority on the path toward further gain. In the past, concerns about the difficulty of achieving the necessary implosion symmetry have led some to develop alternate pathways towards fusion, such

as fast ignition [25], which relaxes some of these requirements.

In fast ignition, the compression and ignition phases are separated, potentially allowing for higher energy gain from the fuel. Here the fuel is precompressed to lower overall densities than that required in the central hotspot ignition scheme, and therefore requires lower laser energies for compression, of up to 485 kJ [26], compared to the 1.9 MJ delivered at NIF. A secondary ultrahigh intensity ignitor beam, with an energy of 100-200 kJ [10], is then used to deliver a localised dose of energetic particles to ignite the fuel and initiate a burn wave.

Some have dedicated studies to the concept of using laser driven protons for the purpose of igniting the fuel pellet [10, 11], and some of the properties of laser driven proton beams make them highly desirable for such a purpose. The protons can be focussed to generate the high energy density hot spot, and because of the Bragg peak which they deposit their energy in, they can once again be used to efficiently localise the energy deposition.

Many ion acceleration mechanisms have been reviewed for their potential applicability to the fast ignition variant of fusion by *Fernández et al.* [11], and the target normal sheath acceleration mechanism, which this thesis primarily deals with has many attractive features. The beam has a large energy spread, which at first glance may seem to mean that it would not localise any heating of the fuel pellet. However, with the most energetic protons arriving earlier in time than low energy protons, the lower energy protons encounter preheated fuel and can travel further into the target material, enabling a hot spot to be created. The temperatures and maximum proton energy required of a target normal sheath acceleration driven beam are well within the reach of current laser technology, but the most commonly cited problem is the low laser to proton energy conversion efficiency. If this can be improved, the scheme may become feasible.

Fernández et al. also consider alternative ion acceleration mechanisms to target normal sheath acceleration for fast ignition, but many of these mechanisms are in very early stages of research, with some yet to be fully experimentally realised. The estimated required laser parameters, to drive the desired proton

beams are also more stringent than that to drive a target normal sheath acceleration fast ignition beam. For these reasons, a target normal sheath accelerated proton beam may yet prove to be the best candidate for the fast ignition scheme.

1.3 Thesis outline

The remainder of this thesis is largely split into two sections. The first section, comprised of chapters 2 and 3, deals with providing the reader with details on the most relevant background on both the theoretical understanding of laser plasma interactions and on the methods used in this thesis.

Chapters 4, 5 and 6 detail the findings and interpretation of three experimental campaigns which the author made major contributions to, as detailed previously in the *Role of the Author* section.

Chapter 2

Laser plasma interaction physics relevant to ion acceleration

The acceleration of ions by ultra high intensity lasers, which this thesis is primarily concerned with, can be considered a tertiary step to two highly nonlinear preceding processes. The plasma conditions are initialised by the early time laser intensity profile, up to nanoseconds prior to the picosecond main laser pulse. The main laser pulse then generates a high energy electron population in its interaction with this plasma. It is these hot electrons which are fundamental to driving the ion acceleration, which we aim to study.

In this chapter each process, in the ion acceleration chain is introduced in a context relevant to this thesis.

2.1 Ionisation

The processes leading to plasma formation on a laser irradiated surface is highly dependent on the incident light intensity. This thesis will focus on laser intensities from $10^{12} - 10^{19}$ Wcm^{-2}, and some consideration of relevant ionisation mechanisms across this intensity range is given. This thesis is also primarily concerned with 500 fs duration, 1.054 μm wavelength interactions, which much of the discussion assumes.

A semi classical approach to the quantum mechanical ionisation processes in hydrogen preserves some level of intuition in the physical interpretation. For this, the Bohr radius, a_B, in equation 2.1 is used, which is defined as the distance from the nucleus outside which the probability of finding the valence electron falls to $1/e_N$. Other symbols have their usual meanings, as listed on pages xxi-xxiii.

$$a_B = \frac{4\pi\epsilon_0\hbar^2}{m_e e^2} \approx 52.9 \times 10^{-12} \text{ m} \tag{2.1}$$

When one laser photon does not possess enough energy to ionise the valence electron through the familiar photoelectric effect [27], the electron may be ionised by absorbing multiple photons which collectively have enough energy to overcome the ionisation potential, in a process termed multiphoton ionisation [28]. At laser intensities of 10^{10} Wcm^{-2}, approximately twelve 1.18 eV photons can irradiate the Bohr radius of the hydrogen atom, providing enough energy to overcome the 13.6 eV ionisation energy, leaving the free electron with excess kinetic energy. It is also possible that more than the requisite, n, photons are absorbed, in this case the excess, s, photons contribute to the free electron kinetic energy. This is summarised in equation 2.2.

$$K_e = (n+s)\hbar\omega_l - U_{ionis} \ni (n\hbar\omega \geq U_{ionis}) \tag{2.2}$$

In the case of single or multiphoton ionisation, the electron can be considered as being liberated from a potential well by a particle-like photon bombardment.

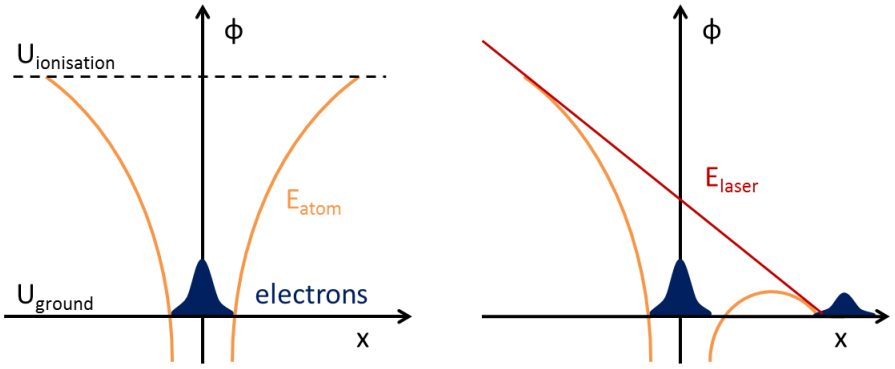

Figure 2.1: The standard picture of electrons in an atomic potential well (left). If a laser field is introduced (right), the barrier of the atomic potential well is suppressed, and electrons can tunnel out. Adapted from *Gibbon* [29].

However, by treating the coherent laser field as a wave, it can also be thought of as a retarding potential. In this case, the Bohr radius is again useful for calculating what is known as the atomic intensity, which is the field strength of laser required such that it is equal to the binding potential of the electron in the nuclear field, given by equation 2.3. When the field of the laser results in an intensity which is greater than or equal to the atomic intensity, the atom will be field ionised.

$$I_a = \frac{\epsilon_0 c}{2}\left(\frac{e}{4\pi\epsilon_0 a_B^2}\right)^2 \approx 3.51 \times 10^{16}\ \mathrm{Wcm}^{-2} \tag{2.3}$$

This is not to say that this is the limiting laser intensity for field ionisation, but only the case for which field ionisation is highly probable. In reality, the quantum mechanical nature of the electron in the potential well, lends itself to ionisation at intensities below this threshold. This is visualised in figure 2.1, when compared to the potential well. The presence of the laser field perturbs the potential, but is not sufficient to match that of the ground state of the atom. In this case, the lowering of the barrier makes it more likely that the bound electron can quantum mechanically tunnel through the barrier and become a free electron, and a threshold intensity for this to occur using a semi classical approach can be shown to be 1.4×10^{14} Wcm^{-2} for hydrogen [29]. This form of tunnelling ionisation is also referred to as barrier suppression ionisation.

A convenient way to determine whether the multiphoton or field ionisation is

the dominant mechanism can be made by considering whether the electric field of the laser is significantly distorting the Coulomb potential. This is often described by the Keldysh parameter [30], in equation 2.4.

$$\gamma_K = \omega_l \sqrt{\frac{2U_{ionis}}{I_l}} \tag{2.4}$$

Typically, the bulk plasma electrons will gain energies in the tens to hundreds of eV range. Provided that the free electron kinetic energy is at least equal to that of the ionisation energy of a bound electron, the bound electron can be ionised by the transfer of this energy via a collision. The characteristic time between electron collisions, τ_{coll} can be estimated from equation 2.5 from *Robinson* [31]. The Coulomb logarithm, $\ln \Lambda$, gives an estimate of the average interaction distance in the plasma.

$$\tau_{coll} \approx 2.4 \times 10^{-9} \left(\frac{T_e}{\mathrm{eV}}\right)^{3/2} \left(\frac{n_e}{10^{20}\ \mathrm{m}^{-3}}\right)^{-1} \frac{1}{Z \ln \Lambda} \tag{2.5}$$

This simple estimate of the electron collision time picks out many of the key relationships in collisional ionisation. This correctly predicts that collisions are more frequent and hence more important for lower temperature and higher density plasmas. Physically, this is due to higher energy electrons having a lower cross section for interaction, which is reproduced in this simple model by higher energy electrons spending less time in the Coulomb field. Additionally, a first order estimate of the collision time in the plasma can be obtained to decide if the plasma is collisional or collisionless on the timescales of interest.

This electron collisional ionisation is not limited to the time of the laser irradiating the plasma, and provided the electrons initially have enough energy, they may liberate electrons which go on to cause more ionisation, in a process termed avalanche ionisation.

2.2 Plasma

The problem in defining any state of matter is a difficult one as it will inevitably share some common properties with other states of matter at some scale. Some of the general features of the plasma state are described here, however, these properties should not be considered as being exclusive to plasmas, but rather as a set of properties which a plasma possesses.

At the microscopic level, a plasma is composed of free charged particles instead of the electrically neutral atoms which make up the more familiar states of matter, as such, plasmas have some different properties. The coming chapter discusses in some more detail some of the consequences of this, such as the effect that it has on electromagnetic wave propagation, and how the energy from the electromagnetic wave can be coupled into the plasma.

Plasma can also exhibit collective behaviour, in that one charged particle can influence many other nearby charged particles simultaneously, which is in contrast with the more familiar states of matter which have their behaviour dominated by binary collisions between the constituent particles. A useful quantity to find if this criteria is satisfied is the Debye length, λ_D, which is the characteristic scale length over which the potential due to a test charge is attenuated by a factor of $1/e_N$. This is expressed in equation 2.6.

$$\phi(x) = \phi_0 \exp\left(-x\sqrt{\frac{n_e e^2}{\epsilon_0 k_B T_e}}\right) = \phi_0 \exp\left(-\frac{x}{\lambda_D}\right) \tag{2.6}$$

The Debye shielding length therefore dictates that the potential due to a test charge in the plasma is exponentially attenuated as opposed to the inverse square decay of its field in free space, and effectively imposes a characteristic distance over which the quasineutrality condition can be breached. For the plasma condition to be satisfied, the average number of particles in the sphere of radius λ_D, known as the plasma parameter, must be greater than unity.

2.2.1 Electromagnetic wave propagation in plasma

The nature of an electromagnetic wave propagating in plasma can be derived from first principles using Maxwell's equations. The strong fields of a laser interact with both the electrons and the ions of the plasma, however, owing to their much larger mass, the ion motion is typically negligible compared to that of the electrons. For this reason, it is convenient to consider plasma electrons to be in motion, with the far less mobile ions forming a stationary background. The electric field of the laser can therefore be thought to displace electrons from the ions, and as a consequence large electrostatic restoring forces are set up due to the charge separation, as in equation 2.7.

$$\mathbf{F}_e = -e\mathbf{E} = m\frac{d^2\mathbf{x}}{dt^2} \tag{2.7}$$

The result is that contrary to the case for vacuum, the oscillating electrons have a non zero current density in the Ampère-Maxwell law, which results in an additional term to the familiar vacuum wave equation, shown in equation 2.8.

$$\nabla^2\mathbf{E} = \frac{1}{c^2}\frac{\partial^2\mathbf{E}}{\partial t^2} + \mu_0\frac{\partial\mathbf{j}}{\partial t} \tag{2.8}$$

Taking account of this current density, the dispersion relation for the wave propagating in plasma is shown to be equation 2.9.

$$\begin{aligned} c^2k^2 &= \omega^2 - \frac{n_e e^2}{\epsilon_0 m_e} \\ c^2k^2 &= \omega^2 - {\omega_{pe}}^2 \end{aligned} \tag{2.9}$$

Compared to the vacuum case, the additional term in the dispersion relation is the electron plasma frequency. At first glance, equation 2.9 indicates that as ω_l tends towards ω_{pe} the wave vector tends to zero, and therefore light can propagate in a plasma only when its angular frequency is greater than that of the plasma frequency $\omega > \omega_{pe}$. For this reason, this frequency is sometimes referred to as the cut off frequency, as light below this limit is cut off from propagating

in the plasma, which is said to be overdense. Plasma electron densities below this density are said to be underdense, and the critical density in equation 2.10, separates these two regimes.

$$n_{crit} = \frac{\epsilon_0 \gamma m_e \omega_l^2}{e^2} \tag{2.10}$$

On closer examination, by considering the spatial part of the wave beyond the critical surface, an evanescent wave can be shown to exist, which exponentially decays as it tunnels beyond the critical surface. The characteristic depth that the light can reach is described by the skin depth, δ_s, which is when the electric field reaches $1/e_N$ of its magnitude at the critical surface.

$$E(z) = \exp(ikz) = \exp\left(i\sqrt{\frac{\omega_l^2 - \omega_{pe}^2}{c^2}}z\right) = \exp(-z/\delta_s) \tag{2.11}$$

As the critical density is dependant on the Lorentz factor, this means that in practice it can be difficult to precisely define the critical density for a linearly polarised wave as we will see over the coming chapter.

2.2.2 Electron interactions with electromagnetic waves

2.2.2.1 Infinite plane waves

Considering the motion of a free electron is informative for describing the behaviour of electrons in the field of an ultra intense laser. The motion of charged particles in the presence of electric and magnetic fields is described by the Lorentz force in equation 2.12.

$$\frac{d\mathbf{p}}{dt} = q\left(\mathbf{E} + \mathbf{v} \times \mathbf{B}\right) \tag{2.12}$$

In the classical case, with the magnitude of the electric field being a factor of c larger than the magnetic field, the motion of the oscillating electron can be obtained by neglecting the $\mathbf{v} \times \mathbf{B}$ term. The quiver velocity, v_{osc} of the electron

oscillating in an electric field of amplitude E_0, is obtained in equation 2.13.

$$v_{osc} = \frac{e}{m_e \omega_l} E_0 \sin \omega_l t = a_0 c \sin \omega_l t \tag{2.13}$$

Here, the normalised vector potential, a_0, has been introduced, which is the ratio of the quiver velocity to the speed of light, and is a useful parameter for identifying the transition into the relativistic regime. Relativistic interactions are usually defined as those where $a_0 > 1$. Equation 2.14 expresses this in more useful units, which define the relativistic regime to be for laser irradiances upward of 1.37×10^{18} Wcm$^{-2}\mu$m^2.

$$a_0 \equiv \frac{eE_0}{m_e \omega_l c} \cong 0.85 \left(\frac{I\lambda^2}{1.37{\times}10^{18} \text{ Wcm}^{-2}\mu\text{m}^2} \right)^{\frac{1}{2}} \tag{2.14}$$

When the quiver velocities in the laser electric field are relativistic, the $\mathbf{v} \times \mathbf{B}$ term of the Lorentz force can no longer be ignored, and this term can be calculated by inserting the quiver velocity in equation 2.13 into the Lorentz equation 2.12. Because the electron oscillations are orthogonal to the magnetic field of the laser, this gives rise to a force in the direction of the laser, and accelerates electrons to the velocity given in equation 2.15.

$$v_z = \frac{e^2}{4 m_e^2 \omega_l^2 c} E_0^2 \cos(2\omega_l t) = \frac{a_0^2}{4} c \cos 2\omega_l t \tag{2.15}$$

This simple analysis shows that for relativistic electron velocities the magnetic field of the laser gives rise to a force accelerating electrons to the characteristic velocity v_z. This occurs at twice the laser period and always points in the direction of the laser, because of the cross product of the current density and the magnetic field always being in the same direction.

2.2.2.2 Inhomogeneous fields

In addition to the infinite plane wave assumed so far, in practice, a focussed laser pulse has significant electric field gradients. These gradients arise from the fast component of the electric field oscillating at ω_l, travelling inside a Gaussian like carrier wave that arises from the laser being focussed in space and pulsed in time.

The result is that an electron oscillating in the laser electric field can experience a strong push over the first half cycle of the laser period, to a region with a lower field strength. This lower field provides a restoring force which is inadequate to return the electron to its original position. Therefore, over a single laser cycle in an inhomogeneous field, an electron will be pushed from a region of high field strength to low field strength, providing a net force in a direction away from the high intensity regions. This is called the ponderomotive force, and the process repeats for each laser cycle within which the electron is influenced by the laser field. In the classical case, considering only the electric field, the force can be shown to be represented as in equation 2.16 which is the negative average gradient of the classical ponderomotive potential [29].

$$\mathbf{F}_{pond} = -\nabla\phi_{pond} = -\frac{e^2}{4m_e\omega_l^2}\nabla\mathbf{E}^2 \tag{2.16}$$

Under a relativistic treatment of the ponderomotive force this becomes equation 2.17. The ponderomotive potential energy in equation 2.18 gives an estimate of the energy transferred by the laser to the electron per laser cycle [32].

$$\mathbf{F}_{pond} = -m_e c^2 \nabla\gamma \tag{2.17}$$

$$U_{pond} = (\gamma - 1)\, m_e c^2 \approx 511 \text{ keV} \left(\sqrt{1 + \left(\frac{I_l \lambda^2}{1.37 \times 10^{18} \text{ Wcm}^{-2}\mu\text{m}^2} \right)} - 1 \right) \tag{2.18}$$

2.3 Coupling of laser energy into plasma electrons

The coupling of laser energy into plasma electrons is often described in terms of different absorption mechanisms, with each mechanism a simplified case, where imposed assumptions restrict the discussion to a particular aspect of the interaction. In general, the laser energy absorption by plasma electrons is understood by considering the relative efficacy of the mechanisms for the plasma conditions under consideration.

2.3.1 Collisional absorption

Collisional absorption, commonly referred to as inverse bremsstrahlung, occurs when free electrons oscillate in a relatively weak, laser electric field, with the field irradiance commonly quoted as being lower than 10^{15} $\mathrm{Wcm^{-2}}\mu\mathrm{m}^2$, in the presence of an ion distribution.

At this irradiance, electrons would quiver in the field of the laser, resulting in no damping of the electromagnetic wave as it passes. However, the presence of ions in the plasma means that as the electron quivers with some energy borrowed from the half cycle of the light wave, there is a probability that the electron will collide with a more massive plasma ion, scattering the quivering electrons. The result of this is that some energy of the oscillating electrons is converted into a thermal distribution, and hence lost by the laser. This happens on average, at the electron ion collision frequency, given in equation 2.19. The fraction of energy absorbed by a plasma due to a field propagating over a density gradient, l_{ss}, is given in equation 2.20 [33], where l_{ss} satisfies $n_e(x) = n_{e0}\exp\left(-l_{ss}/x\right)$.

$$\nu_{ei}(n_{crit}) \propto \frac{n_{crit}Z^*}{T_e^{3/2}} \tag{2.19}$$

$$f_{abs} = 1 - \exp\left(\frac{32}{15}\frac{\nu_{ei}(n_{crit})}{c}l_{ss}\right) \tag{2.20}$$

Collisional absorption is maximised near the critical surface of low temperature, long scale length, high Z^* plasmas. The temperature dependence in equation 2.19 is a consequence of higher energy electrons having a smaller collision cross section, and so the mechanism is dominant for lower intensity beams.

2.3.2 Collisionless absorption

There are many different paths through which collisionless coupling of laser energy into electrons can be achieved, but the common mechanism they possess as summarised by *Davies* [34], is that they result from driving electron oscillations across a density gradient. A p-polarised laser is assumed in the discussion that follows, but some consideration of polarisation dependence is given in section 2.3.3.

2.3.2.1 Resonance absorption

The presence of a nonuniform preplasma can significantly effect the propagation of a laser within it, and for all but an oblique angle of incidence the laser cannot freely propagate to the point of the critical density. It is simple to show that for a plasma which has a density scale length $\nabla n_e = \nabla(0, n_{ey}, 0)$ and a wave vector $\mathbf{k} = (k_x, \frac{\omega_l}{c}\sin\theta_i, 0)$, as in figure 2.2, the dispersion relation in equation 2.9, becomes that in equation 2.21.

$$\omega_l^2(1 - \sin^2\theta_i) = \omega_p^2 + c^2k_x^2 \tag{2.21}$$

This shows that the wave vector continuously changes in the density gradient, and that reflection, $k_x = 0$, takes place at $n_e = n_{crit}\cos^2\theta_i$. Here, a polarised electric field, can be transverse or parallel to the density gradient. In the p-polarised case, the field tunnels to the critical density where it can resonantly excite a plasma wave. As the electric field is exponentially attenuated beyond this point, the restoring field is weak, resulting in the plasma wave breaking, allowing electrons to gain energy as they are accelerated across the density gradient.

The angle of incidence relationship is described by the Denisov function, ξ [35], in equation 2.22, which also describes the fraction of energy absorbed by the mechanism, f_{abs}.

$$\begin{aligned} \xi &= (kl_{ss})^{1/3} \sin\theta_i \\ f_{abs} &\propto \xi \exp\left(-\frac{2}{3}\xi^3\right) \end{aligned} \tag{2.22}$$

The absorption mechanism peaks at some intermediate angle of incidence between oblique and glancing incidence. This is because a scale length must exist for the mechanism to take place, while the fraction of the field that tunnels to the critical density position is reduced with increasing angle of incidence.

Good agreement exists with this model and the experimental results up to irradiances of around 10^{17} Wcm$^{-2}\mu$m^2. However above these intensities relativistic effects become more important.

2.3.2.2 Vacuum heating

In the case where the electron oscillation amplitude is greater than the plasma density scale length, *Brunel* [36] proposed that electrons could be pulled by the laser field into the vacuum in one half cycle of the laser period and then accelerated back in the second half cycle. In this way, when the electric field of the laser interacts with a steep density gradient of overdense plasma, the electron does not encounter an equal restoring force as it crosses the critical surface, resulting in a net acceleration of the electron. It was observed in PIC codes by *Gibbon and Bell* [37], that electrons can in fact make multiple oscillations in the vacuum before being accelerated over the density gradient, which the authors described as vacuum heating.

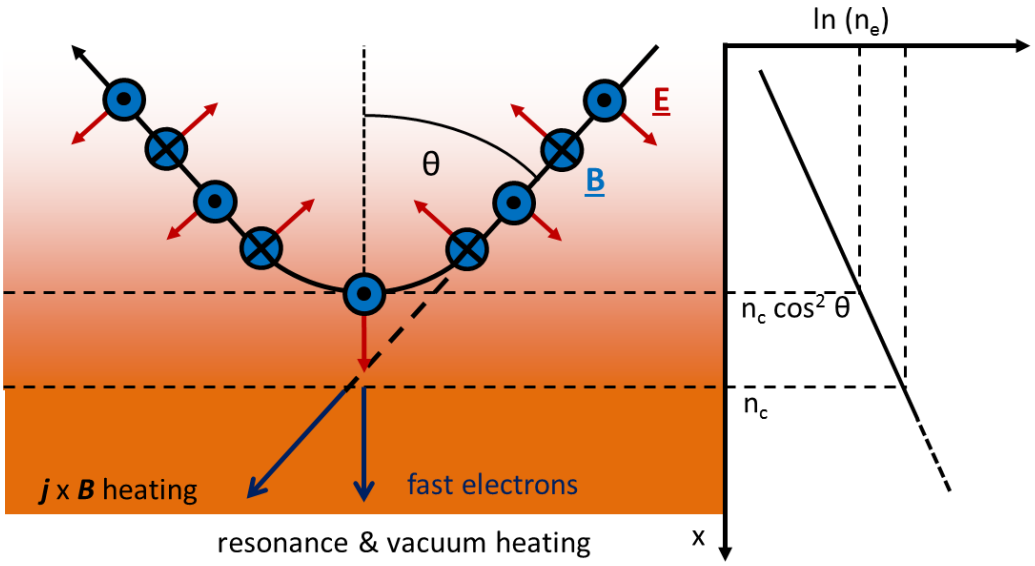

Figure 2.2: A summary of the collisionless heating mechanisms, as defined in the text, and their relation to the laser incidence angle.

2.3.2.3 Relativistic j x B heating

It has been shown that as the laser irradiance approaches 10^{18} $\mathrm{Wcm^{-2}}\mu\mathrm{m}^2$, electrons acquire relativistic quiver velocities in the electric field, resulting in a non negligible magnetic field contribution to the Lorentz force. As the slowly varying electric field envelope also acts upon the electrons, through the ponderomotive force, this allowed *Kruer and Estabrook* [38] to obtain the total force to be that in equation 2.23

$$\mathbf{F} = -\frac{m}{4}\nabla v_{osc}^2 \left(1 - \cos 2\omega_l t\right) \tag{2.23}$$

This net force is the result of both the electrons being pushed via the ponderomotive force and accelerated at twice the laser frequency by the fast $\mathbf{v} \times \mathbf{B}$ component, with a period of twice that of the laser and in the laser direction. As there is no condition on the direction of the electron oscillations relative to any plasma density gradient, this mechanism can result in the electron being accelerated across the density gradient by either an s-polarised or p-polarised laser pulse. The mechanism is found to be optimised at high electron densities, and so

is most efficient for oblique incidence.

The $\mathbf{j}\times\mathbf{B}$ mechanism, arising from the magnetic field component of the laser is therefore distinct from the collisionless heating mechanisms of resonance absorption or vacuum heating, which are due to only the electric field of the laser. As electrons are accelerated in different directions by the different components, the mechanisms can be identified experimentally by this. Additionally, where the resonance absorption or vacuum heating accelerate electrons at the laser frequency, the $\mathbf{j}\times\mathbf{B}$ mechanism accelerates electrons at twice this frequency.

2.3.3 Polarisation considerations

In the theoretical cases discussed, some clear polarisation dependencies emerge from some of the absorption mechanisms, particularly in resonant absorption and vacuum heating, which require an electric field component pointing into some region of the target, which is termed p-polarisation. However, the results of this thesis have been obtained exclusively from interactions in which the laser pulse is s-polarised relative to the target, and so some comments are made on the *de facto* polarisation dependence of laser absorption by hot electrons.

It may be surprising at first that in practice, the laser polarisation direction makes little difference to the TNSA ion acceleration process from relativistic interactions, which this thesis is primarily concerned with. *Ping et al.* [39] first showed that the laser energy absorption fraction at irradiances above 10^{17} $\mathrm{Wcm^{-2}}\mu\mathrm{m}^2$, quickly rises from being a few percent to around 30 % at 3×10^{18} $\mathrm{Wcm^{-2}}\mu\mathrm{m}^2$; an absorption fraction which almost matches that of p-polarised light at the same irradiance.

Further than this, *Gray et al.* [40] measured the escaping electron distribution of s-polarised interactions at the PHELIX laser, from which all of the data presented in this thesis was obtained. These measurements show that the escaping electrons on the target rear side are predominantly emitted along the incident laser axis for 3×10^{19} $\mathrm{Wcm^{-2}}$ $\mu\mathrm{m}^2$ interactions, and retains a strong component along the laser axis for lower irradiances of 5×10^{18} $\mathrm{Wcm^{-2}}\mu\mathrm{m}^2$, with an

additional component in the target normal direction.

Additionally, *Gray et al.* directly measured the maximum proton energy from the interactions in both polarisations, and found this to be independent of the laser polarisation for laser incident angles between 10° to 80°.

These experimental results indicate that as the electric field of the laser becomes adequate to accelerate the electrons to relativistic energies, the relativistic $\mathbf{j} \times \mathbf{B}$ heating begins to dominate the laser energy absorption. As well as this, the fact that the electron movement is not limited to only the laser direction, but occurs in all directions due to the ponderomotive force, is likely to further complicate the simple representations of absorption presented so far. With electrons acquiring momentum in many different directions in a relativistic interaction, mechanisms that would otherwise be inaccessible for a given polarisation can therefore become possible, and it is easy to see why no single mechanism can be used to describe the laser energy absorption as a whole.

The shape of the critical surface is also a factor which can affect the absorption of the laser. On the scale of the laser spot size, this shape is determined by the incident laser radiation pressure balancing the thermal pressure of the plasma electrons, which leads to a curved critical surface due to the laser transverse intensity profile. However, sub spot size structure is commonly observed in simulations, in the form of critical surface rippling for example. Each of these processes changes the effective angle of incidence at each point on the critical surface, and can lead to enhanced absorption of the laser pulse.

Laser absorption into hot electrons is therefore a more complex process, than can be described by any individual mechanism and is highly dependent on the initial conditions of the target preplasma. However, it can be concluded from closer examination and experimental results, that in the relativistic regime, a considerable fraction of laser energy absorption into hot electrons, to drive ion acceleration is possible regardless of the polarisation of the laser.

2.3.4 Focussing effects of preplasma

From the plasma dispersion relation in equation 2.9, the refractive index, η, of the plasma can be shown to be that in equation 2.24

$$\eta = \sqrt{1 - \left(\frac{\omega_p}{\gamma\omega_l}\right)^2} = \sqrt{1 - \frac{n_e}{\gamma n_{crit}}} \tag{2.24}$$

The refractive index is therefore proportional to only the local electron density, and as expected, the refractive index only has real solutions in underdense plasma. However, as the real laser has a strong transverse intensity profile in space, plasma created by the laser pulse might also have a strong transverse electron density profile, as the ionisation has already been shown to be dependent on the laser intensity.

As the deflection of the beam is greater from regions of higher refractive index, an electron density peaked on axis due to intensity dependent ionisation, results in defocussing of the laser by the plasma. As the total deflection depends on the path length of the laser in the plasma, this is more important for lasers propagating through long scale length plasma at ionising intensities.

When relativistic effects become important, the Lorentz factor in equation 2.24 also becomes important. The electrons oscillating in the centre of the beam have a larger Lorentz factor than those at the edge. The end result of this, is that the refractive index profile due to relativistic effects is peaked on axis, which results in a focussing of the laser beam, in contrast to the ionisation induced defocussing, where the refractive index is minimal at the centre. The beam spreading can then be cancelled by self focussing, if the laser has the critical power in equation 2.25, as given by *Barnes, Kurki-Suonio and Tajima* [41].

$$P_{crit} \cong 17.5 \left(\frac{\omega_l}{\omega_{pe}}\right)^2 \text{GW} \tag{2.25}$$

Why the self focussing depends on the power of the beam can be understood as this. The refractive index differences across the beam profile are induced by the beam intensity, and cause the on axis beam to travel more slowly than the edge of the beam. This induces a phase difference over the beam profile, and it is the path difference of these two regions of the beam that determine the focussing angle of the beam. The focussing is dependent on both the intensity and the profile of the beam, and therefore a dependent on the power for focussing exists.

So far, a uniform and fully ionised plasma has been assumed. However, the ponderomotive force also expels electrons from the high intensity regions of the laser. A depleted electron density in the central region acts to complement the induced relativistic electron density profile from the laser profile, and this can lead to an enhanced self focussing compared with the laser profile alone.

2.4 Laser driven ion acceleration

Until laser technology delivers intensities in the region of 10^{24} $\mathrm{Wcm^{-2}}\mu\mathrm{m}^2$, ions cannot be directly accelerated by laser fields to relativistic energies in the same way as has been described for electrons. However, high energy ion acceleration using lasers is possible, and laser driven protons with weakly relativistic energies of 120 MeV, have been observed [42], and MeV proton acceleration is routine.

The specific nature of the laser driven ion acceleration mechanism depends primarily on the areal density of the target and the laser intensity that irradiates it. The most relevant ion acceleration mechanism for the experiments in this thesis is the target normal sheath acceleration mechanism [43, 44], which dominates the majority of moderately relativistic intensity interactions when micron thick foils are irradiated with micron wavelength lasers. The proceeding sections discuss the target normal sheath acceleration mechanism in more detail. For completeness a brief discussion of some other laser driven ion acceleration mechanisms are introduced later.

2.4.1 Target normal sheath acceleration

On the target front surface, it has been shown that the laser can accelerate electrons to relativistic energies, typically in the MeV range. These electrons are capable of travelling through micron width foils relatively unperturbed, owing to their small cross sections for collisional and radiative stopping. On reaching the target rear, the most energetic of these electrons can escape the target, setting up large electric fields due to the charge separation, which reach 10^{12} Vm^{-1}. At this point, the electric field strength is sufficiently large that electrons with energies in the MeV range and which are still being generated by the laser source, do not have the required escape velocity of the field, over the few micron Debye length surrounding the target. The result of this is that the electrons being displaced by the heavier bulk target oscillate from one side of the target to the other, maintaining charge separation fields, in a process termed refluxing. Importantly, as the electrons are constantly being generated over the laser pulse duration, and with the target transit time of the electrons being on the order of femtoseconds for a micron thick target, this field remains quasistatic in nature, and does not fluctuate significantly due to the electron oscillations.

On the non irradiated, target rear, where there is initially no plasma, the electric fields are sufficiently large that barrier suppression ionisation processes ionise the surface [45]. Unless steps have been taken to treat the target surface, regardless of the target material, the surface is usually composed of a contaminant layer of hydrocarbons and water adsorbed from the atmosphere.

The newly created ions on the target rear surface feel an average field due to the displacement of these many electrons and are accelerated in the direction of the field, being normal to the target plane, hence the term target normal sheath acceleration (TNSA). High charge to mass ratio ions are preferentially accelerated in the strong fields, as they stream from the target surface, and experimentally these are found to dominate. Accelerating these ions in the TVm^{-1} fields over the few micron Debye lengths results in the ions acquiring MeV energies.

A simple consideration of the evolution of the sheath field in one dimension can

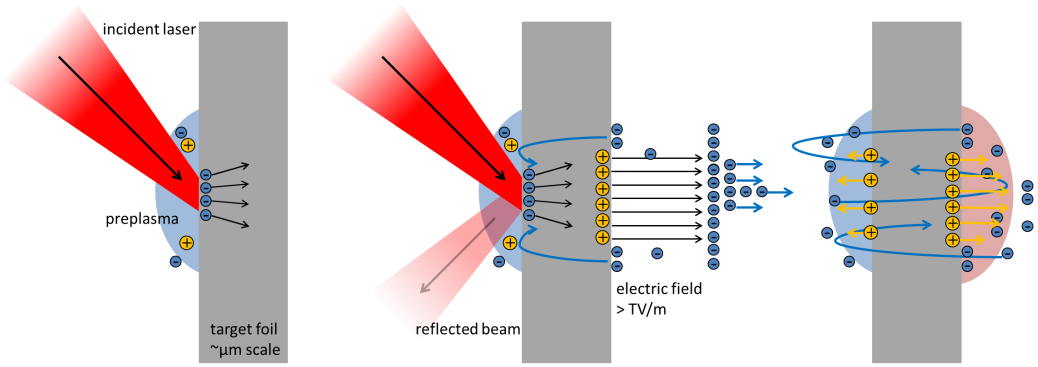

Figure 2.3: A schematic of the target normal sheath acceleration mechanism

be used to extract some of the expected scaling of the mechanism. For simplicity an ion slab with an initial step density gradient, with density n_{i0}, on one side and zero on the other, and an electron density governed by a Boltzmann distribution as in equation 2.26 is assumed. The integration of Poisson's equation gives the form of the electric field on the target rear, as equation 2.27, given by *Roth and Schollmeier* [31].

$$n_e = n_{e0} \exp\left(\frac{e\phi}{k_B T_h}\right) \tag{2.26}$$

$$E(z) = \frac{2k_B T_h}{e} \frac{1}{z + \sqrt{2}\lambda_D} \tag{2.27}$$

This shows that the maximum field, is proportional to the hot electron temperature, which is itself a product of the laser intensity on the target front surface, recalling equation 2.18, for instance which shows the ponderomotive scaling of the hot electron temperature. Assuming that the ion energy will be proportional to the potential generated by the hot electrons, it is reasonable to assume that the ion energy scales with $(I\lambda^2)^{1/2}$. A scaling of this order is indeed obtained experimentally, and so from simple considerations of the electrostatics of the plasma, some dynamics can be predicted using plasma expansion models.

2.4.2 Plasma expansion models

2.4.2.1 Self similar expansion

A simple plasma expansion into vacuum, which has been predictive of low intensity long pulse interactions, is based on a fluid model of collisionless cold ions driven by an isothermal hot electron population. When the ions are assumed to be fixed in space with the electrons forming clouds around the ions, the electric field can be found by considering the force balance due to the electron pressure as in equation 2.28, given by *Gibbon* [29].

$$\begin{aligned} n_e e E &= -\frac{\partial P_e}{\partial x} \\ E &= -\frac{k_B T_e}{e}\frac{1}{n}\frac{\partial n}{\partial x} \equiv -\frac{k_B T_e}{e l_{ss}} \end{aligned} \tag{2.28}$$

This naturally introduces the concept of the plasma scale length, l_{ss} which is the characteristic length over which the plasma density falls to $1/e_N$ of its original value.

If the ions in this field are assumed to obey the continuity equations of mass and momentum, and with the stated condition of quasineutrality, the electron driven expansion can be shown to obey the self similar solutions in equation 2.29.

$$\begin{aligned} v_i(z,t) &= c_s + \frac{z}{t} \\ n_e(z,t) = Z n_i(z,t) &= n_{e0} \exp\left(-\frac{z}{c_s t} - 1\right) \end{aligned} \tag{2.29}$$

2.4.2.2 Plasma expansion by sheath fields

The self similar expansion has been successful in predicting low temperature and high density plasma expansion, but it also has some intrinsic issues. One limitation is that the self similar solution does not limit the ion velocity, this is easily checked by equation 2.29, which says that as the z becomes infinite, so does the ion velocity. Clearly this is incorrect. As well as this, the model assumes an

ion density distribution that goes to infinity, and so the plasma expansion cannot even in principle be extended to the case of the step like density profile which is assumed in TNSA.

A more subtle issue as observed by *Mora* [46], is that the self similar plasma expansion is only meaningful as long as the Debye length does not exceed the density scale length, which is inevitably violated at some point. This leads to an enhancement of the local electrostatic field and to hence to the ion velocity of the expansion.

In order to extend this model to reflect a more meaningful plasma expansion into vacuum, *Mora* [46] suggested this could be limited by the physical reality that at time zero, the position of the ion front is well defined. This leads to there being a well defined ion front position at all times, from which a useful maximum ion velocity can be found at each time.

Following on from the general assumption of the electron distribution and the electric field found in equation 2.27, a Lagrangian code was developed to solve the problem numerically from the fluid continuity equations 2.30 and the Poisson equation describing the potential, to find the temporal scaling of the maximum proton energy. This is in terms of the factor, $\tau_M = \omega_{pi} t/\sqrt{2e_N}$.

$$\frac{\partial n_i}{\partial t} + \frac{\partial}{\partial x}\left(n_i \mathbf{v}_i\right) = 0 \qquad \frac{\partial v_i}{\partial t} + \mathbf{v}_i \frac{\partial \mathbf{v}_i}{\partial x} = -\frac{e}{m_i}\frac{\partial \phi}{\partial x} \tag{2.30}$$

$$K_{max} = 2k_B T_e \ln^2\left(\tau_M + \sqrt{1+\tau_M^2}\right) \tag{2.31}$$

The *Mora* model is again driven by an isothermal plasma expansion, and as with all isothermal models, the proton energy will tend to become infinite over time. The difference is that a maximum proton energy at each time is assumed, providing a useful starting position. An isothermal expansion may be valid to some extent for times similar to the laser duration, as in this case the laser is a constant supply of hot electrons at a given time. Many authors have applied the empirical scaling that $1.3\tau_l$ is a good estimate of the acceleration time for this

model. By extending the work further, *Mora* was able to show that a finite ion energy is achieved in an adiabatic description of the plasma expansion model [47].

In experimental scaling work, this model has been employed successfully by *Fuchs et al.* [48], who demonstrated that up to intensities of 6×10^{19} Wcm^{-2}, the model predicts accurate ion energies when assuming the ponderomotive potential to be accelerating the electrons.

2.4.2.3 Effect of rear target density scale length on ion acceleration

Grismayer and Mora [49] took the work of *Mora* further to consider the effect of an initial ion density gradient on the plasma expansion model, with specific interest in the maximum ion energies that could be achieved under these conditions. The ion density is assumed to take a form which reflects an expansion initiated by a previous low temperature electron population, which is likely to be the most practical choice for many situations. The plasma expansion is then considered by introducing an electron population in Boltzmann equilibrium as before.

From the ion acceleration perspective, the combined electron and ion distributions cause two distinct field zones to emerge. A quasineutral zone, closer to the bulk target, where the ion and electron populations are about equal in number density, and a negative zone far from the bulk target, where the electron density exceeds the ion density. The accelerating electric field is therefore a product of these two contributions, and the potential can be found by solving Poisson's equation.

The case of an infinitely steep ion density gradient results in a maximum accelerating field which occurs at the vacuum interface. However, when the ion density scale length is around five times the Debye length, the maximum field no longer arises from the sheath fields, but from the quasi neutral region of the density profile, with the field decaying further away from the bulk target. The maximum electric field then becomes that given by the self similar solution in equation 2.28, extended over the quasineutral region of space, resulting in a

plateaux in the electric field over a spatial region.

In an isothermal model, the electric field plateaux is constant in time, resulting in ions from deeper within the plasma gaining more energy than the ions in front of them, leading to a wave breaking. The effect of the wave breaking is a peak in the ion density profile, and hence a peak in the electric field toward the ion front. Additionally, because of the constant value of the electric field of the plateaux, the electric field exceeds that for the step density case. From the point after wave breaking, the ion velocity from acceleration in this field tends toward the same temporal evolution as observed for the step profile case. With an isothermal expansion however, the maximum ion energies become independent of the initial scale length for long time.

The adiabatic case of this expansion was also explored, and whilst the same general principles apply to the ion acceleration mechanism, the finite energy content of the fields and the electrons limit the energy gain by the ions. This enables the model to make predictions of the maximum final energy of the ions, and the model was found to be in good agreement with experimental data for plasma scale lengths of up to 20 μm and incident laser intensities of 10^{19} Wcm^{-2} [50].

2.4.2.4 Multi pulse sheath acceleration

Until recently, the conversion efficiency of laser energy to forward direction MeV protons has been limited to a few percent in the TNSA acceleration mechanism. Many ideas have been explored to enhance this fraction, by the use of microstructured targets [51], which can be used to increase the absorbed energy fraction, or by reduced mass [52] and reduced thickness targets [53] which more efficiently couple the accelerated electrons energy to ions.

Multiple laser pulses have also been used to enhance the conversion efficiency into ions whilst increasing their maximum energy, first experimentally realised through using a low intensity nanosecond pulse to set up the preplasma conditions that a relativistic pulse goes on to interact with [54, 55].

The concept of using collinear relativistic pulses for ion acceleration was then

introduced *Robinson, Neely, McKenna and Evans* [56] proposed that a double pulse could be used to modify the TNSA mechanism into a new Multi Pulse Sheath Acceleration Mechanism (MPSA). Numerical modelling suggested that the light ion front plays an important role in the mechanism, where low energy spectral peaks with enhanced conversion efficiency compared to TNSA in the MeV region were predicted.

In MPSA a lower intensity relativistic pulse initiates the ion acceleration as in TNSA, where the higher charge to mass protons surge ahead of the higher charge to mass ions. Some time later, the hot electrons generated by a more intense second pulse are injected into the moderately expanded rear surface. An increase in the local electron temperature causes an enhanced electrostatic field to be generated at the position of the light ion front, where there is a build up of electrostatic charge. This enhanced electrostatic field once again accelerates some of the initially lower energy protons to higher energies than when the pulse is absent, and therefore an enhanced number of protons across the spectrum are generated. When these protons with enhanced energy catch lower energy protons ahead of them, a wave breaking occurs, causing a second enhanced field area from which spectral peaks are generated. The simulations were conducted using 1D PIC and a 1D Vlasov code, with both broadly looking at the same setup of two 40-100 fs pulses delayed by 100-150 fs, predicted similar spectral features.

This inspired experimental investigation of the mechanism by *Markey et al.* [57], who found that for 700 fs duration pulses, separated by 1.5 ps, the laser to proton energy conversion efficiency could be enhanced by a factor of 3.3 compared to a single pulse interaction alone. However, the predicted spectral peaks were not observed on either the radiochromic film or Thomson parabola ion spectrometers in the experiment.

In the modelling by *Markey et al.*, for longer pulses of 300 fs in duration, closer to that for which experimental data has been obtained, a longer time delay between the prepulse and main pulse may allow more sufficient plasma expansion than in the case by *Robinson et al.*, where 100 fs delays between the two pulses

were investigated. In the modelling, *Markey et al.* reports that the absorption of the main pulse is enhanced, compared to the single pulse, but begins to saturate to a constant value over time delays. But how much of this is due to the steep density profile originally assumed is unclear, and this may account for some of the modelled increase in conversion efficiency. Measurements of the reflected energy by *Brenner et al.* [58] have since shown that the reflected energy fraction remains approximately constant for all pulse delays up to 4 ps, indicating that the mechanism is not reliant on the enhanced laser energy absorption in reality.

Brenner et al. [59] went on to show that by complementing MPSA with thinner targets than that used by *Markey et al.*, that the laser to proton conversion efficiency can be increased to 15%, the highest conversion efficiencies for laser driven ion acceleration reported in the literature to date.

From the point of view of practicality, the process of delivering collinear pulses is attractive, as this can easily be achieved by a simple modification to the laser delivery. This does not require any additional alignment procedures than for a flat foil interaction, which lends itself to high repetition rate delivery, which will be mandatory for future applications.

2.4.3 Radiation pressure acceleration mechanisms

Several mechanisms proposed in the literature rely on the radiation pressure directly from the laser to accelerate electrons to relativistic velocities. *Esirkepov et al.* [60] proposed a mechanism by which all electrons are expelled from the target as they are accelerated in a single cycle of a relativistic pulse by the $\mathbf{j} \times \mathbf{B}$ mechanism. As radiation pressure continuously pushes the electron critical surface over the pulse duration, the accelerating potential is maintained, and sheath acceleration suppressed. If the laser uniformly irradiates an extended area of the foil in the region of 25 μm full width at half maximum, and the ion acceleration is sufficiently quick, instability growth rates can also be suppressed. This is known as the light sail mode of radiation pressure acceleration (RPA). The hallmark of this mechanism is the quasi monoenergetic ion spectra which it produces, which

has drawn interest from the many applications that would require this from a laser driven ion source.

In the way which the mechanism has been described here, a relatively high laser intensity of 1.2×10^{23} Wcm^{-2} must be achieved for a linearly polarised laser pulse. *Robinson et al.* [61] however, were able to show by computational simulation, that by using a circularly polarised beam to suppress the $\mathbf{j} \times \mathbf{B}$ heating, the steady ponderomotive force of the laser could steadily acceleration the electrons such that RPA could be observed apart from TNSA at lower intensities in the $> 10^{20}$ Wcm^{-2} range.

The onset of this mechanism has been observed experimentally for both carbon ions [62], and more recently protons [63] , which appears to show features of RPA proton spectra at energies of 10 MeV. For the 10^{20} Wcm^{-2} laser intensity that was used to produce these beams, the energies are low compared to that which can be delivered by TNSA at the same intensity, however an attractive feature of radiation pressure acceleration in general is that the ion energies scale as $\propto I_l$ in the relativistic regime, as opposed to the TNSA mechanism scaling of $\propto (I_l \lambda^2)^{1/2}$. As laser intensities become higher in the future, this mechanism may deliver the monoenergetic hundreds of MeV proton energies that are required for medical applications.

While the light sail RPA mechanism requires ultra thin targets to achieve acceleration of a monoenergetic ion population, shock acceleration [64] can give similar proton distributions in thicker targets. The mechanism again relies on the radiation pressure of the laser being sufficient to drive an electron population, but this time, instead of going through the whole target, the electrons are driven into the bulk of the target. Strong charge separation drives an ion bunch into the target, creating a collisionless electrostatic shock travelling through the target material.

Considering the interaction from the shock frame, bulk target ions stream toward the shock at the shock velocity, v_s. On colliding with the shock the ions gain a further $\frac{1}{2} m_i v_s^2$ from the collision, and so the maximum velocity that an ion

can gain from the mechanism is $2v_s$. A full consideration of the mechanics gives the maximum ion energy from the mechanism to scale as in equation 2.32, given by *Robinson et al.* [65].

$$K_i = \frac{2I}{n_i c} \tag{2.32}$$

This shows that for this mechanism, the highest energies come from near critical density plasma. While it is difficult to find targets with densities near critical for 1 μm wavelength lasers, the lowering of the critical density to 10^{19} cm^{-3} for carbon dioxide lasers makes gas targets suitably close to critical density. *Palmer et al.* [66] obtained quasi monoenergetic ion beams using such a configuration, at 1.1 MeV and energy spread of 4.2 %. This was implemented using the terawatt CO_2 laser at Brookhaven National Laboratory, where an upgrade is currently under way to increase the peak power to 100 TW, potentially offering the possibility to accelerate monoenergetic ion bunches to over 100 MeV.

Chapter 3

Experimental and numerical methods relevant to laser driven ion acceleration

Despite the months to years of preparation and interpretation that go into them, the laser plasma interactions which are the subject of this thesis take place on timescales which border on the inconceivably short. In order to interpret the physical mechanisms at work, the detectors which are chosen to glimpse these fleeting interactions must be reliable and well understood. This is especially the case, as highly competitive access to the most cutting edge laser facilities means a limited number of shots are available for each experiment and cannot be readily repeated.

By the nature of the interactions, time integrated measurements are usually made. By matching the results to those obtained from numerical modelling, computational simulations are often used to provide an insight into the temporal dynamics of the interactions.

In this chapter, the experimental and numerical methods relevant to this thesis are introduced along with the laser systems that are used to initiate the interactions.

3.1 Ultrahigh intensity lasers

It is no surprise that ultrahigh intensity lasers, share much in common with the lasers of introductory textbooks. A laser photon can be amplified in a coherent manner if its electromagnetic field acts on a population inverted gain medium, if the energy of the gain medium band gap matches that of the laser photon. This is the process of stimulated emission and is the central principle upon which most lasers are based. Ultrahigh intensity lasers are not, however, the monochromatic, continuous wave lasers generally represented by this model.

In the experiments reported in this thesis, the lasers typically contain around 100 J of energy, compressed into sub picosecond pulse durations. Esoterically, a pulsed laser requires a superposition of around 10^5 longitudinal modes, resulting in a frequency bandwidth. This frequency bandwidth is central to the chirped pulse amplification technique which enables amplification to ultrahigh intensity. However, in the pursuit of high energy gain, this technique causes some of the ideal pulsed intensity profile to be sacrificed. This leads to the introduction of the concept of temporal contrast, and the various sources of this are discussed.

Here, a broad overview of this most relevant laser technology is presented.

3.1.1 Chirped pulse amplification

Chirped pulse amplification (CPA) [5] was designed to circumvent the issue that amplification of laser pulses can result in damage of optical components, as the beam fluence begins to reach the optics damage threshold. Even below the damage threshold, effects due to the nonlinear refractive index of a material, η_2, such as B-integral accumulation [67], according to equation 3.1, can result in deformation of the pulse phase front. This causes self focussing in the optics, and if propagated through a long enough distance can lead to component damage.

$$B_{\int} = \frac{2\pi}{\lambda} \int \eta_2 I(z) dz \tag{3.1}$$

The obvious solution is to reduce the fluence by increasing the beam radius. However, increasing the sizes of the optical components with it *ad absurdum* soon becomes prohibitively expensive and a more general solution is required. CPA is that general solution, and involves stretching the frequency components of the laser pulse in time, known as a chirp. The frequency bandwidth of the laser makes this possible, and the frequency dependent stretch is most often introduced by a grating pair known as a stretcher. To introduce a positive chirp to the pulse, a configuration is chosen such that longer wavelength components take a shorter path through the stretcher, while the shorter wavelength components take a longer path. In the PHELIX laser, the pulse is stretched to tens of thousands of times its original length using this technique.

Due to its now reduced intensity, the temporally longer pulse can safely be amplified without suffering the adverse effects associated with higher intensity pulses. While the energy density of the pulse is still limited to similar levels of the non chirped pulse, the total energy of the stretched pulse is much larger.

The final step in the CPA technique is to compress the stretched pulse using a complementary pair of optical gratings to those in the stretcher. In practice, the gratings are larger in size to avoid damage from the pulse. In this way a higher power pulse than by conventional amplification can be achieved.

3.1.2 Contrast

Due to inherent imperfections in the amplification techniques used, three main defects are delivered in tandem with the main pulse, as summarised in figure 3.1. Briefly, the sources of these are reviewed.

The amplified spontaneous emission (ASE) pedestal is a result of excited atoms in the pumped amplifiers spontaneously decaying to the lower energy state, rather than being stimulated to decay by a coherent laser photon. With this process being random in nature, the photons are emitted over 4π steradians. With the laser chain being a finite length, a significant fraction of the light can remain

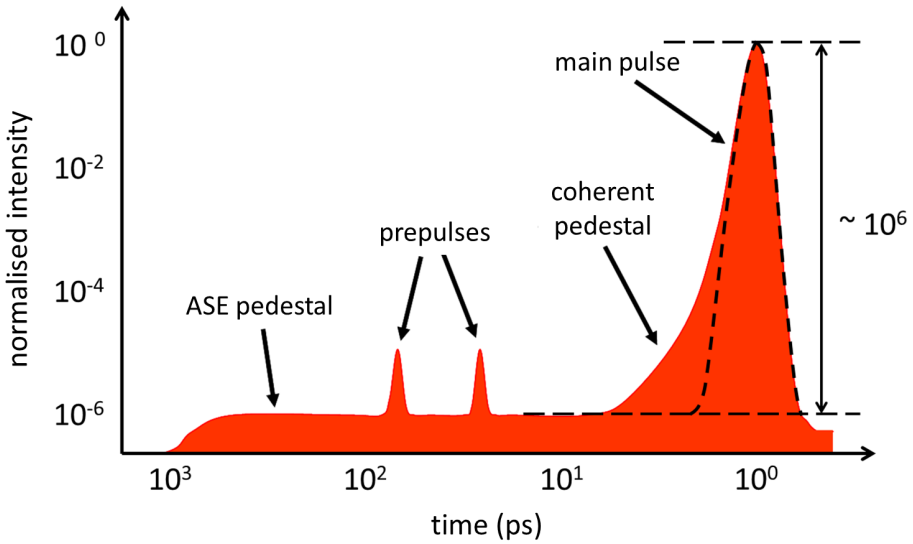

Figure 3.1: A schematic outlining the main contributors to laser contrast, and their typical time scales and intensity levels at which they occur in a chirped pulse amplified ultrahigh intensity laser system. Adapted from *Carroll* [54]

in the system, and these spontaneously emitted photons can go on themselves to become amplified. With laser intensities in this thesis reaching up to 10^{19} Wcm^{-2}, and the damage threshold of many target materials being around 10^{12} Wcm^{-2}, one amplified spontaneously emitted photon, per ten million laser photons can constitute this significant fraction.

This fraction of the instantaneous intensity relative to the intensity of the main pulse is known as the intensity contrast level, and is found to vary depending on the time prior to the main pulse arrival. It is therefore usually quoted both as a ratio and the time at which the ratio is measured to take this value.

An intrinsic source of ASE in the laser system arises from the use of regenerative amplifiers [68], which are found in the front end of some laser systems. In a regenerative amplifier, the signal beam, which is to be amplified, is passed through a gain medium multiple times on a closed path, in order to achieve high gain in the early stages. However, by confining the beam to a closed path, the random ASE emission is also confined, and upon the multiple encounters with the gain medium also provides the ASE with an environment to be amplified to high gain. It is also worth noting that contrary to the signal amplification which

occurs only in the direction of signal travel, ASE can be accumulated by travelling in counter propagating directions, because of its random nature of emission.

It is possible to optically shutter much of the pulse ASE up to around a nanosecond prior to the main pulse via Pockels cells. However upon recompression of the pulse, this still leaves the incoherent ASE as an intensity pedestal, which can act upon the target for the comparatively long nanosecond timescale prior to the picosecond main pulse arrival.

Additionally, various sources of unwanted lasing arise in the laser chain from internal reflections from various optical components and give rise to prepulses in the laser temporal contrast trace. These might be eliminated by introducing wedge shaped optics for example.

Finally, on the order of the laser pulse duration, scattered light from the diffraction gratings of the stretcher, which is amplified in the laser chain, leads to the introduction of a coherent component in the contrast trace, sometimes referred to as uncompensated dispersion or the coherent pedestal [69].

3.2 PHELIX laser

All of the data in this thesis was obtained on the Petawatt High Energy Laser for heavy Ion eXperiments, PHELIX [70], at the Gesellschaft für Schwerionenforschung, GSI, facility in Darmstadt, Germany. A brief description of the laser setup and optional modules that were used follows, and a simple schematic of the laser and target area layout are given in figure 3.2. To deliver the high energy short pulsed laser that is required for ion acceleration experiments, the laser undergoes the now standard technique of CPA.

The femtosecond front end of the laser begins with a commercially available *Coherent Mira* oscillator. A continuous wave *Coherent Verdi* is used to pump the titanium doped sapphire oscillator crystal and this delivers a 100 fs duration pulse with a total energy of 4 nJ. From this point, the pulse can be passed through the stretcher, or the optional ultrafast optical parametric amplifier (uOPA) [71] mod-

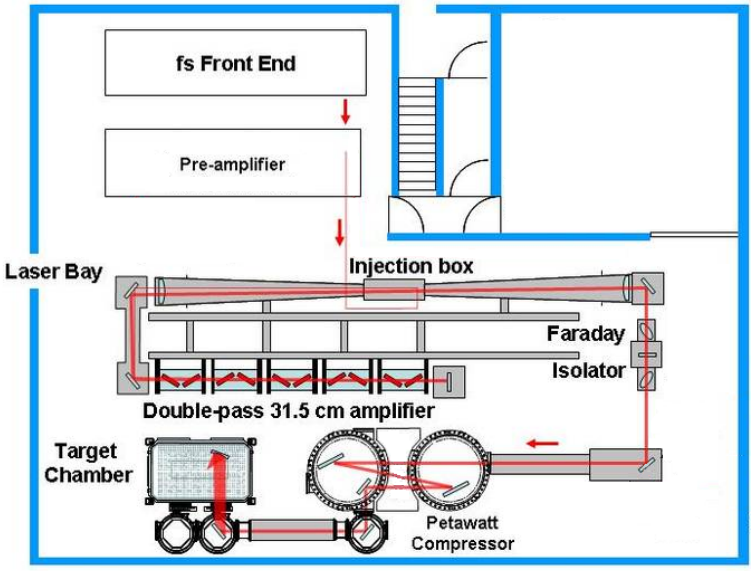

Figure 3.2: Schematic of the laser and target area at PHELIX, adapted from [73]. This shows the recently upgraded target chamber, while the experiments reported in this thesis used the target chamber prior to this installation, where the final turning mirror shown here was the position of the off axis focussing parabola.

ule prior to stretching, which is a recent development in the PHELIX beamline, made available late in 2012.

Wagner et al. [72] have shown that by employing this module, the contrast can be enhanced and is tunable from $10^7 - 10^{10}$ at 100 ps, to bring the contrast in line with requirements for the recent upgrade to the facility which can now deliver 10^{21} Wcm^{-2} pulses. Chapter 6 is concerned with using the uOPA module, while it was not available for the experiments described in chapters 4 and 5. Some more detail on the uOPA module at PHELIX is given in section 3.2.1.

After the pulse is stretched to a duration of 2.4 ns, two Titanium doped sapphire, linear and ring regenerative amplifiers, respectively, intensify the pulse to deliver a output beam of 30 mJ at 10 Hz repetition rate. It is at this point that the beam is passed through the double pulse generator described in section 3.2.2, which was used in chapters 4 and 6.

The pulse or pulses are then further amplified using three neodymium doped glass amplifiers in the preamplifier section of the laser, which is capable of increasing the pulse energy up to 2 J. At this stage the beam also encounters a

deformable mirror which is coupled to a Shack-Hartmann wavefront sensor at the end of the amplification chain. This acts to correct spatial aberrations introduced by the preamplifiers and main amplifiers.

Up to this stage, the laser chain can be operated at a repetition rate of a shot every two minutes, whilst maintaining good beam quality. This mode of operation was employed in chapter 4 to enable an extensive data set to be obtained of a plasma mirror system characterisation, in a shorter time.

The final amplification stage, which was used in the other results chapters, is a double pass flash lamp pumped neodymium doped glass amplifier. This is capable of delivering pulses of 250 J, however, radiation safety rules limit the deliverable energy to 120 J. The compressor chamber then returns the pulse to its gain narrowed bandwidth limit of 500 fs.

On focussing by an $f/9$ off axis parabola, to typically a 15×20 μm spot in the target chamber, maximum intensities of 10^{19} Wcm^{-2} are achieved.

3.2.1 Optical parametric amplification at PHELIX

Optical parametric amplification (OPA) relies on an amplifying crystal which has a second order nonlinear optical susceptibility. Here, the signal pulse, which is the pulse that is required to be amplified, is passed through the crystal at the same time as a higher frequency pump pulse. The interaction of these two waves in the crystal medium results in the pump photon being converted into a second signal photon which is coherent with the original signal photon. Any excess energy from the pump photon and signal photon is output as a third photon, called the idler, at a frequency which conserves the energy. This is summarised in equation 3.2.

$$\omega_{pump} = \omega_{signal} + \omega_{idler} \tag{3.2}$$

As the idler photon can take any frequency that satisfies equation 3.2, the whole bandwidth of the signal pulse can in theory be uniformly amplified. This is one very clear advantage of this technique over conventional amplification, which

is strongly affected by gain narrowing in the amplifiers. Efficient recompression of the stretched pulse of an OPA system has been observed in experiment [74], and the technique offers a path to significantly reduce the laser pulse duration.

The potential for OPA to enhance the laser contrast is equally attractive. As parametric amplification does not rely on the pump energy being stored in the medium, as a conventional amplifier requires via a population inversion, the probe pulse is only amplified when the pump pulse is present. In practice, the pump photons alone interacting with the nonlinear crystal can spontaneously decay into signal and idler photons, in a process termed parametric superfluorescence [71]. These spontaneously created photons can undergo similar amplification in the crystal to the true signal photons, and so these photons can themselves generate an ASE pedestal of their own. The pedestal can only be generated on the timescale that the pump beam interacts with the crystal, and so in minimising this time, the contrast level can also be optimised. This is the concept of ultrafast OPA as employed at PHELIX, where the pump pulse duration is on the order of a picosecond.

The setup at PHELIX allows the uOPA module to be used prior to the CPA in a process known as optical parametric chirped pulse amplification (OPCPA) [75]. The beam layout is designed such that the pulse undergoes OPA before being passed through the regenerative amplifiers which are the major source of ASE in the system. It follows that if the uOPA module is used to deliver a higher energy input signal pulse to the regenerative amplifiers, the amplification of the regenerative amplifiers can be reduced accordingly to deliver the same energy as without the uOPA module. This results in a reduction in the ASE level in the regenerative amplifier, and therefore an improved contrast level. Because the gain in the uOPA is tunable by adjusting the strength of the pump beam, by using the same compensatory means in the regenerative amplifiers, the contrast level of the system as a whole is tunable [72].

3.2.2 Double pulse generator

A double pulse can be generated by the setup shown on figure 3.3. The front end pulse is passed through a half wave plate, the rotation angle of which determines the intensity ratio of the two beams before they travel on to a polarising beam splitter. The transmitted fraction, which becomes the main pulse, contains the bulk of the energy and is delayed relative to the reflected beam. The transmitted beam path traverses a series of mirrors on a translation stage, which are used to control the relative time delay.

As the fixed path prepulse fraction of the system initially is orthogonally polarised relative to the main pulse, a second half waveplate is necessarily introduced to this beamline to match the polarisation to that of the post pulse. The beams converge at a second beam splitter which realigns the beams to the same path through the rest of the system.

The time delay between the pulses is characterised using a single shot autocorrelator. The pulses can be overlapped in time using this technique within an error of $\sim$ 200 fs. The motorised delay stage could introduce a $\pm$ 4 ps delay between pulses whilst maintaining linearity between drive position and the time delay on the autocorrelator. At a nominal delay of 4 ps the maximum error associated with the pulse delay is $\pm$ 500 fs, corresponding to a time delay error of $\pm$12 %.

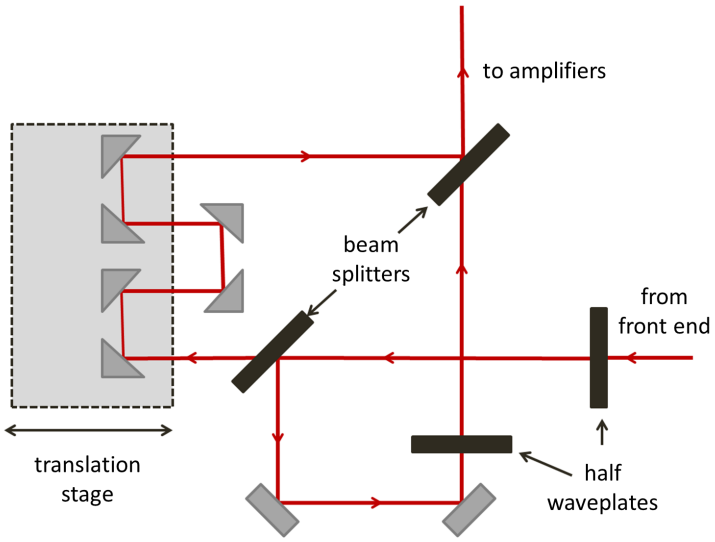

Figure 3.3: Schematic of the double pulse generator

3.3 Ion diagnostics

Laser driven ion acceleration is the main theme of this thesis, specifically proton acceleration, which are the preferentially accelerated species in the laser driven approach. Here, radiochromic film for proton detection and the Thomson parabola ion spectrometer are introduced. Ions are known to deposit energy into materials according to the Bethe-Bloch relationship, which dictates that the stopping power of an ion is proportional to the square of its charge and inversely proportional to its velocity as given by *Ziegler* [76], in equation 3.3.

$$\frac{dE}{dx} = \frac{4\pi e^4}{m_i v_i^2(x)} Z_i^2 Z_{targ} \ln\left(\frac{m_i v_i^3(x)}{Z_i e^2 \omega_e}\right) \tag{3.3}$$

In general, as an ion slows in a material, its stopping power is increased, leading to the ions depositing more energy per unit distance the further that they travel into a material. The result is the characteristic Bragg peak in which ions deposit their energy, as shown in figure 3.4. This was obtained on the Monte Carlo based simulation package, Stopping Ranges of Ions in Matter (SRIM), which is a widely used software package that can be used to model the energy deposition of ions in a range of target materials [76].

3.3.1 Radiochromic film

Radiochromic film (RCF) is a self developing dosimetry film with an active layer consisting of a colourless chemical monomer which when exposed to ionising radiation reacts to form an optically dense polymer. The optical density, OD is related to the transmitted fraction, I_{trans}, of incident light, I_0 through a material, as in equation 3.4, and is proportional to the absorbed dose and therefore the incident proton flux.

$$OD = \log_{10}\left(\frac{I_0}{I_{trans}}\right) \tag{3.4}$$

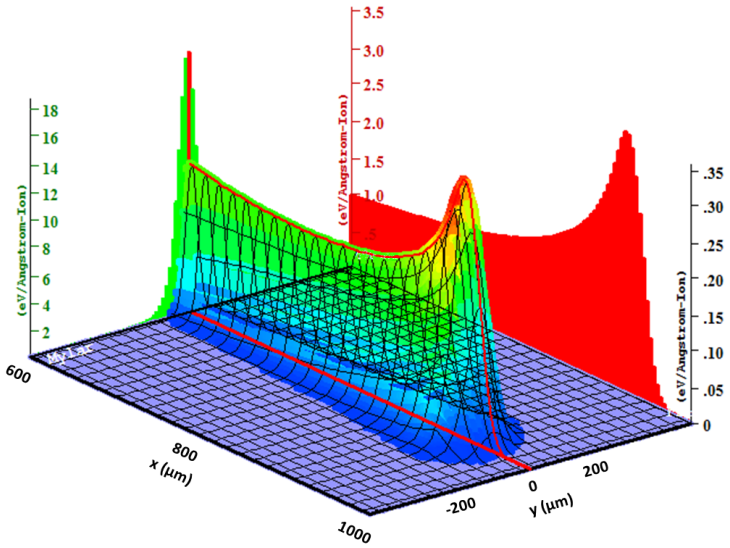

Figure 3.4: The Bragg peak of a 10 MeV proton beam travelling in the x direction as it deposits its energy in a Mylar target, obtained from SRIM. Projections on to the axes show the form of the peak and the line integrated energy deposition. Each cell is 40 $\times$ 40 μm.

RCF is particularly suited as a diagnostic of laser accelerated ions as the response appears to be independent of dose rate [77]. Therefore, if RCF is exposed to a known dose via a monoenergetic cyclotron accelerated proton beam for example, the optical density of the film can be absolutely calibrated, and used for extracting proton doses from laser produced ion beams.

Circa 2011, the manufacturers of RCF, Gafchromic, discontinued the manufacture of the HD 810 type of film, and introduced a similar film, HD V2, both of which are used in this thesis, and the layer composition of each type of RCF is shown in figure 3.5. Both film types are similar in structure, with a thin active layer being backed by a polyester substrate for stability. The composition of the active layer of these films is undisclosed, but spectrophotometry indicates the active layer has been modified, with the HD V2 exhibiting an absorption peak in the blue end of the spectrum, shown in figure 3.6. This results in the films taking a different colour, but their general response is similar.

The manufacturers advice for extracting RCF dose from the HD 810 film, is to illuminate it with a narrow bandwidth light emitting diode of wavelength

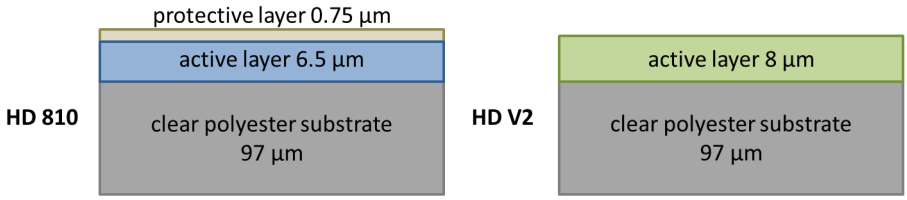

Figure 3.5: The layering structure of the two types of radiochromic film, Gafchromic HD-810 (left) and HD-V2 (right).

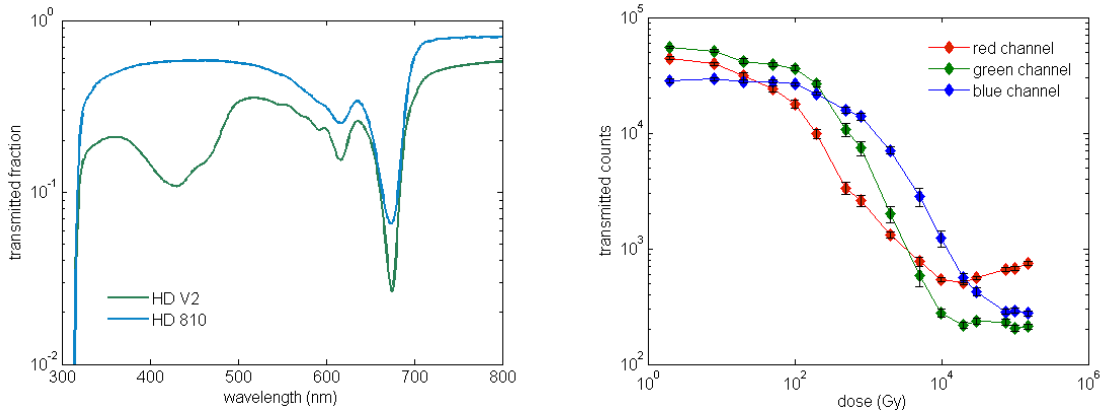

Figure 3.6: (left) The transmission spectra for exposed HD 810 and HD V2 films across the visible spectrum. (right) The transmitted counts of each colour channel in the flatbed scanner as a function of exposed dose on the HD V2 film. Error bars represent the variance across the central region of interest.

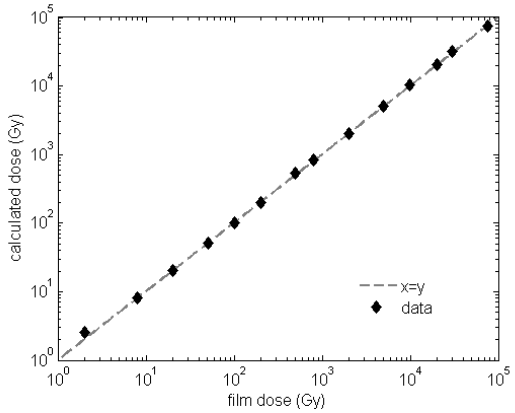

Figure 3.7: By using the three colour channels a good degree of linearity between calculated dose and film dose can be found. For HD V2 a root mean square error across the dose range of 2 Gy -75 kGy of 5 % is obtained.

around 660 nm as this coincides well with a prominent absorption peak in the film, shown in figure 3.6. This technique is recommended provided the RCF has been exposed to a dose in the range of 10 Gy to 400 Gy. However, with doses well in excess of this regularly deposited in the films in laser driven ion acceleration experiments, the optical density of the film in this region of the spectrum become large before reducing for even higher doses. This response is unacceptable for reliable dose extraction, with multiple doses having the same measured OD, and so the response of other areas of the spectrum can be explored to find a more appropriate, monotonic response to dose.

A flat bed transmission scanner serves as a powerful, off the shelf, solution to this problem [78]. The transmission scanner consists of a light emitting diode array, at three wavelengths of 643 ± 15 nm, 532 ± 20 nm and 474 ± 11 nm [79], on one side of a transmission tray, which is loaded with RCF. A charge coupled device on the other side of the tray measures the transmitted intensity of each light emitting diode. When scanning in 16-bit colour, the transmitted counts measured for each colour channel are given in figure 3.6, and this can be converted into optical density.

To extract a dose from the films there are two key criteria. Firstly there must be a large enough change in the optical density with increasing dose that the increase can be reliably measured. Secondly, the dose deposition must bear a monotonic relationship with the measured optical density in this region, otherwise the dose extraction will be ambiguous. This dose to scanner response is shown in figure 3.6.

Each colour channel is observed to have differing responses according to this criteria, making each colour channel of the spectrum suitable for extracting doses in different ranges. The red channel for example responds with a large change in optical density at low doses, while it exhibits non monotonic behaviour at doses exceeding a few hundred Gray. This makes it useful for extracting low doses from the films. The blue channel shows little to no change in optical density until the films are exposed to in excess of hundreds of Gray, but maintains a

monotonic response up to tens of thousands of Gray, making this channel useful for extracting high doses.

The range in doses that can be reliably extracted from each channel is referred to as its dynamic range. On their own, each channel has a limited dynamic range, but by combining the measurements from each channel the dynamic range of the film ranges from a few Gy to tens of kGy. Specifically, this method can be used to reliably extract doses from 0.5 Gy - 31 kGy using the HD 810 films and 2 Gy -75 kGy using HD V2 films, as shown if figure 3.7.

With protons depositing their energy in a Bragg peak, the width of each RCF active layer may be considered to be dominated by the stopping of a narrow range of proton energies. Therefore if several layers of RCF are stacked on top of each other, each RCF layer predominantly samples a different energy range of the proton energy spectrum in a technique dubbed radiochromic film imaging spectroscopy [80]. The exponential TNSA proton spectra are particularly conducive to this.

Here the proton spectrum can be fully deconvolved if the contributions of the higher energy protons are subtracted from each RCF layer, with the spectral resolution proportional to the number of RCF layers in the stack. The added benefit to this technique is that in addition to obtaining proton spectra, a high spatial resolution two dimensional profile of the beam is obtained.

The contribution of heavier ions can usually be effectively removed by introducing a thin aluminium foil layer to the front of the stack. Equation 3.3 shows that this preferentially stops high Z, lower energy ions.

On the RCF layers which sample the lower energy protons, it is not uncommon to find some that this layer is saturated with signal. Particularly, for the lower dynamic range HD 810 type film, which found to have a maximum recoverable dose of 31 kGy using the flatbed scanner technique, and this problem was encountered by *Brenner et al.* [59].

For this purpose RCF was exposed to a controlled dose of up to 202 kGy at the cyclotron source at the University of Birmingham. To give the best possible

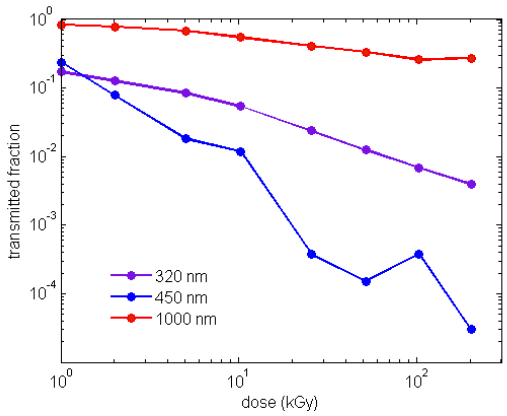

Figure 3.8: Spectrophotometer transmittance as a function of dose for HD 810 in three regions of the spectrum.

chance of identifying a region of the spectrum where the recoverable dynamic range may be increased, the RCF was scanned using a Shimadzu UV-1800 spectrophotometer across the wavelength range of 190 nm to 1000 nm.

The spectrophotometer transmittance versus wavelength scans for a dose range of 1 kGy to 202 kGy are shown in figure 3.8. This shows a region in the UV part of the spectrum at 320 nm, where the optical density has a monotonic relationship and scales well with dose across the full range up to and including 202 kGy. The maximum measurable dose in the UV region may well exceed this value but we are unable to verify this as we do not have a higher exposed dose calibrated film.

By backlighting the film with a UV source and using appropriate filtering, dosimetry can be made that would be otherwise irretrievable using the flatbed scanning technique. This was my contribution to the article published in *Physica Medica* by *Bolton et al.* [81], and the technique has since been used by *Brenner et al.* [59] to report record conversion efficiencies of laser to proton energy of 15 %.

3.3.2 Thomson parabola ion spectrometer

While RCF provides some discretised spectral information on the laser accelerated proton beams, the Thomson parabola ion spectrometer is the most commonly deployed spectrometer for laser accelerated ion beams, which provides high energy resolution, continuously sampled spectra. The Thomson parabola also provides a practical solution for sampling light and heavy ion spectra.

A schematic of the Thomson parabola ion spectrometer designed by *Carroll et al.* [82] is given in figure 3.9. The diagnostic is aligned, with the zero deflection axis along a clear line of sight to the interaction. When positive ions, electrons and neutrals stream toward it, from the interaction some of the species travel through the lead pinhole at the front of the detector. The function of the pinhole is both to limit the flux on the detector medium, preventing saturation of the signal, and also defines the energy resolution of the detector, as spatially separated species of equal energy will experience a displacement difference when travelling through the electric and magnetic fields. Typically a pinhole 10's of microns in diameter gives a good compromise between signal and resolution.

A pair of permanent NdFeB magnets, separated by 10 mm are used to create magnetic fields in the region of 0.1 - 1.0 T, dependent on the field strength of the individual magnets used. The purpose of this is to disperse the ions according to their energy. For any given species, the higher energy ions have a larger Larmor radius than the lower energy ions, and so they experience less deflection in the magnetic field, therefore each species is dispersed by the magnetic field in the $\mathbf{v}_i \times \mathbf{B}_{magnet}$ direction by a distance proportional to its energy.

The ion species are deflected in the magnetic fields according to both their energy and charge to mass ratio, however, all positive species experience a deflection in the same direction by the magnetic field. The few kV electric field applied across the plates provide a second deflection of the ion species, orthogonal to that caused by the magnetic field, in the direction of the applied electric field.

The result is that each ion species is separated according to their charge to mass ratio and energy in parabolic paths at the detector plane, where the ion

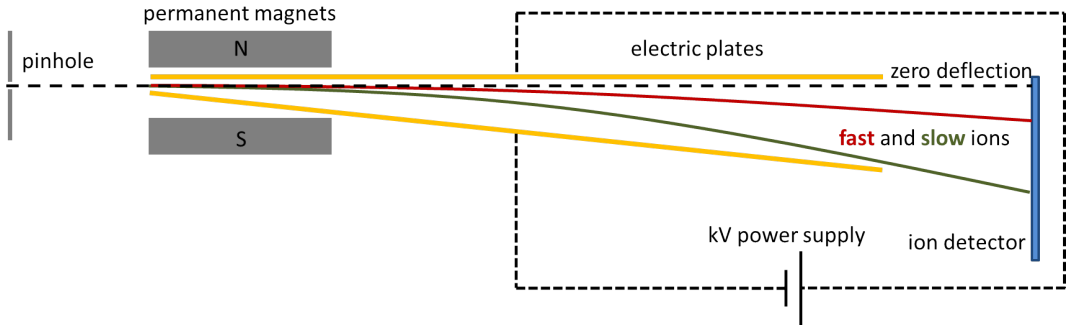

Figure 3.9: Schematic of the Thomson parabola ion spectrometer.

energy is proportional to its deflection in the magnetic field.

Photons and neutral particles, which travel along the zero deflection axis of the detector, provide a useful reference point for calibration.

The main problem with the Thomson parabola is that the solid angle sample size is very small, and so where proton beams are observed to have strong variation in the angular profile, caution must be exercised as the Thomson parabola trace may not be representative of the proton beam as a whole. To mitigate some of this concern, it is possible to use the Thomson parabola in conjunction with the RCF detector, to measure the proton beam uniformity, and it is possible that the Thomson parabola line of sight can be taken through a small hole bored in the RCF detector stack.

3.4 Plasma mirrors

Although the contrast of a laser system is determined by each individual laser setup, and largely outwith the control of the experimenter, the plasma mirror [83] is a tool that can be incorporated into the experimental configuration and enables the contrast level to be enhanced by more than two orders of magnitude. The cost of employing a plasma mirror is often a reduction in the energy delivered to the target, in the region of 15-30 % per plasma mirror interaction, and therefore a reduction in interaction intensity. This is dependent on the polarisation of the plasma mirror interaction, which may or may not be practical to alter in the experimental setup.

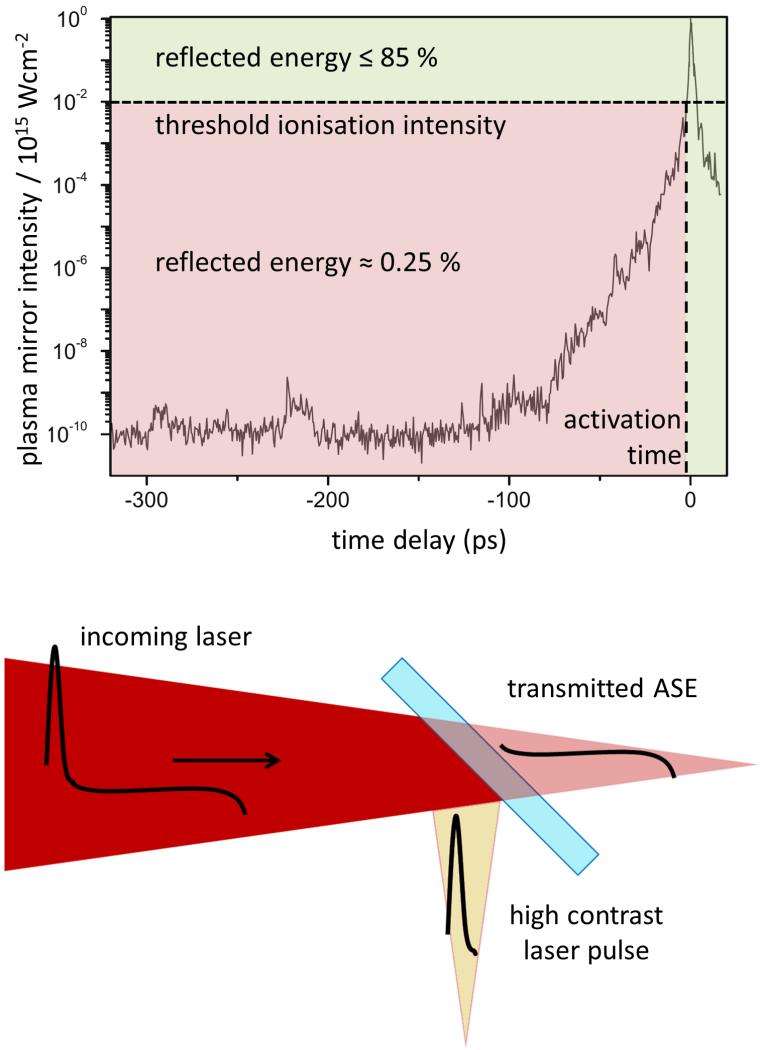

Figure 3.10: The contrast trace of the PHELIX laser with the uOPA front end, adapted from *Wagner et al.* [72]. Prior to the laser intensity reaching the threshold for ionisation of the plasma mirror, the reflected energy fraction is determined by the optical coating on the plasma surface, and so the bulk of the energy of the ASE is transmitted through the plasma mirror. After the plasma mirror is ionised, the bulk of the reflected energy is reflected. Depending on the picosecond contrast level, this change in reflected energy fraction can take place rapidly, on the order of picoseconds prior to the pulse maximum intensity.

The plasma mirror is essentially a dielectric (glass) slab, with an anti reflective coated surface, which typically reflects around 0.25 % of the incident light at the laser wavelength, when being operated at an intensity below its ionisation threshold. In chapter 4, this intensity is found to be in the mid 10^{12} Wcm^{-2} range. Above these intensities, the plasma mirror exhibits an intensity dependent reflectivity, which is found to peak around 10^{15} Wcm^{-2}. The detailed reflectivity of the plasma mirror is highly dependent on the spatiotemporal intensity profile of the laser pulse.

This effective threshold ionisation intensity means that the spot size on the plasma mirror can be chosen such that the maximum incident intensity reaches that for which the maximum reflected energy fraction is gained. Subsequently, where the incident intensity on the plasma mirror is low, as with the ASE, the bulk of the laser energy is transmitted through the plasma mirror. The steeply rising intensity profile at the few to tens of picoseconds time prior to the main pulse can be tuned to have fast switch on times, where only the main part of the pulse experiences the high reflectivity plasma mirror surface. Figure 3.10 shows this for a real contrast trace obtained from the PHELIX laser [72].

The widespread use of plasma mirrors for contrast enhancement has led to several characterisation investigations [83, 84, 85]. These have shown that as well as verifying the intended contrast enhancement that the plasma mirror can also act as a spatial filter, due to variations in the spatial intensity profile of the pulse.

Time resolved reflectivity measurements have also been published by *Nomura et al.* [86, 87], and this is dealt with in more detail in chapter 4, where the reflected energy and beam spatial profile is investigated in the double pulse regime.

3.5 Numerical modelling

One of the most powerful tools for the modern laser plasma experimenter is numerical modelling. Because a single interaction spans a few picoseconds, multiple measurements on the single shot time frame can be difficult and impractical with current technology. What is often recorded experimentally, is a time integrated measurement of the whole, highly nonlinear interaction. However, if experimental measurements can be reproduced via numerical modelling, then this can be examined at finer resolution in time and space to provide some insight into the mechanisms at work in the experiments.

Over the years, with confidence in the numerical models growing, some have seen to use modelling as a predictive tool for experiments, with varying success underpinned by the validity of the assumed experimental conditions. A symbiotic relationship between the two approaches has developed and the best understanding may emerge from using both.

3.5.1 Particle in cell

In the high density, and collisionless regime of interest to much of this thesis, particle in cell (PIC) simulations have become the numerical modelling method of choice. An attractive feature of PIC is that it presents a viable approach to modelling these conditions, based only on some very limited assumptions of the initial experimental conditions, and evolve according to the well known electromagnetic laws. The Extendable PIC Open Collaboration (EPOCH) project [88], has recently delivered a PIC code for the academic community, making these tools more widely available. A basic discussion of the PIC code procedure and some considerations follow.

A fully kinetic approach to describing the evolution of the system would be to solve the Fokker-Planck equation, equation 3.5, for each species, which is described by a distribution function, $f_{VFP}(\mathbf{r}, \mathbf{p}, t)$, and where collisions between species, $C(f)$, are also accounted for. Often, when dealing with laser plasmas,

fixed ionisation state and collisionless plasmas are assumed, and so the collision term is assumed to become zero, in which case the Vlasov equation is attained. Maxwell's equations can be used to progress the electric and magnetic field of equation 3.5 to model the evolution of the system, by using a finite differencing approach, where the distribution function is mapped to a grid.

$$\frac{\partial f_{VFP}}{\partial t} + \mathbf{v}\frac{\partial f_{VFP}}{\partial \mathbf{x}} + q\left(\mathbf{E} + \mathbf{v} \times \mathbf{B}\right)\frac{\partial f_{VFP}}{\partial \mathbf{p}} = C(f) \tag{3.5}$$

The most commonly cited problem with the method of solving the Vlasov equation in this way is that the size of the distribution function soon becomes very large and computationally intensive, with the function being six dimensional at each grid point. Aside from reducing the dimensionality of the simulation, the size of the problem can be reduced by following the evolution of a relatively small number of macroparticles which themselves approximate the distribution function of a cloud of many particles of a given species. These macroparticles therefore occupy a finite volume and have a shape, as they represent a large number of *real* particles, but are assumed to have no internal degrees of freedom. The macroparticles being free to travel to any point in space can be mapped onto spatial grids, or a set of cells, and this forms the fundamentals of the PIC approach to modelling the evolution of an electromagnetic system. A brief summary of the PIC approach follows, and a schematic of its evolution is presented in figure 3.11 to aid the description. A comprehensive discussion of the PIC method is given by *Birdsall and Langdon* [89].

Each macroparticle which has an associated mass and charge is initiated with a position and velocity at the beginning of the simulation, $\mathbf{r}_i, \mathbf{v}_i$, and is mapped onto a grid by some assumed shape function of the particle. This allows the charge and current densities, $\rho_g, \mathbf{j}_g$, to be calculated at each grid point. When these quantities are known at each grid point, Maxwell's equations can be solved to find the self generated electromagnetic fields of the plasma at each point on the spatial grid, $\mathbf{E}_g, \mathbf{B}_g$. When the collective field contributions of each macroparticle

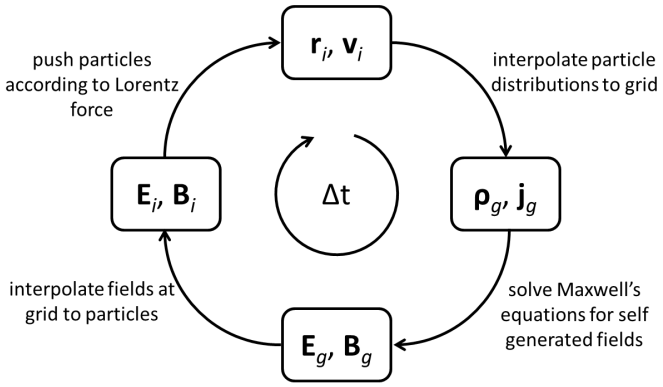

Figure 3.11: Schematic summarising the steps involved in solving the particle in cell algorithm. Adapted from *Birdsall and Langdon* [89].

have been calculated, the fields are then treated self consistently, and the particle motion can be progressed according to the Lorentz force for a time duration where the particle has a new position and velocity $\mathbf{r}_{i+1}, \mathbf{v}_{i+1}$. The process is iterated over many time steps to model the evolution of the system.

In pursuing this approach, several non physical quantities have been assumed or introduced and a sensible approach to quantifying these needs to be considered. Firstly, the space and time dimensions have been discretised. In order for the code to remain stable, the timestep must be sufficiently small that the fastest oscillations in the simulation are resolved, and this is usually determined by the electron plasma frequency. The grid is usually discretised into segments of the order of the Debye length of the plasma.

As well as this the number of macroparticles must be chosen such that good statistics are retained throughout the simulation, and this is highly dependent on each individual simulation.

Advanced PIC codes such as EPOCH, allow some quantum processes such as ionisation to be modelled, however, in practice these require larger computational resources. For this reason they are usually not included, and with the resolution of the modelling being limited by the cell size, timestep and number of macroparticles, they are often only suitable for modelling up to a few picoseconds, for the relevant systems here.

Chapter 4

Plasma mirror lifetime characterisation by temporally controlled double pulse interactions

The post plasma mirror far field quality is measured as a function of its ionisation time, giving the first lifetime characterisation of this type. The measurement is enabled by implementing a temporally separate double laser pulse in an ionisation-probe fashion and measuring the probe pulse far field as a diagnostic of the quality of the reflected beam wave front. An analytical model of the expanding plasma mirror surface and its perturbations show the evolving optical quality is dependent on the incident quasi-near field laser intensity distribution.

The plasma mirror is found to remain of high reflectivity and optical quality for up to five picoseconds after its surface is initially ionised, reaching a maximum probe pulse reflectivity of 96 %, which is the highest plasma mirror reflectivity reported to date. It is proposed that the time dependent reflected energy fraction of the probe pulse is a product of the spatial and temporal ionisation processes being in competition with the preplasma absorption.

Since the time of examination, substantial development on this work has been published in *New Journal of Physics* [90].

4.1 Introduction

Over the past decade it has become increasingly apparent that for many branches of experimental laser plasma physics, not least in the field of ion acceleration [53], that laser contrast is as important an intrinsic parameter of a laser system as any. Debate continues over the optimum level of ASE for experiments, but consensus exists in that it must in principle be known and controlled in order to advance the interpretation of experimental laser plasma physics. The plasma mirror is a widely favoured tool that enables contrast to be enhanced by some experimentally measurable value from a previously known level. Many high power laser plasma experiments have employed the plasma mirror to date, with some studies being dedicated to understanding the characteristics of these optical switches [83, 84, 85].

Under certain conditions, the far field of the laser pulse has been measured to be of good quality after the plasma mirror interaction [85], and the time resolved reflectivity has also been measured up to ten picoseconds after a short pulse interaction [86]. However, there have been no direct measurements of the duration for which the plasma mirror surface retains its high optical quality. This lifetime measurement is of particular interest in the context of establishing the applicability of plasma mirrors in experiments utilising double pulsing techniques, which have been shown to notably enhance the conversion efficiency of laser energy into protons [57, 58, 91], and to provide an optical means of controlling the divergence of hot electron populations [92, 93, 94]. With multiple laser pulses also being shown to be more efficient at plasma channelling [95], double pulsing could conceivably be adopted by alternative acceleration mechanisms, such as the breakout after burner, which also benefits from high contrast laser pulses [96].

In this chapter, the simple double pulse generator from section 3.2.2 is used to deliver two pulses with tunable intensity ratio and temporal delay. An ionisation pulse, is introduced to activate the plasma mirror, and then by measuring the far field of the more intense, reflected probe pulse, whilst simultaneously measuring

the specularly reflected energy fraction, the optimum working conditions of the plasma mirror can be identified.

4.2 Experimental method

The experiment was carried out using the PHELIX laser at the GSI facility. A schematic of the experimental setup is given in figure 4.1 where the 12 cm apertured beam is focussed in an $f/12.5$ cone to the plasma mirror, in s-polarisation relative to the plasma mirror surface.

The plasma mirror is a BK7 glass substrate, with a SiO_2 and ZrO_2 double layer coating, which is optimised to be antireflective for 1053 nm at a 45° angle of incidence. The manufacturer quotes the reflectivity of this configuration to be less than 0.25 %, potentially offering a factor of a few hundred in contrast enhancement, and this is close to the 0.4 % experimentally measured, which suggest that in practice a factor of 250 in contrast enhancement is achievable.

After the plasma mirror interaction, energy needs to be dumped before the far field can be imaged safely, without damaging the CMOS detector. An uncoated wedge and blank transmit the majority of the energy through them, while the weaker, B-integral free, reflected beam is retained for imaging. The beam is first expanded for 44 cm to allow the fluence to drop below the damage threshold of the optics [97]. On reaching the 15 cm diameter, 80 cm focal length spherical mirror, the beam intensity is reduced by approximately two orders of magnitude and can be safely collimated using an achromatic lens, which delivers the beam to two diagnostic branches.

On the first branch, a magnifying telescope arrangement, filtered for the laser wavelength, is used to image the far field on an 8-bit CMOS camera, outside the chamber, while a Gentec pyroelectric power meter allows absolute calorimetry of the beam energy content on the second branch. While the power meter has a large dynamic range meaning no additional energy filtering was needed, the dynamic range of the CMOS camera is limited and so some optical filtering variable up

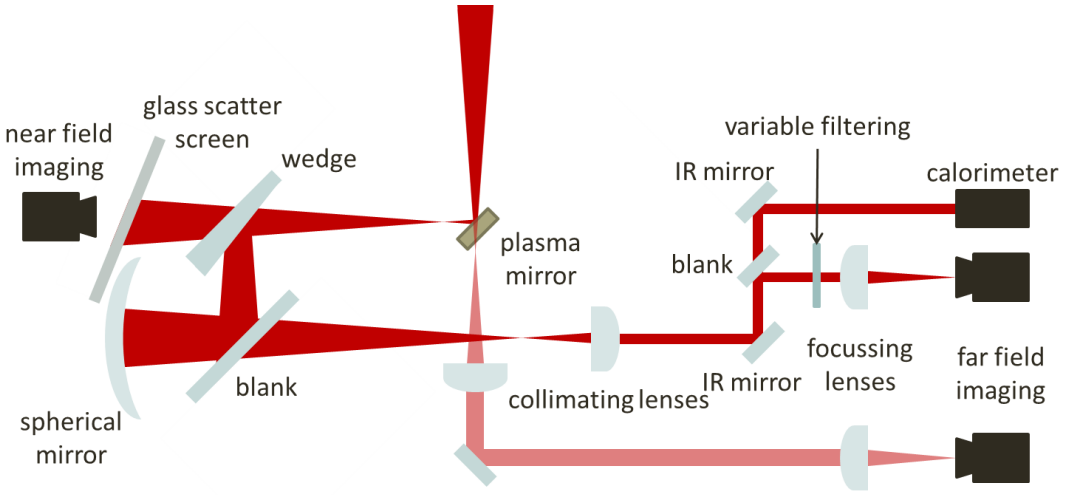

Figure 4.1: Schematic of experimental setup detailing the positions of blanks and wedges used for energy mitigation and focussing optics. For simplicity the variable filtering is omitted.

to three orders of magnitude, calibrated for the laser wavelength, was installed on this line. By making energy measurements using the same calorimeter at a position on the beam line prior to the plasma mirror, the throughput of the system was calibrated for comparison to in house on shot total energy delivery calorimetry.

In addition to the on shot set up, an equivalent plane monitor was used to directly image the far field when the plasma mirror was driven out of position by a motorised translation stage. This allowed the focus of the parabola to be optimised as well as acting as a far field reference against the relatively more complex post plasma mirror imaging line. As this drive allowed positioning accuracy to within $\frac{1}{16}$ μm, the driving action did not affect the beam alignment.

To enable testing to be carried out at two minute repetition rate, the plasma mirror was positioned a distance from focus where a maximum intensity of around 10^{15} Wcm^{-2} could be reached using only 1 J deliverable by the front end of the laser system. To achieve this, the plasma mirror was positioned 2.5 mm from focus, giving a spot diameter of $200\times200\sqrt{2}$ μm on the plasma mirror surface. As this is some twelve times the Rayleigh length, the beam can be considered to be outside the far field.

In designing the experimental setup, special attention was given to minimising the accumulated B-integral of the far field imaging system. For a laser of wavelength 1.054 μm, a B-integral of unity is accumulated on propagating through each centimetre of BK7 glass at an intensity of 5.3 $\times 10^{10}$ Wcm^{-2} [98]. Typically, the work here concerns maximum post plasma mirror energies of $\sim$450 mJ, for which the maximum accumulated B-integral on the imaging line approaches only 0.1. As the results of this chapter are obtained primarily for energies in the region of half this value, B-integral effects within the diagnostic are negligible.

Suitable collection of the specularly reflected light is also important, and to ensure that this was achieved the spherical mirror used subtended an $f/5.3$ collection angle, more than double the nominal $f/\#$ of the specularly reflected light from the plasma mirror. This ensured that the whole beam and some small angle scattering would be collected when the plasma mirror was operating in the region of interest, and that any hard edges of the specular intensity distribution would be avoided when collecting the beam, which could be detrimental to the far field measurement. Some consideration of the collection efficiency of the system is given in Appendix A.

4.3 Experimental results

4.3.1 Specular reflectivity intensity dependence

As the plasma mirror was being operated closer to focus than usual it was important to obtain the characteristic calibration curve of the intensity dependent specularly reflected energy fraction, in the single pulse regime, to ensure it was working as expected. The specular reflectivity of the plasma mirror operating 2.5 mm from focus is presented in figure 4.2 alongside data obtained on the same campaign where the plasma mirror was positioned 1.5 cm from focus, and the data is found to be in good agreement. On shot far field measurements were simultaneously recorded, shown in figure 4.3, providing a benchmark for the far field quality of the double pulse system.

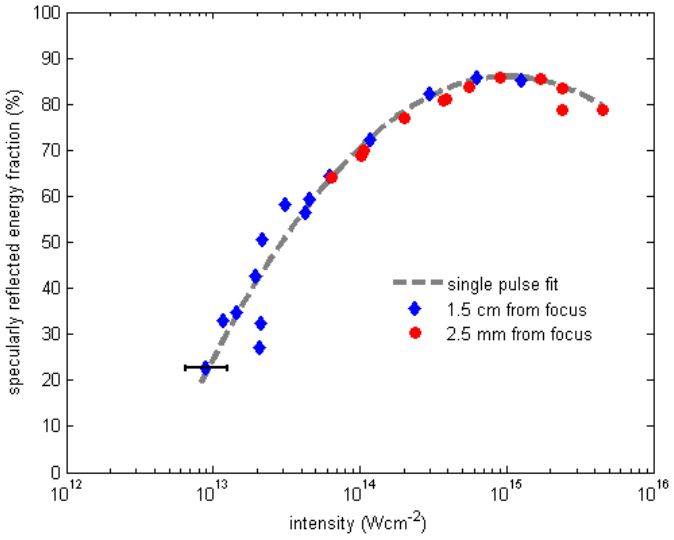

Figure 4.2: The plasma mirror reflectivity curves for single pulses obtained at two operating distances from focus. A representative error bar for the intensity is given which is derived from the intensity distribution given in figure 4.9.

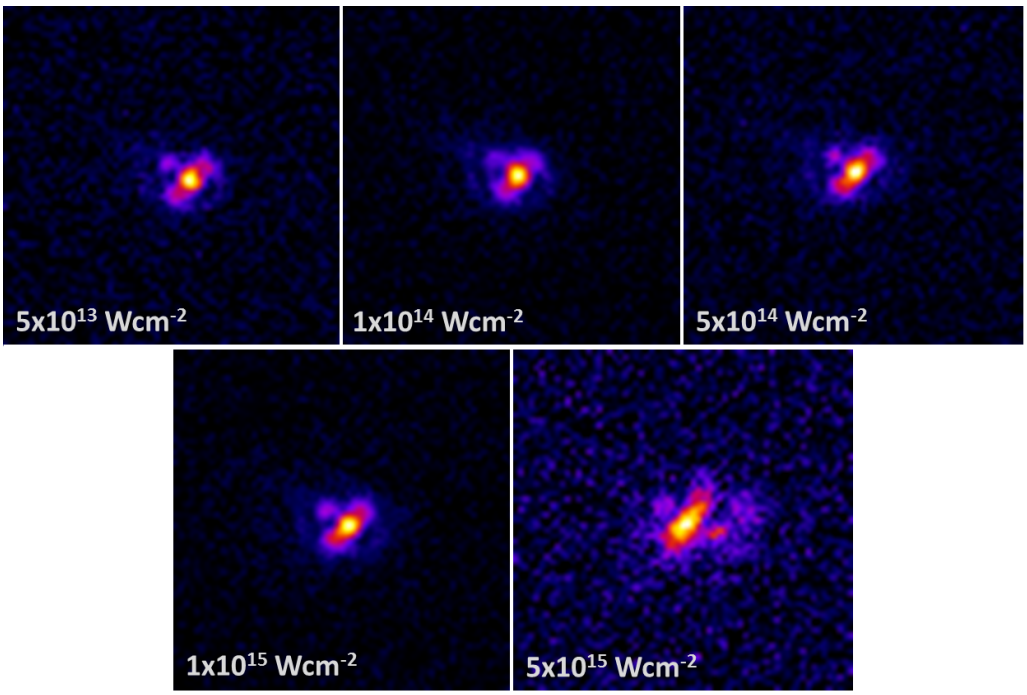

Figure 4.3: The post plasma mirror far field intensity distributions for a series of single pulse shots at varying incident intensities.

A typical reflectivity curve is obtained for the single pulse interaction, where the specular reflected energy fraction increases with rising peak intensity, which corresponds to the rising edge of the main pulse ionising the plasma mirror. A peak reflected energy fraction of 85 % is observed at an intensity of 10^{15} Wcm^{-2}, above which the the peak reflectivity of the mirror begins to drop. This due to the plasma mirror surface becoming ionised earlier in time with respect to the main pulse arrival. With the contrast ratio at a few picosecond reaching as much as 10^{-3} of the main pulse intensity, some plasma expansion can be driven resulting in a reduced specularly reflected energy fraction due to the main pulse being scattered or absorbed in the preplasma.

A qualitative analysis of the simultaneous far field measurements show that for the single pulse type interaction, the far field quality is semi independent of the incident intensity; up to around 10^{15} Wcm^{-2}, where the far field quality is maintained by keeping the picosecond contrast ratio below the damage threshold of the plasma mirror. As the intensity increases beyond this point, surface nonuniformities have sufficient time to grow to alter the post plasma mirror far field quality.

4.3.2 Specular reflectivity time dependence

The temporal behaviour of the plasma mirror was investigated with an ionisation:probe pulse intensity ratio set at 1:8, verified through calorimetry, for time delays in the range of 1 ps to 40 ps.

Both the reflected energy fraction and far field intensity distribution of the probe pulse show strong dependency on the temporal separation of the pulses. These dependencies can be understood in terms of the plasma conditions dictated by the ionisation pulse, primarily through the nature of the ionisation caused and the plasma temperature seeded by the ionisation pulse. Within this section the temporal dependence of the reflected energy fraction and far field intensity distribution of the probe pulse are introduced in turn, and the trends are described in the context of the plasma conditions set up by the ionisation pulse.

4.3.2.1 Reflected energy fraction

As the plasma mirror has been shown to be independent of both the intensity as varied by energy (section 4.3.1) and the intensity as varied by spot size [83], when the total incident energy fraction of the ionisation pulse, f_{ion}, is known, the specularly reflected energy fraction of the ionisation pulse, R_{ion}, can be calculated from the single pulse reflectivity curve in section 4.3.1. This allows the single time integrated calorimetry measurement of the total specularly reflected energy, E_{cal}, to be deconvolved into its component ionisation and probe pulse contributions, when the total incident energy, E_{inc} is known. From this, the experimentally measured specularly reflected energy fraction of the probe pulse alone, R_{probe}, is calculated from equation 4.1, for a range of ionisation-probe pulse time delays and intensities, and this is shown in figure 4.4.

$$R_{probe} = \frac{E_{cal} - (R_{ion} f_{ion} E_{inc})}{E_{inc} - (f_{ion} E_{inc})} \tag{4.1}$$

Two trends stand out, firstly, the reflected energy fraction of the probe pulse has a different intensity dependence when compared to that for a single pulse; secondly there is a strong dependence of the reflected energy fraction on the ionisation-probe time delay.

Figure 4.4 shows clearly that for time delays of up to 5 ps the specularly reflected energy fraction is enhanced considerably, from which a maximum probe pulse specularly reflected energy fraction of 96 % was measured, well in excess of the 84 % expected for a similar single pulse interaction.

Relative to the single pulse case, the increased specularly reflected energy fraction with intensity is likely due to spatial variations of the ionisation pulse intensity on the plasma mirror surface. As the intensity of the ionisation pulse increases, the lower intensity regions form critical density plasma, where there was none at lower intensity. If the probe pulse encounters preformed plasma, no energy is needed to form the plasma at short time delay and this leads to an enhancement in the reflected energy fraction. Because of this, an initial rise

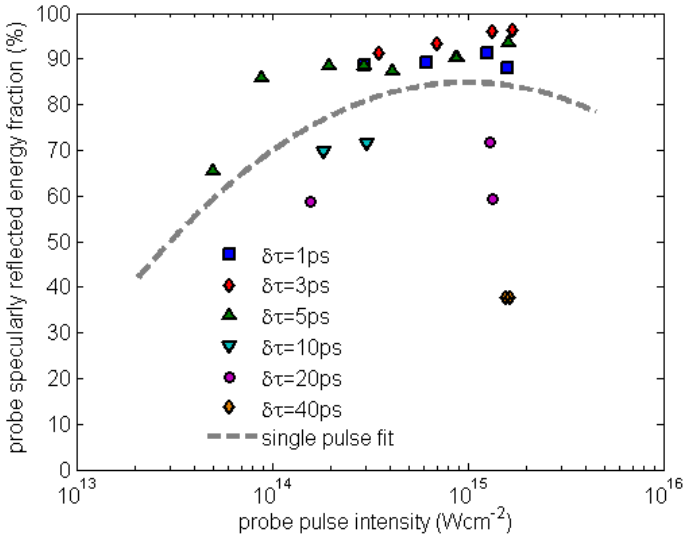

Figure 4.4: The intensity dependent plasma mirror specular reflectivity curves for the probe pulse alone, measured at various time delays relative to the ionisation pulse. The ionisation to probe pulse intensity ratio is 1:8.

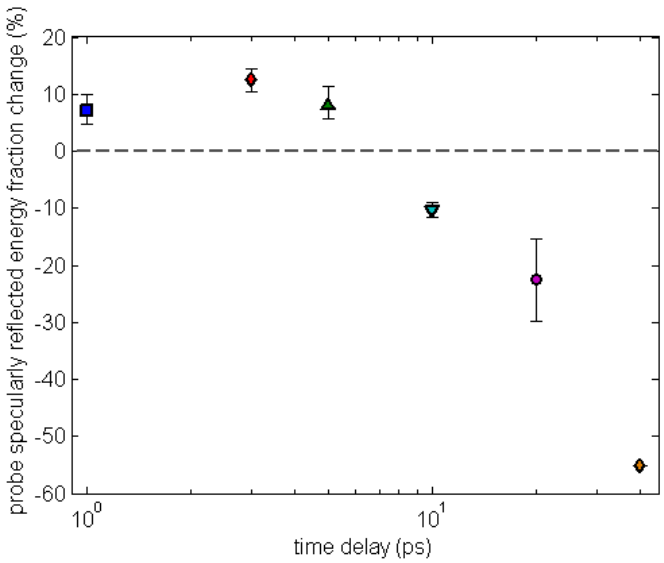

Figure 4.5: The time dependence of the reflected energy fraction change of the probe pulse relative to the single pulse. Error bars represent the range of the experimental measurement.

in the probe pulse reflectivity for short time is expected as the ionisation pulse creates an ionised surface that the probe pulse goes on to interact with.

A result that marks the onset of an enhanced reflectivity due to preformed plasma is the marked reflectivity enhancement in the 10^{14} Wcm^{-2} probe pulse intensity region of the 5 ps delay scan, where the reflected energy fraction is well in excess of that expected for a single pulse. The observation that the reflectivity of the double pulse configuration drops close to that of the single pulse as the probe pulse intensity is reduced to $\sim 5 \times 10^{13}$ Wcm^{-2}, is consistent with the $\sim 6 \times 10^{12}$ Wcm^{-2} ionisation pulse approaching the threshold minimum intensity to ionise the plasma mirror. Around ten percent of the ionisation pulse is expected to be specularly reflected at this level, which might be explained by only the hottest spot of the plasma mirror becoming over critical density, resulting in only a small region of preformed plasma reflecting a small fraction of the probe pulse. This is consistent with spatial variations in the ionisation of the plasma mirror surface.

An estimate of the average enhancement in the specularly reflected energy fraction with time, relative to the reflected energy fraction expected for a single pulse, is given in figure 4.5. To mitigate the intensity dependence, each enhancement is averaged for measurements made in the intensity range of 2×10^{14} - 2×10^{15} Wcm^{-2}, and error bars indicate the range in the enhancement.

The observation of the peak specular reflected energy at a temporal delay of 3 ps is intriguing. As the laser energy source has effectively been switched off 3 ps prior to the arrival of the probe pulse, additional reflected energy must arise from some inherent property of the plasma itself. A possibility is that lower laser intensity regions on the periphery of the ionisation pulse spot only partially ionise the plasma, leaving it under critical and not reflecting. Collisional avalanche ionisation taking place in these regions could lead to them becoming over critical only after there has been time for a sufficient number of collisions to make this region over critical. The 3 ps time scale that is observed to maximise the reflectivity of the plasma mirror surface is in some agreement with that experimentally

observed by *Pronko et al.* [99].

The fact that the maximum, minimum and average specularly reflected energy measurements in this range all show this trend indicate that this is a real effect, and with the estimated error in the shot to shot reproducibility of the method being less than 1 % from nominally similar shots, and system light collection efficiency appear to vindicate this.

As observed for delays of 10 ps and over, the specularly reflected energy fraction of the plasma mirror is expected to fall. This is because as the plasma scale length get longer with time, they become more absorbing. An estimate of the time delay dependent absorption fraction is made in section 4.4.

4.3.2.2 Post plasma mirror far field

The on shot far field intensity distributions simultaneously recorded with the calorimetry measurements in section 4.3.2.1 are shown in figure 4.6. Each image corresponds to the maximum incident intensity for the stated time delay, with the exception of the 10 ps delay, for which the maximum intensity data shot is about four times lower than the others. However, the far field intensity distribution is again found to be semi-independent of the incident plasma mirror intensity, for 5 ps time delay shots in the range of $9{\times}10^{13} - 2 \times 10^{15}$ Wcm^{-2}, so it is assumed that the lower intensity 10 ps delay shot, while at a different intensity, is representative of the data set as a whole.

There is a clear general deterioration in the far field quality with the plasma mirror ionisation time, and a radial integration technique was used to characterise the extent of the far field deterioration. The radial integrals in figure 4.7 confirm that as the probe pulse is delivered at later time the energy is scattered to a greater degree, and as a guide for the energy that is contained in the focal spot the half energy spot width is used, shown on figure 4.7.

For time delays of up to 3 ps the far field spot size remains of a quality that the measurements are still to within error, but as time delays increase beyond 10 ps the spot sizes indicate that orders of magnitude intensity reduction results.

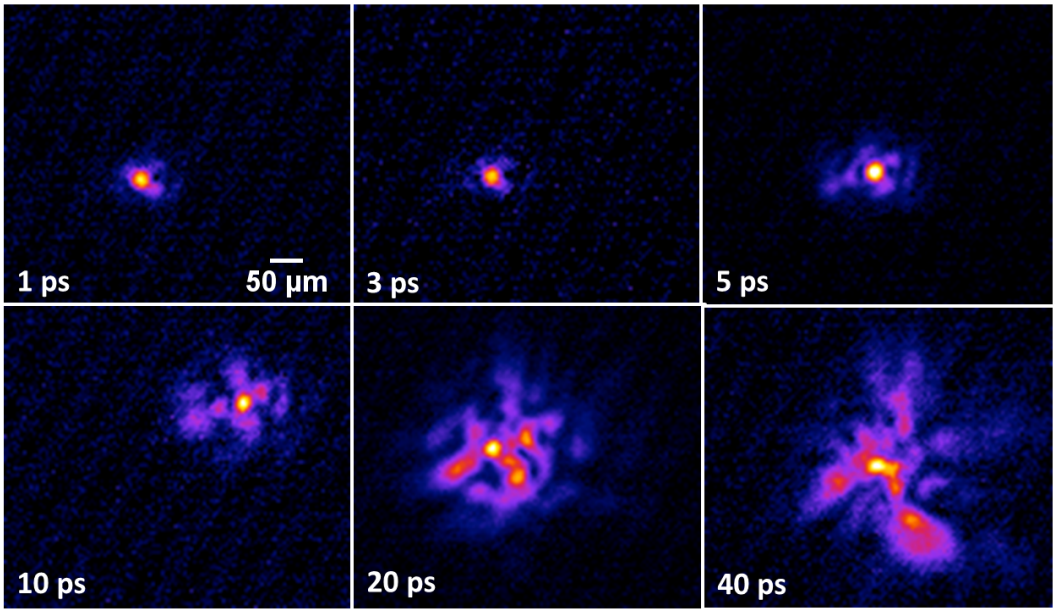

Figure 4.6: The on shot far field intensity distribution obtained on the ionisation-probe shot configuration, for various time delays, the corresponding reflectivities of which are given in figure 4.4. Spatial scales are the same for each image, with the intensity scale normalised to the maximum pixel value of each image.

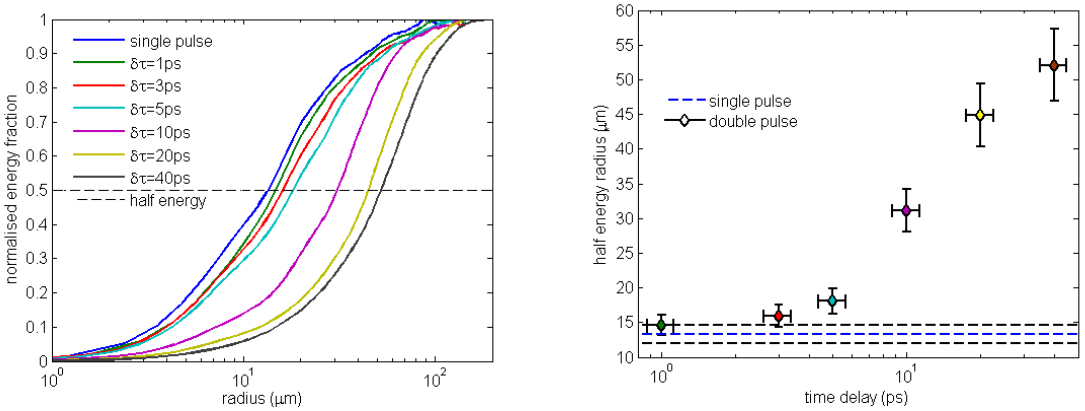

Figure 4.7: (left) The radial integrals of the far field intensity distributions in figure 4.6, with a dashed line marking the radii at which half the energy content is within the beam. (right) The radius of the beam containing half the total far field energy content as a function of plasma mirror ionisation time. The blue dashed line refers to the radius for a single pulse, with the black dashed lines being the error bar associated with that measurement.

4.4 Plasma mirror dynamics in the quasi near field

The extent to which the wavefront is distorted is principally determined by the introduction of phase shifts by non uniform critical surface expansion in the quasi-near field of the beam. A simple model of this can be derived from figure 4.8, which shows two rays incident on a surface with a height perturbation δx. It is simple to show that the relative phase shift introduced to the reflected rays, by virtue of their path difference is given by equation 4.2.

$$\delta\varphi = \frac{2\pi}{\lambda} 2\delta x \cos\theta_i \tag{4.2}$$

If the phase shift is zero then the surface can be considered to be perfectly smooth, while a phase shift of π will cause complete destructive interference of the rays. This leads to a phase shift of $\pi/2$, being the arbitrary choice in perturbation height, $\mathscr{R}$, known as the Rayleigh criterion [100], which can be a useful definition for separating a rough surface from a smooth one, as in equation 4.3.

$$\mathscr{R} \equiv \delta x < \frac{\lambda}{8\cos\theta_i} \tag{4.3}$$

Although this appears crude, a rigorous statistical treatment of electromagnetic waves incident on a normally distributed surface by *Beckmann and Spizzichino* [101] yields a similar factor in describing the attenuation of the coherent specularly reflected intensity, $\mathscr{I}_{coh}$, in equation 4.4.

$$\mathscr{I}_{coh} = \mathscr{I}_0 \exp\left[-\left(\frac{2\pi}{\lambda} 2\sigma_x \cos\theta_i\right)^2\right] \tag{4.4}$$

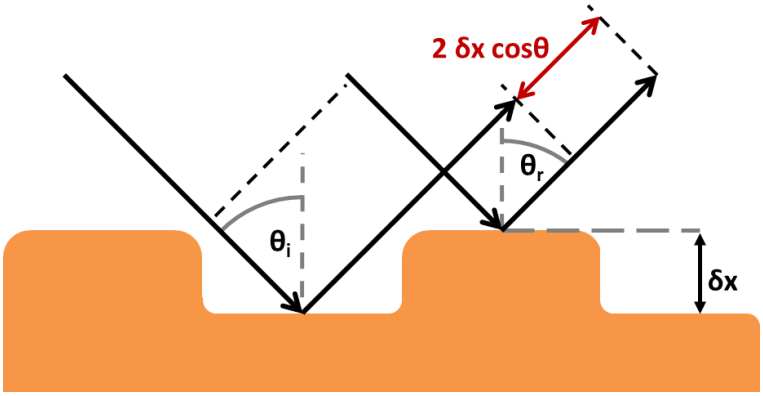

Figure 4.8: A schematic to aid the discussion of the Rayleigh criterion in the text. Two incoming rays at an angle of incidence θ_i are specularly reflected from an uneven surface with a perturbation height δx. This causes the reflected rays to have a different total path length, causing a relative phase shift.

Here the surface is characterised by a standard deviation of the perturbation height, σ_x, which is assumed to vary slowly compared to the wavelength of the incident radiation. This includes statistical averaging such that $2\sigma_x = \delta x$, and the Rayleigh criterion expressed in terms of σ_x becomes, $2\mathscr{R}_\sigma = \mathscr{R}$ [102]. In terms of the full width at half maximum, $\mathscr{R}_{\text{FWHM}} = 2\mathscr{R}_\sigma\sqrt{2\ln(2)}$.

This eliminates the need for an arbitrary choice of phase shift to separate smooth and rough surfaces by allowing the coherent reflected intensity to be calculated. When the Rayleigh criterion is satisfied, $\mathscr{I}_{coh} \approx 0.54\mathscr{I}_0$.

The beam intensity distribution 2.5 mm from best focus, where the plasma mirror was operated, is shown in figure 4.9. This shows a deviation from the ideal super Gaussian near field distribution, with intensity variations that will lead to variations in critical surface position. To obtain an intensity map, the average energy in the nominal 200 μm spot was used to normalise each pixel, from which individual pixels can be assigned an intensity. The intensity distribution of a nominally 10^{14} Wcm^{-2} spot, which corresponds to a typical ionisation pulse intensity, is also shown in figure 4.9.

An electron temperature is assigned to each point on the intensity map by interpolating a temperature based on inverse Bremsstrahlung scaling by *Pert* [103]. With the skin depth of the laser estimated to be of the same scale as the surface

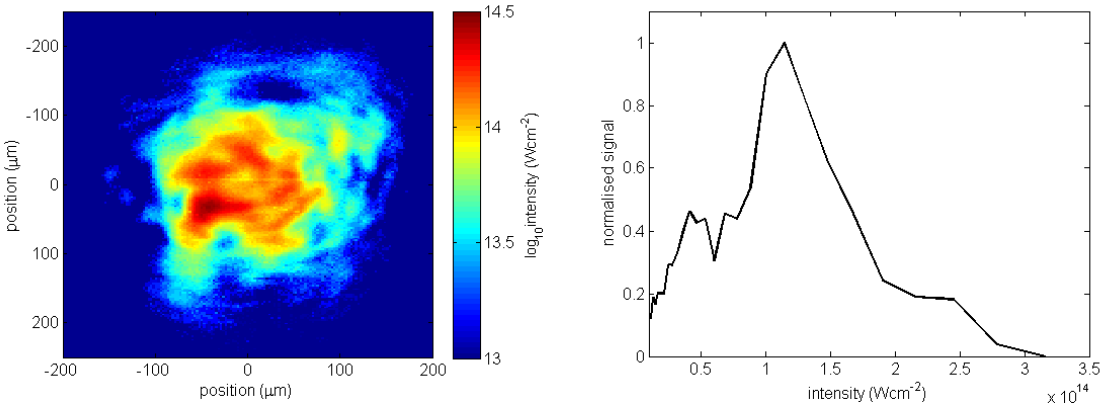

Figure 4.9: (left) The spatial intensity distribution of the quasi near field incident on the plasma mirror as viewed from a 0° degree angle of incidence on the detector. (right) The intensity distribution in the quasi near field.

contaminant layer thickness on the plasma mirror, which itself is estimated to be several [104] to tens of nanometres deep, it is assumed that the bulk of the laser energy is deposited here. It is also assumed that the position of the critical surface will be dominated by the high charge to mass ratio and quasi-neutral hydrogen expansion from this layer. A contaminant layer with a unperturbed hydrogen number density of 10^{28} m^{-3} is assumed, which is consistent with that of water and medium chain hydrocarbons likely to be found in the chamber vacuum pumps. A simple self similar hydrodynamic expansion is assumed where the plasma travels normal to the initial surface and the electron density profile takes the form of equation 2.29.

This indicates the critical surface to be moving with an average speed of around 260 nm ps^{-1}. Crucially, the critical surface can move many times that dictated by the Rayleigh criterion, but it is the temperature differences seeded by the laser that results in expansion velocity differences which themselves cause the critical surface to become more greatly perturbed with increasing time.

As the most intense regions of the interaction seed a faster expansion, the expansion is convolved with the laser intensity to weight the importance of each point's contribution to the far field. The position of the critical surface with respect to the original plasma mirror position is shown for a expansion time of 1 ps in figure 4.10. The full width at half maximum of this distribution can

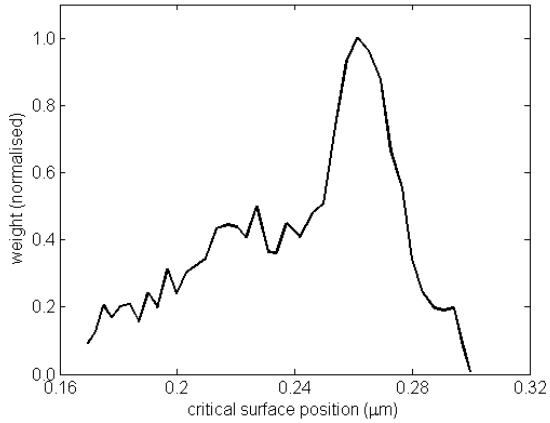

Figure 4.10: The position of the critical surface relative to its position at t_0 after a self similar expansion for a duration of 1 ps. Each position is weighted by the incident laser intensity at that point to correlate the position with its influence on the final far field intensity distribution.

Time (ps)	**FWHM** $/\mathscr{R}_{\text{FWHM}}$	$\mathscr{I}_{coh}$ $(\mathscr{R}_{\text{FWHM}})$ $/\ \mathscr{I}_0$	$\mathbf{1/e}_N$ $/2\mathscr{R}$	$\mathscr{I}_{coh}$ $(2\mathscr{R})$ $/\mathscr{I}_0$
1	0.13	0.98	0.37	0.91
3	0.39	0.91	1.11	0.46
5	0.65	0.77	1.85	0.12
10	1.30	0.35	3.69	0.00

Table 4.1: The critical surface non uniformities at different expansion times, and the intensity correlated expansion (figure 4.10) expressed as a fraction of the Rayleigh criterion introduced in the text.

Time (ps)	$\overline{L}_{\text{FWHM}}$ (μm)	$(\overline{\nabla n_{crit}})_{\text{FWHM}}$	$\theta_{i\,eff}$	$f_{abs\,res}$ (%)	$f_{abs\,ib}$ (%)
1	0.057	1.42E-3	0.08	0.1	1.4
3	0.171	4.26E-3	0.24	0.4	4.2
5	0.285	7.11E-3	0.41	0.6	6.9
10	0.570	1.42E-2	0.81	1.1	13.4

Table 4.2: An estimate of the scale lengths, $\overline{L}_{\text{FWHM}}$, and critical surface density gradients, $(\overline{\nabla n_{crit}})_{\text{FWHM}}$, from the self similar plasma expansion which are used to estimate the absorption fractions of the laser energy by resonant absorption, $f_{abs\,res}$, and the inverse Bremsstrahlung mechanisms, $f_{abs\,ib}$.

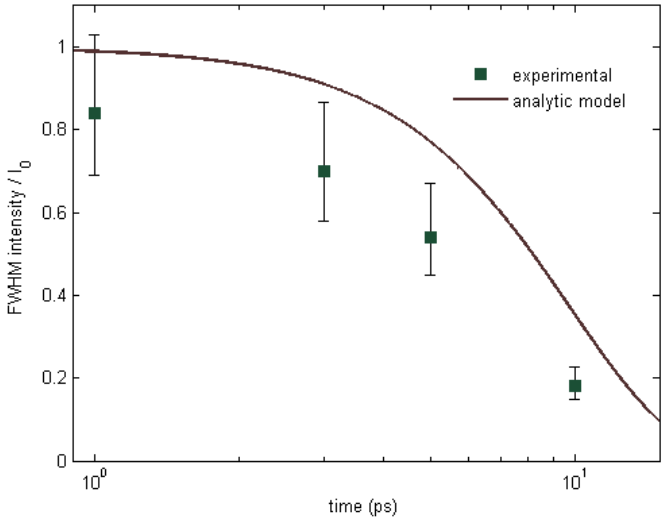

Figure 4.11: A comparison of the analytical model coherent specular reflected intensity fraction and the experimentally measured scaled intensity.

be expressed as a fraction of the Rayleigh criterion, and the coherent specular reflected intensity fraction obtained from equation 4.4.

The trend of the coherent specular reflected intensity fraction of the analytic model, for full width at half maximum, in figure 4.11 is qualitatively similar to the experimentally measured trend, although the analytic model predicts a higher intensity fraction than that experimentally measured. This discrepancy may be explained by a constant expansion velocity over time being assumed by the analytic model. In reality the plasma expansion will decelerate over time, and a faster initial expansion would go some way to explaining why in experiment a sharper initial deterioration in the beam quality is observed.

The analytical model also assumes the characteristic critical surface perturbation size to be normally distributed, and this can only be approximated by relating some aspect of the critical surface position distribution in figure 4.10 to that of a normal distribution, and for this reason the full width at half maximum is chosen. If the $1/e_N$ criteria is used instead, the model under predicts the coherent specularly reflected energy fraction, and does not accurately reflect the trend observed, as the $1/e_N$ measurement of the critical surface position distribution severely deviates from a Gaussian fit. This is shown for reference in table 4.1. It

is conceivable that some of the error in the analytic trend be due to this critical surface distribution.

The self similar expansion model can also be used to estimate the preplasma conditions that the probe pulse encounters, where density scale lengths and critical surface gradients are of most importance for absorption. These values corrected for the laser incident angle for the full width at half maximum intensity profile of the pulse are given in table 4.2.

Since the laser pulse is s-polarised with respect to the plasma mirror surface, resonant absorption can only take place in the density gradients set up by the ionisation pulse. These gradients can be used to estimate an effective angle of incidence for resonant absorption, and an estimate of the resonant absorption and inverse Bremsstrahlung absorption fractions [105] are given in table 4.2.

The interaction of the probe pulse with the plasma conditions set up by the ionisation pulse is two fold. On one hand if there is no plasma, the probe pulse reflectivity is reduced, but on the other if plasma exists with a long enough scale length, it will begin to absorb the probe pulse energy. By considering the average scale lengths and critical surface density gradients estimated by the self similar expansion model, an estimate of the fractional absorption by the resonant and inverse Bremsstrahlung absorption mechanisms were calculated by the model given by *Wilks and Kruer* [33], and are given in table 4.2. Because the transverse critical surface gradients are always small, resonant absorption only plays a limited role for the time delays considered, while inverse Bremsstrahlung is estimated to become large for long time delays. There is some agreement here between the model and experiment, particularly in the preplasma conditions estimated for the 3 ps time delay, when avalanche ionisation has potentially had time to act across the whole of the irradiated plasma mirror region. Here, barring absorption, 100 % reflectivity would be expected, but the estimated 4.6 % absorption is in good agreement with the peak 96 % specularly reflected energy fraction measured (figure 4.4). However, it would appear that the model under predicts the absorption fraction for a 10 ps delay type scale length.

4.5 An analysis of the specularly reflected energy fraction

To the knowledge of the author, the experimental results in section 4.3.2.1 report the highest reflected energy fraction from a plasma mirror interaction in the literature. Not only this, but the inherently large value of the peak measured reflectivity requires some fundamental consideration as to whether this integrated measurement can be physically correct. Here, this is done by assuming an intensity dependent reflectivity behaviour of the plasma mirror, based on the single pulse experimental results, and taking consideration of the real incident intensity profile on the plasma mirror surface introduced in figure 4.9. From this, a modelled response of the the integrated plasma mirror reflectivity is given. An estimate of the integrated reflectivity of the probe pulse from the plasma mirror in double pulse operation is then made, using the same method and assuming a different intensity dependent reflectivity behaviour, based on the 96 % peak reflectivity measurement.

For a single pulse type interaction, the natural choice of intensity dependent reflected energy fraction comes from assuming that the integrated reflected energy fraction measured for a single pulse in figure 4.2 is representative of the average intensity at which it was measured. The specific reflectivity at each intensity was convolved with the intensity distribution in the plasma mirror quasi near field of figure 4.9, and from this the modelled integrated reflectivity shown in figure 4.12 was calculated across a range of average near field intensities.

Qualitatively, the curve shows a similar intensity dependence, with the reflected energy fraction, peaking at around the same maximum as that measured and has a similar low energy cut off to experiment. Across the bulk of the intensity range, the modelled response does however predict a reflected energy fraction, roughly 10 % lower than that observed. This is probably due to the assumption that the single pulse reflected energy fraction is representative of that of the averaged intensity at which it was measured. This experimental measurement itself

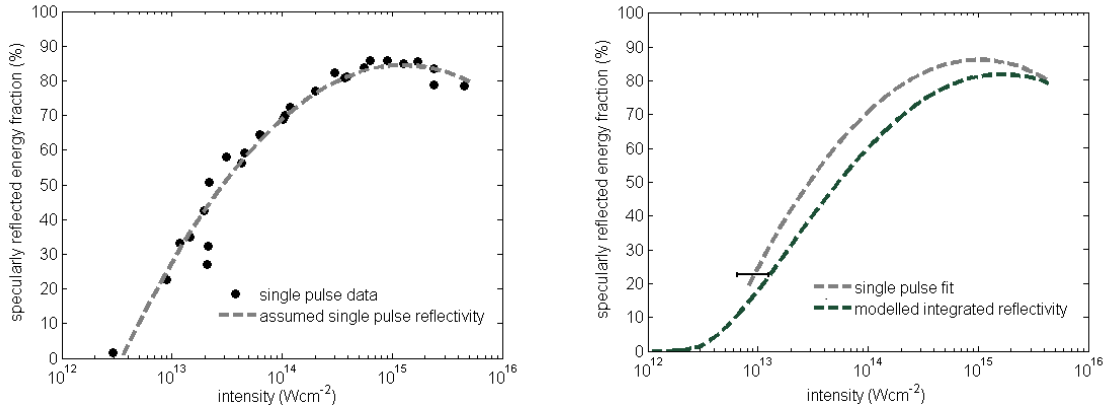

Figure 4.12: (left) The assumed intensity dependent reflected energy fraction (dashed line), shown in comparison with the experimental data for a single pulse integrated reflectivity measurement. (right) The fit to the single pulse experimental data introduced in section 4.3.1 (grey dashed line), compared with modelled integrated reflectivity from considering the assumed intensity dependent reflected energy fraction (left) and the incident intensity distribution on the plasma mirror surface (green dashed line).

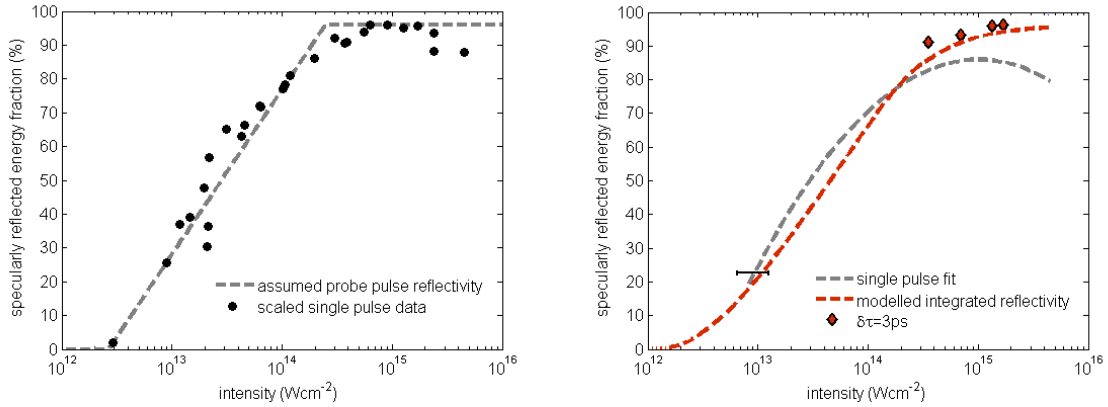

Figure 4.13: The assumed intensity dependent reflected energy fraction for the probe pulse (dashed line), shown in comparison to the experimental data for a single pulse integrated reflectivity measurement, scaled to a maximum reflectivity of 96 %. (right) The fit to the single pulse experimental data introduced in section 4.3.1 (grey dashed line), compared with modelled integrated reflectivity from considering the assumed intensity dependent reflected energy fraction (left) and the incident intensity distribution on the plasma mirror surface (red dashed line).

is time and space averaged, but to a first order, the intensity dependent reflected energy fraction is reproduced satisfactorily despite the near field intensity range spanning over two orders of magnitude. This gives a degree of confidence that the method employed can be used to reproduce the key features and intensity dependence of the reflected energy fraction.

For modelling the plasma mirror probe pulse integrated reflectivity, the assumed intensity dependent reflectivity in figure 4.13 was used. To arrive at this intensity dependent reflectivity, the experimentally measured maximum reflected energy fraction of 96 % is assumed to represent the maximum reflectivity at high incident intensity. The intensity range at for this large reflected energy fraction, was assumed to be in the range of $3.0\times10^{14}-1.7\times10^{15}$ Wcm^{-2}, where the plasma mirror is observed to have a quasi constant high reflectivity value of 84$\pm$2 % for single pulse interactions. It was also assumed that the probe pulse would require the same minimum intensity to ionise the plasma mirror as the single pulse, as the ionisation pulse intensity is too low to ionise the plasma mirror surface, and the experimentally measured value of 1.6 % at 3.0×10^{12} Wcm^{-2} is used. From these limits, the simplest intensity dependent reflectivity is assumed, as a first order estimate.

When using this assumed probe pulse intensity dependent reflectivity, the integrated reflectivity across the plasma mirror near field intensity distribution was again calculated, and is shown in figure 4.13. When a maximum reflectivity of 96 % is assumed, there is very good agreement between the modelled trend and the reflected energy fraction measured for a 3 ps ionisation-probe pulse time delay, indicating that the plasma mirror is achieving these high reflectivity values.

Toward lower intensities, the modelled response once again under predicts the reflected energy fraction, which is likely to be due to the same reasons as previously outlined. However, in addition to this, time dependent ionisation induced by the ionisation pulse is not taken into account, which would have the effect of increasing the reflected energy fraction at lower intensity. This could be taken into account by reducing the gradient of the fit in the $< 96\%$ reflectivity region

of the assumed reflectivity curve, but with a lack of experimental data on this, any factor introduced for this purpose would be artificial. This does not diminish the observation that at high reflectivity regions around 10^{15} Wcm^{-2}, where this under estimate is likely to be less important, the peak observed reflected energy fractions are reproduced well.

4.6 Conclusions and discussion

For the first time the optical quality of the post plasma mirror far field has been characterised as a function of plasma mirror ionisation time, by the use of a double pulse in the ionisation-probe fashion described. The unique combination of calorimetry measurement with optical diagnostics to monitor the post plasma mirror focal spot quality also present the first such calibration across the whole intensity curve.

Not only have the plasma mirrors been shown to remain of high optical quality for time scales of up to 5 ps, but the specularly reflected energy fraction of up to 96 %, observed for the probe pulse is the highest reported to date, which with further investigation may provide a new means of mitigating energy loss by plasma mirrors. This is especially problematic in systems with multiple plasma mirrors for extra contrast enhancement, where energy loss rapidly becomes troublesome. New focussing geometries could be implemented to avoid the ionisation pulse travelling on to target, or the geometry kept in experiments where some degree of controlled preplasma is advantageous. The reflectivity enhancement and its apparent peak at 3 ps is attributed to the specific ionisation mechanisms at work, and variations in the beam quasi near field distribution.

To explain the experimental results, an analytical model based on a simple self similar expansion was developed, with the experimentally measured intensity profile on the plasma mirror surface an integral part. This intensity profile is shown to be crucial, as the non uniformities in plasma expansion are inextricably linked with the real intensity distribution. The non uniformities in plasma expan-

sion provide an insight into the evolution of the critical surface position, which is used as a basis for the second part of the analytic model which relates the critical surface distribution to the coherent specularly reflected energy fraction. With limited experimental data, the model simplicity is appealing as it gives an estimate of the final far field quality based on only one free parameter, the surface roughness, while the other variables, wavelength and angle of incidence are well known.

The model gives a trend in the coherent specular reflected intensity fraction of the analytic model in figure 4.11 that is qualitatively in agreement with the experimentally measured trend, although some discrepancy exists that is outwith the experimental error. This may be attributed to some of the simplifying assumptions made by the model, such as the constant plasma expansion velocity or the normal distribution that the analytical model assumes the critical surface to take. The model also gives some agreement with the trend in experimentally measured absorption, indicating that the scale lengths and thus expansion have been dealt with satisfactorily.

The model was also only extended to times of 10 ps as time scales much greater than this appear to be when radiative cooling as estimated by blackbody emission begin to become important.

To experimentally measure the sub micron structure which is primarily responsible for the deterioration of plasma mirror optical quality would be challenging. Common techniques such as shadowgraphy have micron resolution at best, limited by the laser wavelength. To probe scales of this size a secondary laser would be needed at a wavelength much shorter than the operating wavelength of interest, and interferometry by the shorter wavelength may reveal small scale structure in the density profile at the plasma mirror operating wavelength critical surface. This laser must also be pulsed with a similar duration, where shorter pulses would give better temporal resolution.

Chapter 5

Multi-pulse enhanced laser ion acceleration using plasma half cavity targets

In this chapter, experimental results and numerical modelling of a plasma half cavity target design for laser driven ion acceleration is presented. This new geometry enhances the laser to proton energy conversion efficiency and has been found to modify the low energy region of the proton spectrum. The target design utilises the high fraction of laser energy reflected from an ionised surface and refocusses it such that a double pulse interaction is attained. Numerical modelling through particle in cell simulations and experimental results demonstrate that laser to proton energy conversion efficiency is doubled, compared to planar foil interactions, when the cavity returns the post pulse within picoseconds of the primary interaction.

This work has in part been published in *Applied Physics Letters* [91].

5.1 Introduction

The concept of using an energetic ion beam to drive fusion of a deuterium-tritium fuel capsule is first discussed in the literature in the context of using the then current technology of linearly accelerating ion beams for the compression and ignition of the capsule [106]. Here, the challenge of creating high current, short bunch beams whilst preserving the beam emittance by enhancing the accelerator technology of the time is discussed. Even in the present day, many of these ion beam constraints for fusion reactions remain out of reach of conventional accelerators, whilst the emerging field of laser driven ion acceleration takes many of these desired beam properties for granted. However, the laser driven method of ion acceleration is not without its own challenges.

The quasi thermal TNSA proton spectrum has been the subject of much theoretical study as an igniter beam in the fast ignition scheme of inertial confinement fusion [10, 107, 108] and this work indicates that a proton igniter beam could be feasible with ignition predicted to be possible with currently achievable proton temperatures in the MeV range. However, the total proton energy that need be delivered to the compressed target has been estimated to be in the region of 20-40 kJ [10, 108]. This indicates that to be feasible on the proposed megajoule facilities of the future, the conversion efficiency of laser to proton energy must be increased beyond the few percent routinely reported in the literature to around 10-20 %.

In many laser plasma interactions, large fractions upward of 60 % of the total incident laser energy has been measured to be reflected from the target [39]; a fraction found to be almost intensity independent over four orders of magnitude up to 10^{21} Wcm^{-2} in ultra high contrast interactions [109]. A target design is introduced in figure 5.1 which is engineered to reuse the reflected laser energy to increase conversion efficiency of the laser to proton energy. In this scheme, in addition to the planar (accelerating) foil that the laser primarily interacts with, a second (cavity) foil forms a half cavity which collects the reflected laser light

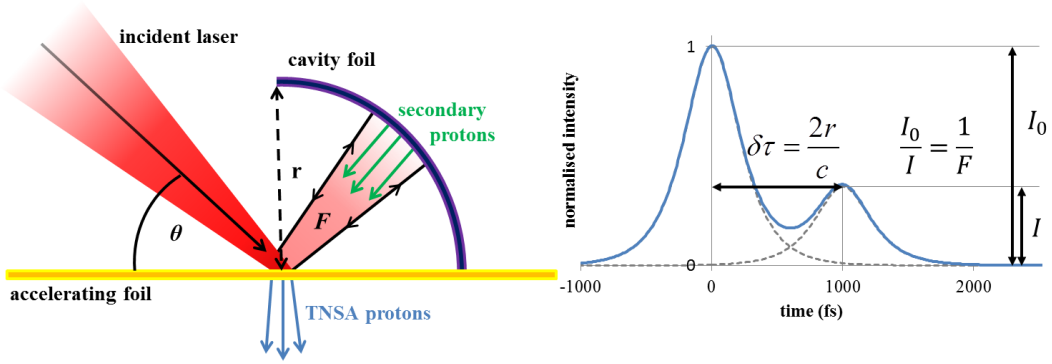

Figure 5.1: (left) Schematic showing the incoming main pulse being reflected by a target foil. A plasma half cavity is used to back reflect and refocus the laser energy onto the target. (right) The intensity ratio of the pulses is determined by the combined reflected energy fraction, F, of the accelerating foil rear surface and cavity foil front surface. The delay between the pulses, $\delta\tau$, is set a $2r/c$ where r is the radius of the half cavity.

and returns it back to the initial interaction point. In addition to returning the laser light, by shaping the cavity foil as a quarter spherical mirror the light is also refocussed, maintaining a high beam intensity for the secondary interaction. This refocussing is crucial as the pulse may propagate several hundreds of microns for various time delays and therefore if the laser beam is considered to diverge obeying only Gaussian optics, the laser would be a fraction of the intensity when it arrives back at the initial interaction point, almost certainly destroying the potential for any double pulse interaction.

Non cavity focussing plasma optics have been examined before, for example the fast focussing elliptical plasma mirror developed by *Nakatsutsumi et al.* [110] which was demonstrated to operate well at intensities in the mid 10^{14} Wcm^{-2} range. Non focussing cavities are being explored by *Badziak et al.* in the regime of hydrodynamic acceleration of plasma [111, 112]. The concept of a focussing cavity design has since been independently applied to the radiation pressure acceleration mechanism by *Raçzka and Badziak* [113] since publication of this work.

The work presented in this chapter represents the first time that the concept of a focussing plasma cavity design has been discussed. This is also the only example of such an approach being applied to the target normal sheath acceleration mechanism, presently the most well understood of all ultrahigh intensity laser ion

acceleration mechanisms, and the data represents the first experimental results reported on such a concept.

The scheme reported here gives rise to a double pulse interaction with the accelerating foil, as in figure 5.1. The intensity ratio of the initial pulse to the post pulse is determined by the combined reflected energy fraction, F, from the surface of the accelerating foil and the interior surface of the cavity foil, while the delay between the pulses, $\delta\tau$, is simply determined by the time taken for the laser light to travel twice the radius, r, of the half cavity. By altering the half cavity radius, the timing of the delivery of the post pulse can be varied and chosen to optimise laser energy coupling to ions.

The multi pulse sheath acceleration mechanism first proposed by *Robinson, Neely, McKenna and Evans* [56] has since been subject to experimental investigation. First, by irradiating planar foils with a controlled prepulse followed by a 2×10^{19} Wcm^{-2} main pulse, an increased conversion efficiency of laser energy to protons by a factor of 3.3 was demonstrated [57], when using a prepulse containing 10 % of the total incident energy. Taking this work further using a similar experimental arrangement, a potential record laser to proton energy conversion efficiency of 15 % above 3 MeV, has since been observed [58].

In both cases the double pulse was delivered by using a Mach-Zender type system in the laser front end, similar to that described in section 3.2.2, to deliver a low energy prepulse followed by a high energy main pulse. The work discussed here differs in that the higher energy main pulse is followed by a lower energy post pulse by virtue of the target geometry. The novel work in this chapter aims to reuse the lost energy from the interaction and represents an investigation into the concept of how much extra energy can be converted to the accelerated ions through a double pulse interaction, without the need to alter the laser system or reduce the maximum on target energy. It is not intended to compete with the multi pulse sheath acceleration mechanisms, but shares the common goal of increasing energy conversion efficiency into ions and may complement it as part of a suite of techniques that can be applied for this purpose.

5.2 Experimental method

An experimental campaign was carried out using the PHELIX laser at the GSI facility, where the s-polarised laser is delivered in 500 fs pulses with typical on target energy of 105 J. The beam is focussed using an $f/9$ off axis parabola to a 20×15 μm FWHM elliptical spot at a 51° angle of incidence, giving on target intensities of 10^{19} Wcm^{-2}, and the pulse has a nanosecond contrast ratio of 10^{6}. The primary diagnostic for proton dosimetry was radiochromic film, which was used in a stack configuration to enable proton doses to be measured in discrete energy steps as well as providing the two dimensional spatial intensity distribution of the beam at selected energies. With shock velocities of several microns per nanosecond being induced by nanosecond prepulses [114], a 25 μm thick gold accelerating foil was selected to ensure that any shocks would not break out from the back of the target during the ion acceleration process.

The experimental geometry was designed to eliminate the possibility of any contribution to the RCF signal from secondary forward going ions, accelerated from reflected laser light incident on the cavity interior, as indicated on figure 5.1. As the Rayleigh length of the focussing optic is approximately 100 μm, the beam intensity on the cavity interior could conceivably remain as high as $10^{17} - 10^{18}$ Wcm^{-2}, and be theoretically sufficient to generate a secondary high energy TNSA proton beam at 51° to the forward direction.

Measurements of the spatial profile of the reflected laser light in Appendix A show a complex behaviour, where the beam expands from a far field containing 15 % of the energy in its FWHM to a near field $f/2.5$ beam containing 50 % of the energy, while the behaviour of the spatial distribution in intermediate fields is unknown. The focussing optic also delivers a spot which is a few times the diffraction limited waist size, and so the propagation between the near and far fields is likely to be complex. For simplicity, a geometric expansion is assumed with the energy in the FWHM being between 15-50 % as limiting cases for calculation of the intensity at the cavity interior. By applying the *Mora* model [46],

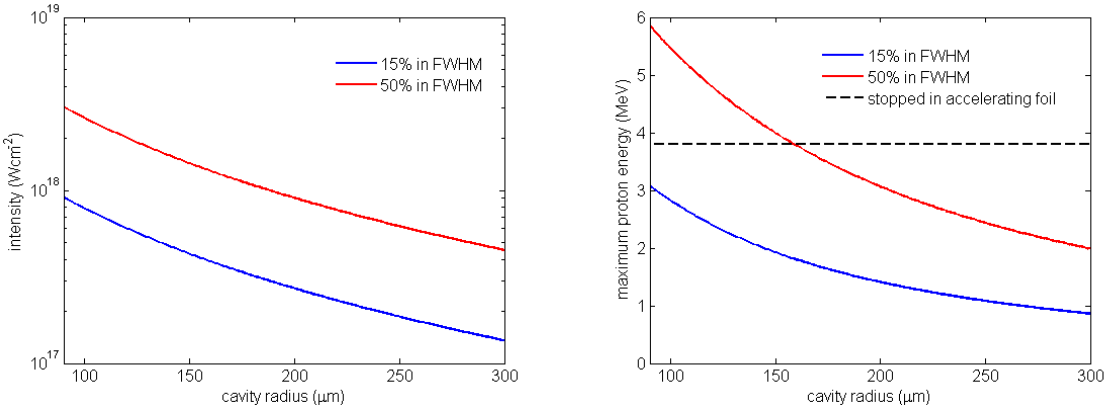

Figure 5.2: The upper and lower intensity limits on the cavity wall as a function of the cavity radius (left) and the corresponding maximum proton energies predicted by the *Mora* model (right).

a maximum proton energy from the cavity foil is approximated, and shown in figure 5.2. As indicated on figure 5.2, protons of energy below ~ 3.8 MeV are stopped in the accelerating foil, accounting for the $\frac{1}{\cos\theta_i}$ foil thickness correction, and any remaining protons that make it through the accelerating foil will be very low in number [48]. The combination of these effects make it unlikely that any secondary proton source will make a significant contribution to the measured dose. However, to further avoid the likelihood of detection of any secondary protons the RCF detector stack is positioned at a distance of 37 mm from the target such that any secondary beam would be well separated from the main beam in the detector plane.

A schematic of the experimental geometry is shown in figure 5.4 and this shows a wrap around image plate stack similar to that used by *Gray et al.* [40] that was employed to measure the electron distribution from the interactions and to investigate whether the cavity target geometry altered this distribution.

Reliable cavity target alignment required multiple imaging lines, as shown on the experimental setup figure 5.3. One imaging line was installed on the laser forward direction, comprised of a collimating and focussing achromatic lens, such that when the target was driven out of position the imaging line could be used to image the focal spot of the laser. The position where the laser comes to focus on this imaging line defines target chamber central. A second imaging line transverse

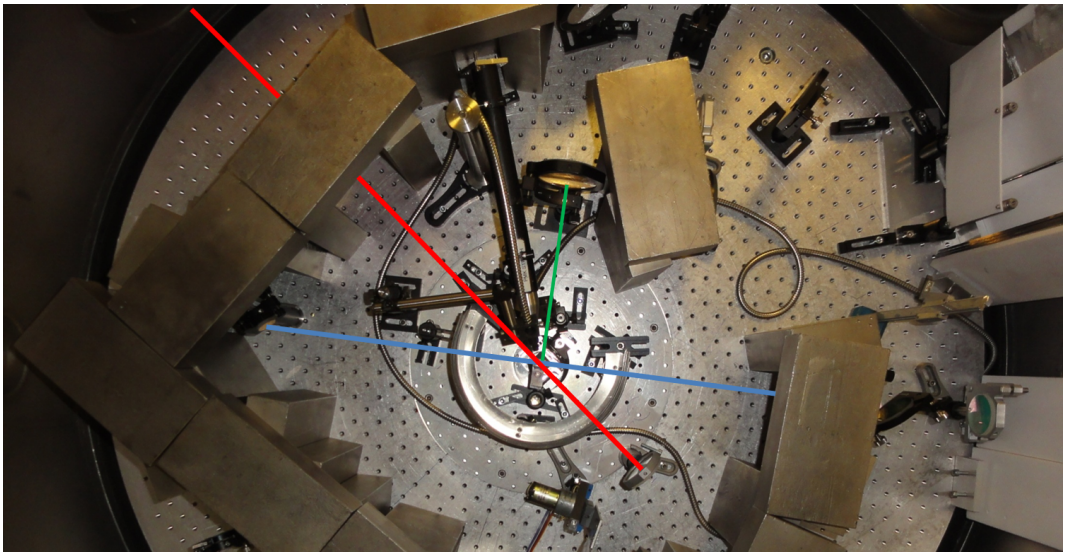

Figure 5.3: The experimental setup detailing the layout of the target alignment system. The laser diagnostic/TCC definition line is shown in red, with the transverse alignment beam in blue. The front surface imaging line is shown in green. A number of lead bricks were required to comply with radiological safety limits.

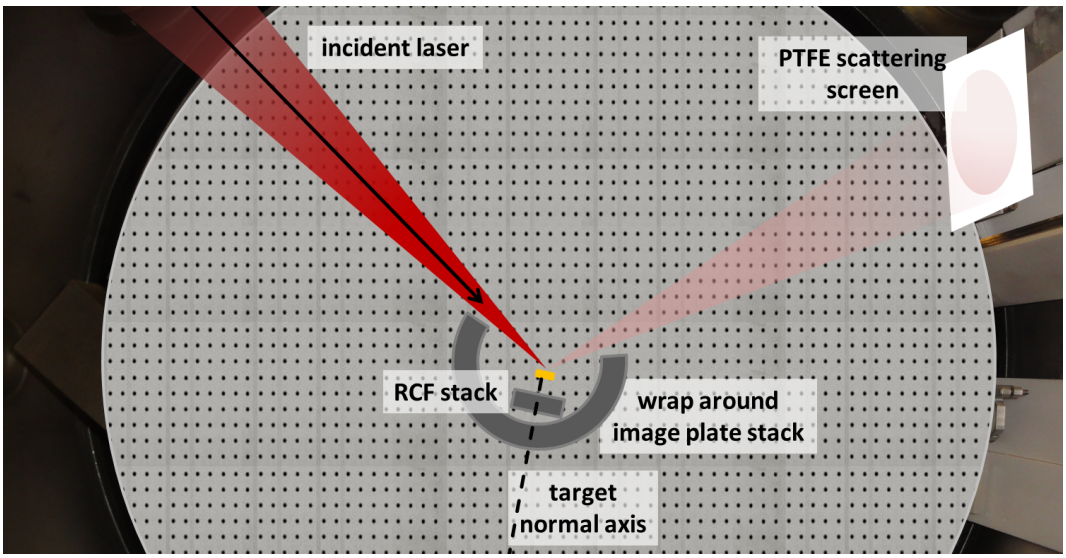

Figure 5.4: For simplicity a schematic experimental layout is also given detailing diagnostic positions.

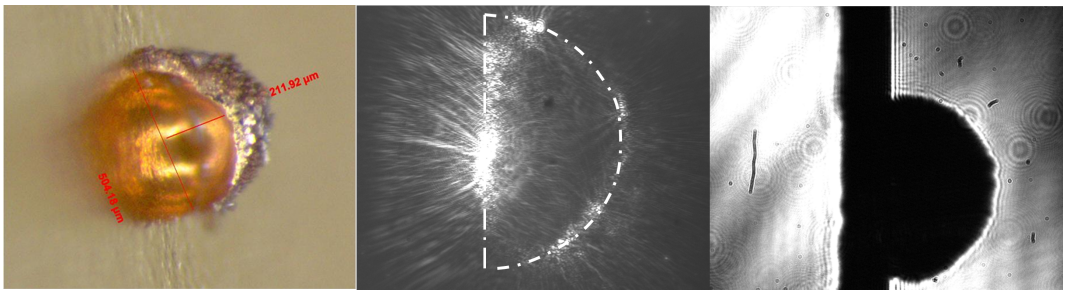

Figure 5.5: Reference views of the cavity targets. (left) A visible light image of the target, roughly from the point of view of the incoming laser. (centre) The front view alignment channel showing the cavity illuminated by the infra red alignment laser which is positioned at the sphere focus. Note that the laser spot appears large here due to the long exposure time used to captured the cavity. A broken line is used to guide the eye. (right) The transverse alignment channel used to position focus and showing the cavity from its end elevation.

to the target defines the target incidence angle. Thirdly, a target front view is installed that gives a view directly normal to the target front surface and allows the focal spot of the laser to be positioned on the target front. These positions can be easily cross referenced on each imaging line by using an appropriate wire thickness of approximately the focal spot size to obscure the focus and have all cameras focussed on the wire tip.

Using glass slide resolution test targets, the resolution of the target front and side view were found to be 11 μm and 20 μm respectively, allowing sub-spot size orientation of the laser spot with respect to the cavity, as well as an orientation on the focussing plane well below the Rayleigh length, indicating a reproducibility of on target intensity to within 2 % due to positioning error.

5.3 Experimental results

The proton energy spectra obtained for four shots from the experimental campaign are presented in figure 5.6. These were obtained for constant laser parameters incident on a single planar foil target as a control measurement and three plasma half cavity targets with radii of 100, 210 and 250 μm, corresponding to pulse separation of 670, 1400 and 1730 fs, respectively.

The interaction of the laser pulse with the planar foil is indicative of the single temperature proton spectra typically observed in laser plasma interactions in this intensity regime. On introduction of the two larger half cavity targets, a significant increase in laser to proton energy conversion efficiency of 56 % is observed in the lower half of the energy spectrum and generally a larger proton number is measured over the full energy spectrum for all half cavities. With proton numbers exponentially decreasing as energy increases it is clear that the total conversion efficiency enhancement is dominated by the number of protons accelerated in the low energy region of the spectrum.

Figure 5.7, shows an enhancement factor, where the dose observed at a given proton energy is normalised to the dose obtained at the same energy for the planar foil interaction. In general, the enhancement factor is larger at higher proton energies, which is indicative of an increase in proton temperature; the normalised difference in two exponential distributions becomes larger as they increase. Such an increase in temperature could be explained by the post pulse creating an effective pulse duration increase, seeding hot electrons in the sheath for a longer time [48, 115].

Similarly, this mechanism would be expected to increase the maximum proton energy. However, no target geometry showed dose above signal to noise on the RCF layer corresponding to proton energy of 15.2 MeV, with all having detectable dose at 13.8 MeV on the previous layer.

The interactions involving the smallest radius half cavity show smaller but generally similar enhancement trends across the spectrum but with a pronounced

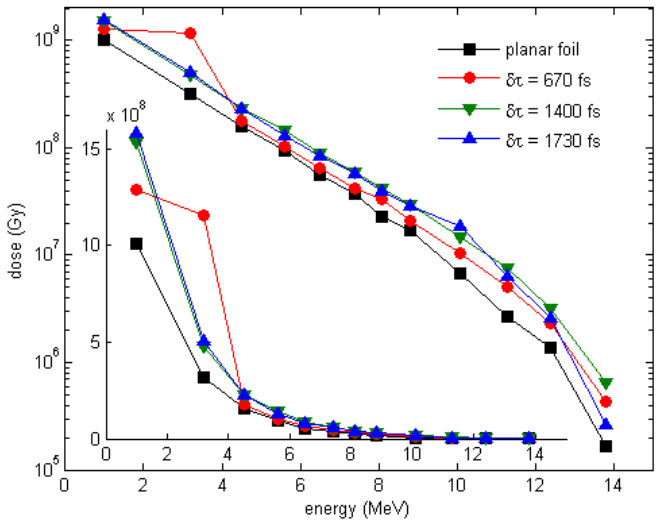

Figure 5.6: The proton spectra for a planar foil and three of the half cavity targets tested, on a logarithmic scale and inset on a linear scale.

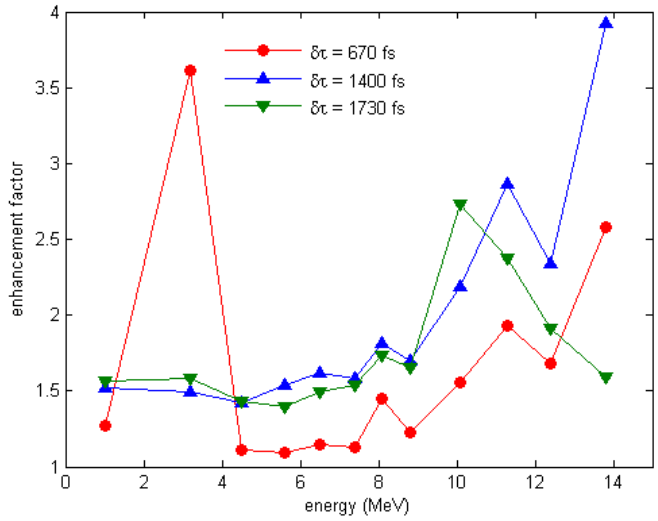

Figure 5.7: The enhancement factor as a function of energy for each of the plasma half cavity proton spectra.

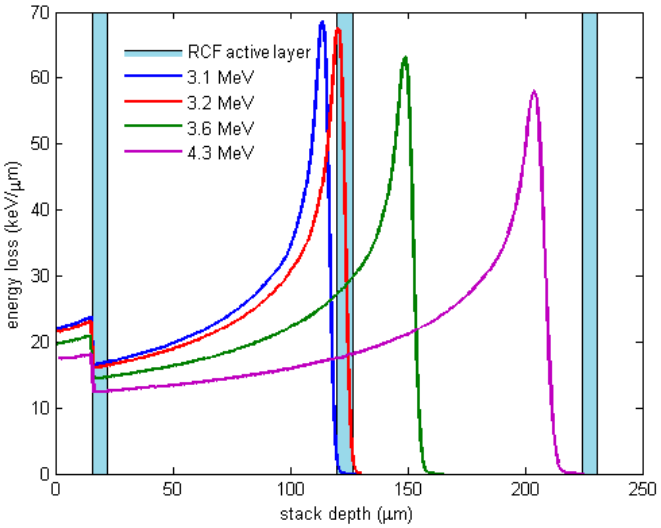

Figure 5.8: The RCF detector stack response to selected proton energies relevant to the observed anomalous spectral feature.

dose enhancement at 3.2 MeV, where three and a half times the number of protons are produced compared to the planar foil interaction. This may be explained by a peak in the proton spectra, which is predicted in simulation of multi-pulse interactions [56], and the finite width of the RCF active layer indicates that any spectral peak would lie in the range of $3.2 - 3.3$ MeV. The 2D spatial intensity distribution and divergence of the protons are very similar for both the planar foil and cavity target shots, strongly indicating that the protons come from a single source and that the mechanism responsible for the enhancement and the spectral feature originates in the sheath of the planar foil.

Several simulated Bragg peaks from the Monte Carlo algorithm SRIM [76] are given in figure 5.8 for selected energies relevant to the discussion of the possible proton spectral shape of the small cavity. While the second RCF layer corresponds to the position where a 3.2 MeV proton deposits the bulk of its energy, depending on the relative number of protons accelerated to other energies their dose contribution to the second RCF layer will differ.

The observed spectrum may be described by a large depletion of protons accelerated below energies of ~ 3.6 MeV as these protons would leave similar doses on the first two layers of RCF, provided that a large enhancement in the

number of protons at the higher end of this range was still generated. Similarly a depletion in the number of protons in the entire region of 1.0-4.3 MeV with a single monoenergetic peak at $\sim$ 3.2 MeV would yield a similar trace.

Taking this further, it is clear that a number of complex spectral shapes could exist below an energy of 4.3 MeV without any effects being observed on deeper layers of RCF, provided the spectrum has some single temperature distribution beyond this point. Although this approach can in principle be used to retrospectively fit a distribution to the detector response, this is a consequence of assuming some mathematically rooted approach in surmising the spectral shapes. In reality these descriptions would require the spectra to have complex distributions, which have not been observed in TNSA experiments to date. Furthermore it is unclear which mechanism could be responsible for such a radical alteration to the persistent single temperature spectra that are typically observed.

It is therefore most likely that the proton spectra can be explained by a single temperature proton spectrum with a modulation in the form of a spectral peak around the energy where the peak is observed, consistent with the modelling of *Robinson* [56] and experimental results of *Markey* [57] and *Brenner* [58]. It is however unknown which energy such a peak lies at, and with what energy spread. It is also the case that unless any such spectral peak coincidently lay exactly at 3.2 MeV, the total dose contained in the peak is likely to be higher than that recorded, and so should be considered a minimum in this sense.

The energy spectra in figure 5.6 were numerically integrated by a trapezoidal approach. These integrals were normalised to that obtained for the planar foil, giving a normalised integrated dose, which is proportional to the conversion efficiency, and is shown in figure 5.9. Here, the total proton conversion efficiency is observed to be doubled for the 100 μm radius half cavity, which assumes that the spectrum is flattened in this region. However, if the measured enhancement is a result of measuring a peak in the proton spectra the total proton dose may well be much lower, resulting in a large error bar in the measurement. This error is estimated by integrating the spectra by the same method but neglecting the dose

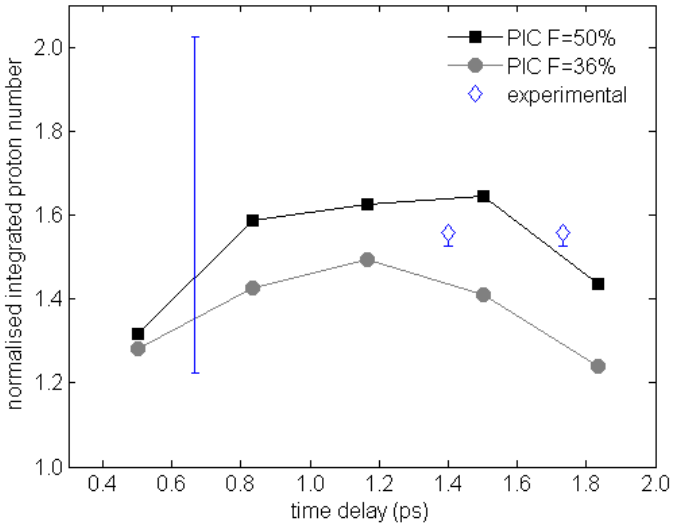

Figure 5.9: The integrated experimental proton dose compared with simulation results. Both experimental and simulation results are normalised to the corresponding single pulse planar foil interactions. In the case of the short time delay, small radius cavity, an error bar represents the range in conversion efficiency, as discussed in the text, a detailed shape of the spectrum is not known.

measurement for protons of 3.2 MeV. The quasi-Maxwellian spectra are relatively unaffected by this change, but in ignoring the peak in the anomalous spectra, the integrated dose falls from a 200 % enhancement to a 120 % enhancement.

The possibility that heavier ions cause the observed spectral feature on the RCF stack must also be considered. As no heavy ion diagnostics were fielded on the experiment there are no direct measurements of the heavy ion spectra. The heavy ions that would be accelerated to highest energy is C^{6+} which is the next lowest mass most naturally abundant element with the highest charge to mass ratio. It can be shown using SRIM that C^{6+} ions would require an energy of at least 1.5 MeV/nucleon for the straggling part of the Bragg curve to penetrate the 15 μm thick protective aluminium shielding the first active layer of the detector stack, and require an energy of 5.7 MeV/nucleon to reach the second RCF active layer. While energies in this range are theoretically possible using lasers similar to that used here [116], experiments reporting these have required careful target preparation techniques to remove the preferentially accelerated high charge to mass protons [45, 117], which inhibit the acceleration of heavier ions [118]. In ion

acceleration experiments at this intensity where the target has not been treated, much lower maximum energies have been observed [119], and therefore it is highly unlikely that these ions will have made any contribution to the dose recorded on the RCF. In normal uncleaned targets, it has been widely shown that proton acceleration dominates.

The radial distribution recorded on the wrap around image plate stack show little variance in the spatial distribution, but compared with the single pulse shot, all of the cavity shots recorded a consistent 50 % higher signal in photo stimulated luminescence. This is an indication that a larger number of electrons were seeded on cavity target shots. Caution must however be taken in using this diagnostic to estimate total electron numbers, as it is sensitive not only to electrons but also to x-rays which could be generated in large numbers on cavity shots. Whilst it is true that x-rays are indicative of electron numbers, the x-ray generation is nonlinearly related to the electron energies and will have a complex relationship.

5.4 Numerical modelling

The experimental integrated proton dose data is compared with simulations using the one dimensional collisionless particle in cell code, ELPS [56]. The collisionless nature of the code is generally assumed to be valid as the dominant absorption mechanisms generating the relativistic electrons of interest here are collisionless as described in section 2.3.2 and the model of relativistic electrons driving the acceleration via collisionless electrostatic fields has been shown to be valid through a number of analytic models which well describe the TNSA mechanism, such as the Mora model, described in section 2.4.2.2.

The intensity scalings of important parameters produced by the code, such as the hot electron temperature, maximum proton energy and laser to proton energy conversion efficiency have been extensively benchmarked by *Brenner* [58] specific to the TNSA mechanism, and compare well to the scalings obtained in experiment. The code has also been used by *Robinson* to reproduce the analytic

scalings of the light sail [61] and hole boring [65] variants of RPA, as well as agreeing with global features produced in an ideal Eulerian Vlasov Fokker Planck solver when applied to the TNSA relevant multiple pulse sheath acceleration mechanism [56]. The codes widespread applicability to laser driven ion acceleration and good agreement with experiment lend confidence that it is applicable to the modelling of this case.

In the simulations, a main pulse was followed by a post pulse of variable intensity ratio, determined by F, as in figure 5.1, with temporal delays ranging from $0.5 - 1.8$ ps, corresponding to a half cavity radius range of $75 - 275$ μm. Simulations had 2.5×10^5 electron, proton and ion macroparticles each, with each species initially uniformly distributed through a one micron region of the grid representing the target. By using a reduced target thickness realistic target densities were achieved while keeping the number of macroparticles low enough for feasible simulation times. Simulations were run in a box of sufficient width to contain the whole interaction over the 4 ps simulation duration, where the simulation duration was chosen to allow sufficient time for protons to approach their final energy asymptote. Foil ions were given sufficient mass to remain relatively static throughout the interaction and were assigned a charge state of one; again this keeps electron numbers low. A laser of wavelength 1.053 μm and 0.5 ps FWHM duration was used, with intensities defined through the dimensionless laser parameter, $a_0 = 4.1$, for the main pulse, to reflect the experimental parameters. A reference simulation was run representing a single laser pulse, $a_0 = 4.1$, interacting with a planar foil.

A second reference simulation was run to investigate the energy scaling of the single pulse interaction. This was done to separate the effect of the enhanced laser energy from the dual pulse effect, both of which occur due to the energy reflected from the cavity. Here, the sum of the energy of the primary pulse and secondary pulse was contained within a single 0.5 ps pulse, with $a_0 = 4.8$, due to the additional 36 % energy in the pulse.

The total proton conversion efficiency for simulations involving double pulse

interactions are normalised to the total proton conversion efficiency given by a single pulse interaction, $a_0 = 4.1$, and these are presented in figure 5.9. F values of, 0.36 and 0.50 were simulated and it was found that for $F = 0.36$, the proton yield is increased on introduction of a post pulse, and is predicted to be optimised for a delay of 1.2 ps, with an enhancement of 50 % compared to the planar foil shot. As F increases further to 0.50 the conversion efficiency can be improved by as much as 65 %.

Both simulation and experimental results show a correlation between time delay and the proton conversion efficiency. The time delay between pulses is important both from the laser plasma interaction perspective and also in terms of the multi-pulse effects at the rear of the target.

Small increases in the scale length of underdense plasma on the front surface have been shown to enhance proton acceleration and increase the maximum proton energy [120]; this is attributed to self focussing and absorption of the laser beam in the preplasma [121]. In the half cavity target geometry the primary pulse interaction with the foil seeds plasma expansion on the front surface which the secondary pulse goes on to interact with. As the delay between the two pulses increases, the scale length that the secondary pulse interacts with also increases, potentially giving enhanced laser energy to proton conversion efficiency. Similarly, there is a plasma expansion on the target rear through TNSA and as the secondary pulse arrives later in time the hot electrons are injected into a longer scale length expanding plasma, which has been shown to cause inferior electric fields to be generated than in the sharp boundary case [49, 50]. This results in an optimum delay where the two effects are balanced.

In the simulations it is very clearly observed as shown in figure 5.11 that a single pulse type interaction produces a hot electron population which peaks in temperature at a time of 800 fs after the initial interaction begins, or 300 fs after the peak of the main pulse. The electrons then rapidly cool as their energy is transferred to the ions of the expanding plasma, as shown in figure 5.10.

When the secondary pulse interacts with the target two predominant effects

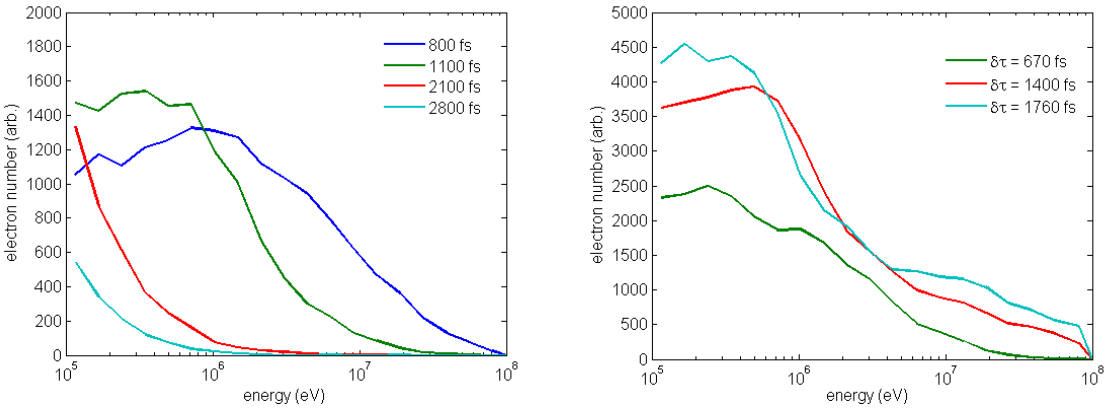

Figure 5.10: (left) The evolution of the electron spectra with time for a single pulse type interaction. The electron temperature peaks at 300 fs after the peak of the main pulse interacts with the plasma. (right) The electron energy spectra are shown for selected double pulse interactions corresponding to times when the electron population is close to its maximum in terms of number density.

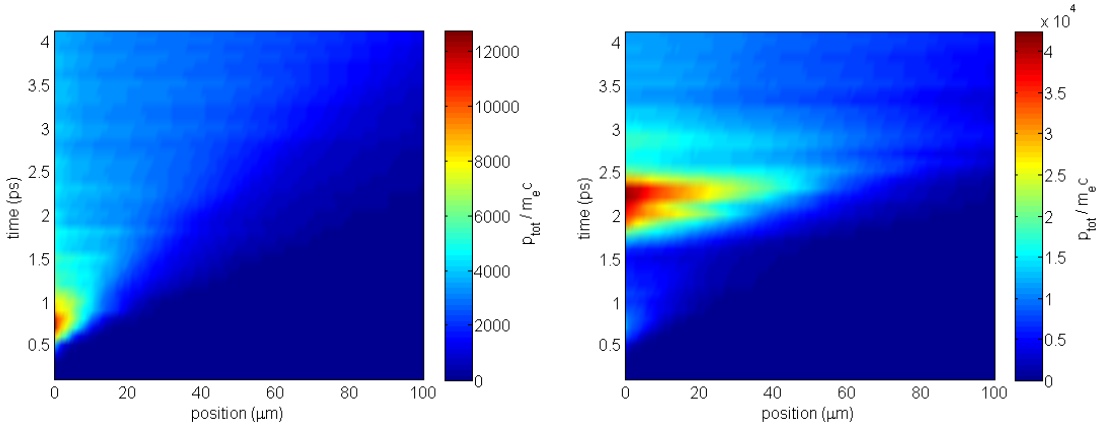

Figure 5.11: The total electron momentum as a function of time shown for a single pulse interaction (left) and a double pulse interaction with a time delay of 1.3 ps (right). All figures from this point unless otherwise stated take the point of 0 μm to define the target rear edge.

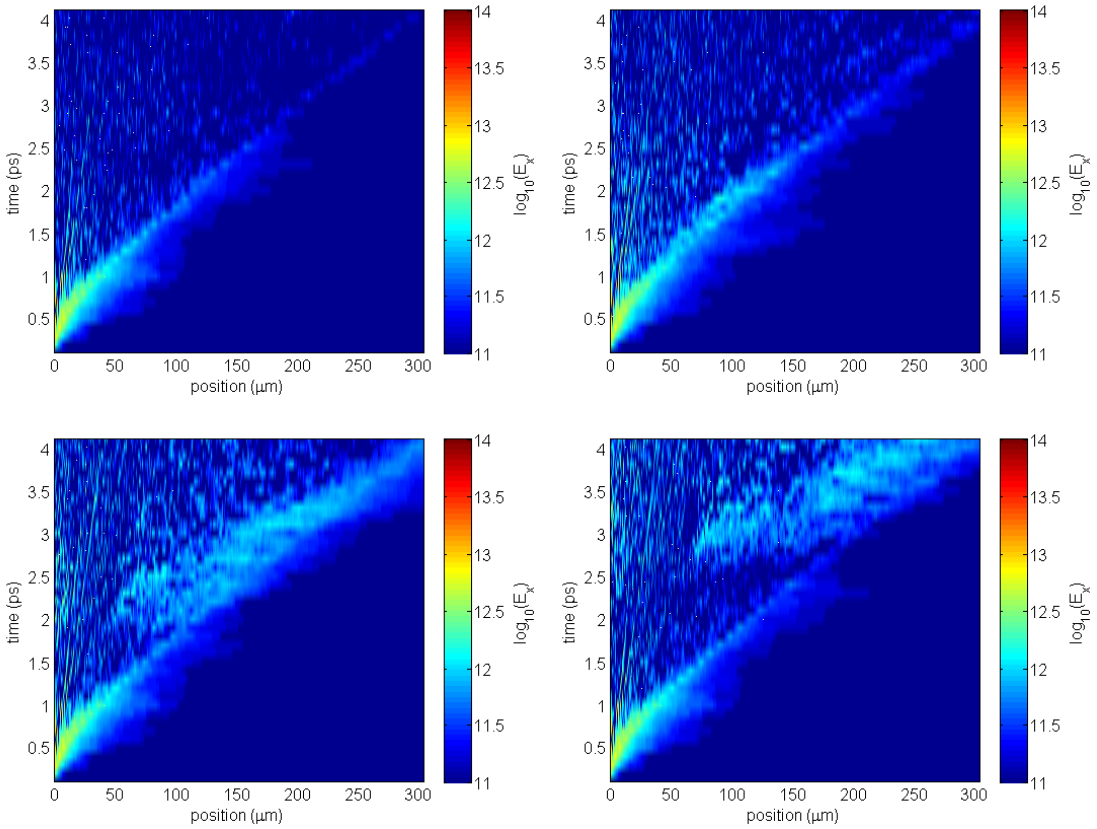

Figure 5.12: The positive E_x component of the electric field as a function of time for single pulse interaction (top left) and double pulse interactions from 0.7 ps, 2.0 ps and 1.3 ps (clockwise from top right).

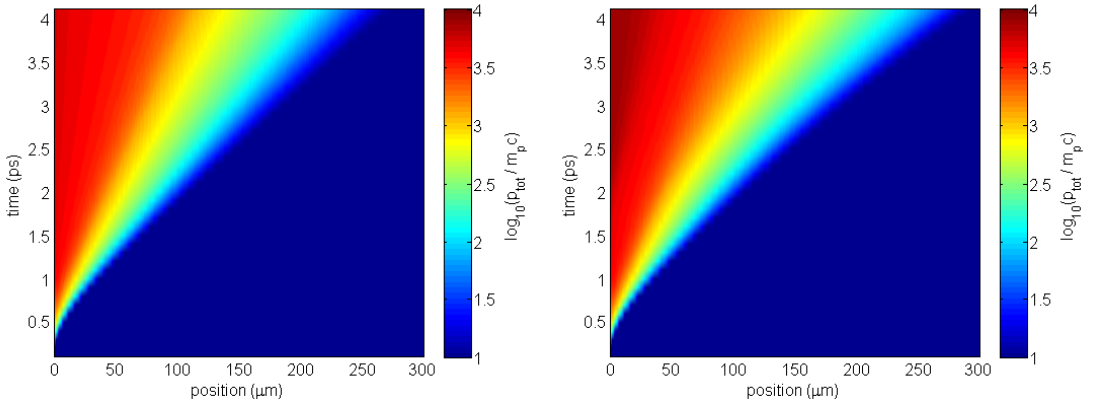

Figure 5.13: The total proton momentum as a function of time shown for a single pulse interaction (left) and a double pulse interaction with a time delay of 1.3 ps (right).

take place. First, as the time delay moves from short time to later time a larger number of hot electrons are generated as the pulse interacts with the preplasma on the front side of the target. Secondly, at its maximum, a complex hot electron temperature evolves after the interaction of the post pulse, which is shown in figure 5.10, where generally the colder and higher number density portion of the electron temperature, and hence the electrons most likely to be involved in the bulk ion acceleration process, reduces as the time between pulses is increased. The lower number density hotter component of the hot electron distribution seems to remain relatively unaffected by the time delay, if slightly increasing with time, which is an indicator that the maximum proton energy might be increased over time.

The total electron momentum on a spatial grid is plotted with respect to time in figure 5.11 to show the electron evolution for the optimal double pulse type interaction. Note the two differing scales on the figures. For comparison of scale, as the post pulse of figure 5.11 begins its interaction at a time of ~ 1.3 ps the two interactions can be considered to be equivalent up to this point. The effect of the electron distributions alone cannot describe how the ion acceleration mechanism evolves, and the primary mechanism for the inhibition of ion acceleration is the deterioration of a steep density gradient on the target rear.

Figure 5.12 shows how the accelerating component of the electric field varies in time for a single pulse, the optimum time delay and the two extremes where the proton acceleration is enhanced to a lesser extent. When this is coupled with the total proton momenta evolution given in figure 5.13, which is essentially a product of the ion density profile and the momentum distribution, a clearer picture emerges of how the electron population of the post pulse interacts to produce the observed laser energy to proton conversion efficiency enhancement.

Using the single pulse accelerating field as the natural reference, the electric field enhancement due to the introduction of the post pulse at the early time of 700 fs results in a field enhancement for a period roughly equal to the delay time between the pulses. This field enhancement is predominantly in the region

corresponding to where the highest energy protons are, and so they are accelerated to higher energies compared with the single pulse case. As the proton density gradient remains steep at the point of interaction of the post pulse, it acts predominantly on the higher momentum ions accelerated from the initial pulse. However, because of the relatively quick arrival of this post pulse in terms of the ion acceleration timescale, the effect is not optimised.

Conversely, as the post pulse is delivered at late time the maximum electric field at the maximum proton momentum front is allowed to decay, and is never restored to the same magnitude as that when the pulse is introduced at the optimal delay; this results in the maximum proton energy once again being reduced due to maximum field deterioration. Further, as the density scale length on the target lengthens, the accelerating field diffuses as a result, which has the effect of enhancing the acceleration of lower energy protons as the fields permeate to regions of lower average proton momentum, however, the fields are weaker due to the increased scale length.

It should be noted that while the field here appears to remain strong at late time, it is observed that the protons are asymptotically approaching a constant total momentum. This is therefore taken to be a good indication that the protons are close to asymptotically approaching their final energy and give a true representation of the final spectra.

Between these two cases lies an optimum, which occurs at a time delay of around 1.3 ps. Here, the maximum accelerating field acting on the highest momenta proton front does not significantly decay over time, and this results in a maximisation of the highest proton energies achieved. It should be noted that an enhancement in the proton maximum energy is observed to some extent for other time delays in figure 5.14, but this is where the effect is optimised. In addition the proton density gradient appears to take a second optimal value at this point; relative to longer time delays, the accelerating field permeates to a shorter depth but crucially as the ion scale length is shorter, the field acts on a larger momentum spread. This results in the acceleration of a larger range of proton momenta

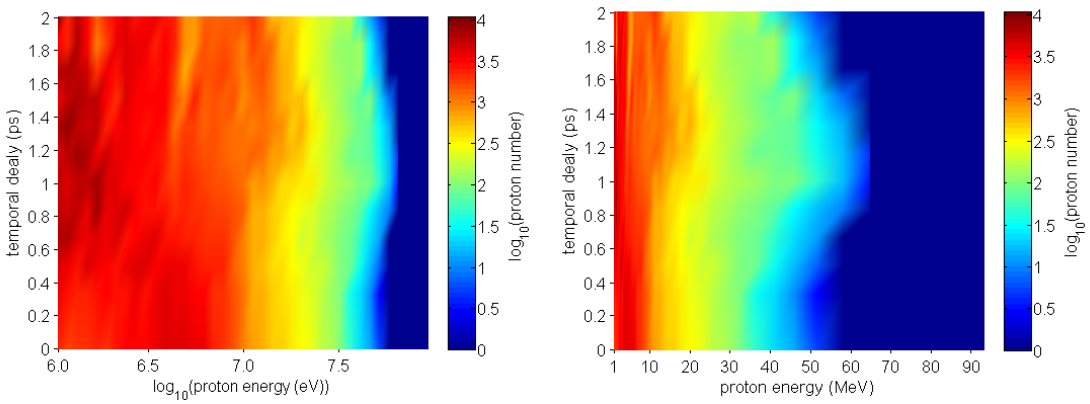

Figure 5.14: The final proton spectra as a function of the delay between the pulses, shown on a logarithmic scale (left) to more clearly show the low energy component which dominates the laser to proton energy conversion efficiency. The spectra are also shown on a linear scale (right) to give an overview of the spectra as a whole. It should be noted that the spectrum included at time t_0 is that of the reference case of $a_0 = 4.8$, and therefore laser energy is constant across the figure.

and with a strong accelerating field as it acts on a shorter density scale length than in the long delay case.

This description of the interplay between accelerating field and the density/momenta distributions on the target rear appear to be consistent with the production of the spectra and global features shown in figure 5.14.

Finally, in the reference simulation case where an $a_0 = 4.8$, single, 0.5 ps pulse is used, an increase in proton conversion efficiency of ~ 20 % is observed. Therefore by using a half cavity target to stage the delivery of the energy to the system a greater enhancement is achieved than by a single pulse with the same total energy.

5.5 Conclusions and discussion

The experimentally measured enhancement in the laser to proton energy conversion efficiency is consistent with simulations for F in the region of $0.36 - 0.50$ yielding a 50 % enhancement in the conversion efficiency, whilst retaining the fast ignition relevant, quasi-Maxwellian spectrum. While there is good agreement on the nature of the enhancement being predicted by the modelling to be a quasi-uniform over the whole spectrum, the predicted maximum energy increase is not something that is experimentally observed. This is despite the experimental indications that the cavity shots have a higher temperature proton spectra, and it is possible that any experimental energy enhancement was not observed due to the resolution of the RCF stack detector.

The spectral shape of the cavity target with the shortest time delay remains an open question, however, this is again due to the resolution of the RCF detector stack. This results in a large discrepancy between the enhancement predicted by numerical modelling for small time delay and that measured experimentally, due to the uncertainty in the structure of the low energy, high dose feature not predicted by the PIC code. The multi-pulse sheath acceleration mechanism [56], which is predicted to produce spectral peaks, may be a possible source of the feature, caused by localised field enhancement at the light ion front, which affects the proton acceleration.

PIC simulations which also included two to three species of carbon ions in the acceleration were run to investigate this possibility but no such spectral features were reproduced. It is possible and likely however, that real interactions where multiple light ion species are present, behave differently to these simulations. Such a mechanism should be identifiable on the trace of a Thomson parabola [82] diagnosing the interaction, which has high spectral resolution at low energy. In any future experiments this would be a mandatory diagnostic to resolve both the low energy proton spectra and ion spectra which may be influencing the evolution of the low energy spectral feature.

A similar RCF response was observed by *Markey et al.* [57] under similar experimental conditions; the rising edge of a 0.7 ps pulse is preceded by a prepulse of the same duration and separated in time by $\sim$ 0.75 ps and where the pulses had an intensity ratio of 0.4:1 rather than the 1:0.4 reported here.

A Thomson parabola would also identify the spectral shape of the low energy response and with many applications demanding spectral peaks and where flatter proton spectra provide a means for uniform isochoric heating, especially where the uniformity of proton heating has been a challenge until present, investigation into the mechanism producing this feature is warranted.

The proton energies reported in the numerical modelling here are relatively high compared with those expected and measured experimentally, and this as well as some other results from the modelling come as a result of using realistic electric fields in a one dimensional model and so some considerations of the one dimensional model must be made and its applicability justified.

Brenner [58] presents a thorough analysis of the dependency of the absorbed laser energy fraction as a function of both the incident laser intensity and pre-plasma scale length on the target front using the same code used here. While some factors that are known to affect the absorption differ, such as pulse length [34], the absorption measured in the modelling at 10^{19} Wcm^{-2} of 8.5 %, is similar to *Brenner*'s $\sim$ 8 %.

Although an absorption of 8 % is in poor agreement with experimentally measured values, because the electrons are restricted to one spatial dimension they can feasibly gain a higher temperature because they are spatially restricted and are not expelled from the laser field. The resulting hotter than physical temperature is ultimately transferred to the ions. The number of protons acquiring large energy are however very low and proton temperatures in the range of $\sim$ 1 MeV, from the modelling is in good agreement with experiment.

Similarly, while electron temperatures seem to be realistic, a large number of electrons are injected by the post pulse compared with the main driving pulse. Again *Brenner* showed that the introduction of a small scale length of $\sim$ 100 nm

can increase the absorption to around 11 %. Here, a scale length of the order of 150 nm results in absorption of 22 % of the laser energy of the post pulse in the case of the 1.3 ps delay. This however may be real to some extent, as the presence of a scale length on the target front surface has been shown to alter the absorption of the laser pulse [120].

Chapter 6

Double pulse ion acceleration in the long time delay regime

In this chapter, a scheme for enhancement of ion acceleration using double pulses is investigated. A controlled high intensity prepulse heats and initiates a target expansion, which a second, more intense laser pulse goes on to interact with at a later time. Initially, the maximum proton energies and conversion efficiency of laser to proton energy are found to be reduced, with a pulse delay of several to tens of picoseconds depending on the specific target material. With time delays in the tens of picoseconds however, the maximum energy and conversion efficiency are found to recover to close to their values for a single pulse interaction. This is explained by enhanced absorption in target front scale lengths significantly increasing the hot electron temperature. The maximum proton energies are reproduced by considering the interaction of different hot electron populations with rear surface density gradients, which are described by the bulk target dominated expansion for long pulse time delays. Experimental results and analytical treatment support this, with both showing strong target material dependence.

Analysis of the spatial profile of the proton beam shows the emergence of beam filamentation with time delay, as well as evidence for shock breakout causing large maximum proton energy and conversion efficiency reduction. The shock breakout is shown to be circumvented by choice of target thickness.

6.1 Introduction

Proton driven fast ignition offers some benefits in the inertial confinement scheme of fusion, as protons can be directed by focussing and deposit their energy in a highly localised manner. However, with the nanosecond time scales associated with compressing the fuel in fast ignition, the possibility of solid ion acceleration targets becoming heated by secondary sources and acquiring density gradients on either side of the target is likely; especially when such a target is required to be in millimetre proximity of the fuel capsule [108]. Even if a solid density ion acceleration target can be isolated from these sources through suitable target design, relaxation of design requirements offers the advantage of simplicity and lends itself to mass production, which is crucial for the realisation of a commercial fusion plant.

The simplest of all solid density target designs is the planar target foil, from which the vast majority of the experimental results in the field have come. Plasma scale lengths on the target front have been found to be beneficial to ion acceleration, where they have been observed to generally increase maximum proton energies and laser to proton energy conversion efficiency [55]. Target rear scale lengths, have however been largely shown to have the opposite effect on the TNSA mechanism [49, 50].

This chapter presents an experimental investigation into this combined effect, driven by double laser pulses. A thin target foil is subject to a relativistic intensity, picosecond laser interaction which quasi-isochorically heats the bulk target electrons to temperatures in the keV range [122, 123]. Following tens of picosecond plasma expansion, significant density scale lengths develop on both the front and rear target surfaces. By varying the main pulse introduction time, the plasma scale lengths with which it interacts are varied, and the extent to which the detrimental effects on ion acceleration, associated with target rear scale lengths can be mitigated by target front preplasma interaction is investigated.

For an interaction with a 0.5 ps laser pulse, the TNSA process typically spans

a few picoseconds, but the time delay between pulses reported here is up to 100 ps, with various physical processes coming into effect and varying in influence over time. For this reason, the data is first described largely qualitatively before an overview of a physical interpretation is presented in section 6.4.1.

6.2 Experimental method

The experiment was carried out using the PHELIX laser at the GSI facility, and the experimental geometry is presented in the annotated photograph in figure 6.1. The s-polarised, 1.054 μm wavelength laser light is delivered in 0.5 ps pulses to target by an $f/9$ off axis focussing parabola, where it forms a 20×15 μm spot, at a 34° angle of incidence. An average total on target energy of 65 J was delivered via the double pulse generator described in section 3.2.2, in a 1:10 controlled prepulse to main pulse energy ratio, giving the main pulse a peak intensity of 4×10^{18} Wcm^{-2}. The pulse delay was tunable from 0-100 ps and by blocking the appropriate arm of the double pulse generator, each single pulse could be delivered to the target chamber on its own.

The majority of the experimental results reported here were obtained using ultrafast Optical Parametric Amplification (uOPA) in the front end of the laser system [72], which is capable of delivering ultra-high contrast pulses of 10^{10} at 100 ps rising to 10^4 at 10 ps. Some shots used the standard CPA front end, which had a baseline ASE contrast level of 10^7 at 100 ps with a similar rise at 10 ps prior to the pulse peak. Other than the contrast difference, the beam energy and pulse duration remained constant, and so shots from the different front ends are comparable, but any minor effects possibly attributable to the contrast difference are discussed as they arise. All data presented are obtained on the uOPA front end unless otherwise stated.

The ion acceleration was diagnosed primarily by the use of 51×51 mm sheets of HDv2 radiochromic film in a stack configuration, located 51 mm directly behind the target. This provides the 2D spatial intensity distribution of the TNSA

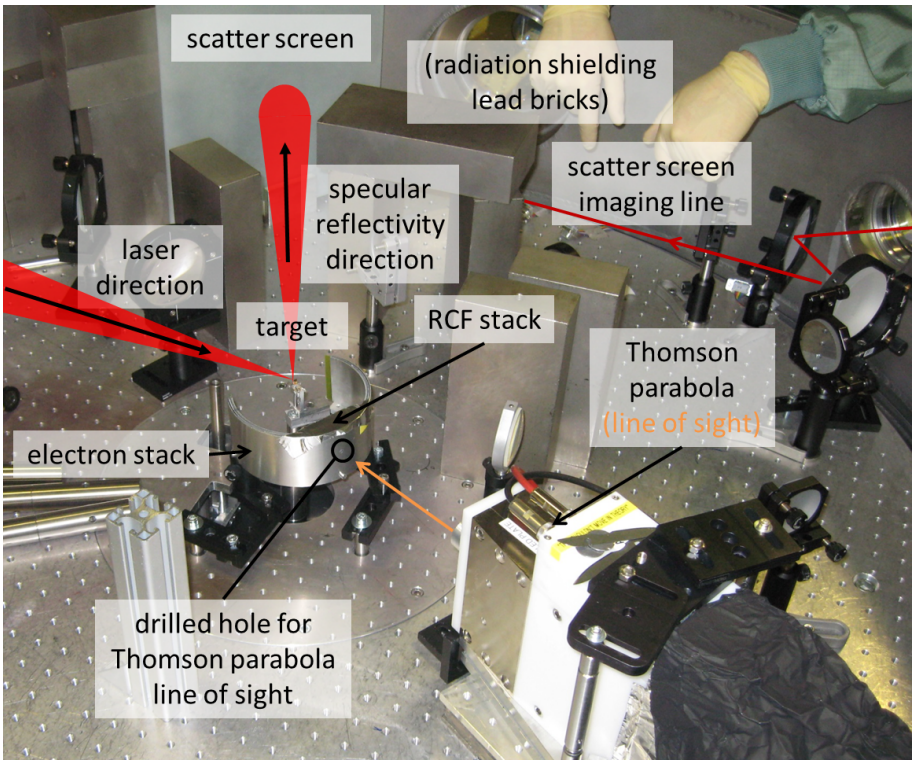

Figure 6.1: An annotated photograph showing the experimental geometry and diagnostics fielded on the experiment.

protons as well as their convolved spectra. A 2 mm diameter hole cut in the centre of the RCF stack provided a line of sight for a Thomson parabola ion spectrometer. The Thomson parabola used a 0.175 T magnetic field to provide high angular dispersion of low energy protons, giving resolution of around 0.1 MeV in the few MeV range. This complements the RCF energy resolution which is in the MeV range, and so reliable cut off energies can be measured with small error over a wider energy range as a whole.

In the specular reflectivity direction, a ground glass scatter screen was positioned. The constrained experimental geometry meant that the screen had to be imaged via a set of 3 inch mirrors, with a field of view of the scatter screen subtending the nominal laser $f/\#$. As the reflected beam was once again observed to be more divergent than the nominal $f/\#$ of the laser, the whole beam was not fully imaged on the scatter screen, however some of the detailed two dimensional intensity distribution data was retained.

6.3 Experimental results

6.3.1 Maximum proton energy and conversion efficiency variation with controlled prepulse time delay

The maximum proton energy was measured from the last layer of RCF in the detector stack which shows signal above the noise level. As the stack samples discrete energy bands along the spectrum, the resolution of the maximum energy is limited to the range between this and the proceeding layer, which is typically around 1.5 MeV across the stack.

With the laser operating in the double pulse mode, the effect of the temporal delay on the maximum proton energy was investigated, and the results of temporal delay scans are presented for shots on 5-25 μm thick gold foils in figure 6.2 and 45 μm thick graphite foils in figure 6.3.

The 5 μm thick gold foil scan in figure 6.2 is the only scan using two different front end amplification configurations. In the case of a single pulse interaction, the maximum proton energy is observed to be slightly higher when using the lower contrast front end. This could be due to the presence of a small preplasma generated by the lower contrast levels, which would reach a focussed intensity of 10^{11} Wcm^{-2}, nanoseconds prior to the interaction. Alternatively, this may simply be shot to shot variation. For transparency the data sets are distinguished and each data point is colour coded to indicate which front end produced the result.

Compared to the single pulse reference, the maximum proton energy is observed to decrease for prepulse to main pulse time delays of up to 10 ps, where the maximum proton energy is almost halved. A similar effect has been attributed to the presence of long, rear surface density scale lengths being detrimental to the ion acceleration mechanism [49, 50]. However, for greater time delays the maximum proton energy is observed to increase, and at 30 ps delay it is around 40 % larger than measured for a 10 ps delay. *McKenna et al.* reported a similar increase in maximum proton energy when a preplasma expansion was seeded

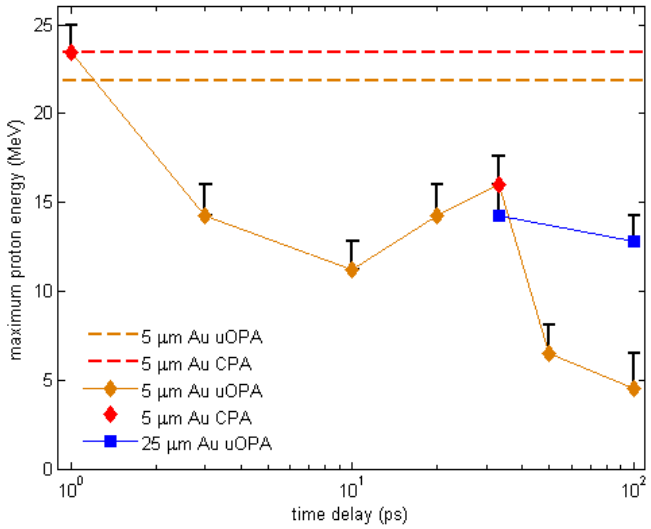

Figure 6.2: Maximum proton energy detected on RCF stack as a function of time delay for shots on 5 μm and 25 μm thick gold foils. The dashed lines represent the maximum proton energy observed from single pulse shots, and the colours of lines and data points correspond to the front end configuration with which the data was obtained. Note that as each RCF layer either records or does not record proton dose, the maximum measure energy therefore represents a minimum.

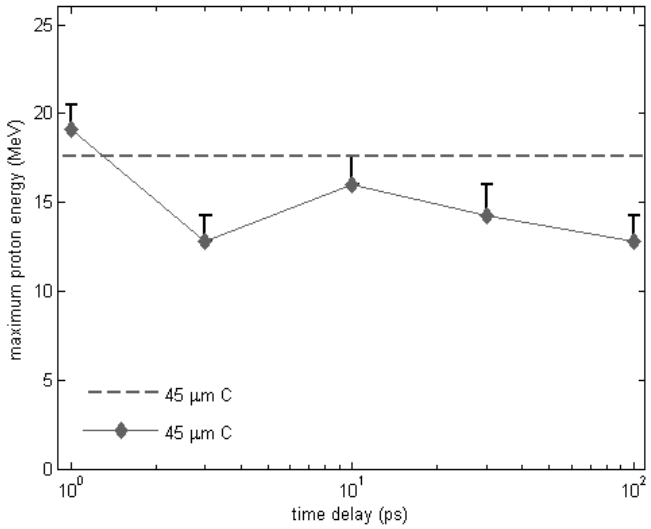

Figure 6.3: As in the style of figure 6.2, representing data obtained for 45 μm thick graphite foils. The data set was obtained entirely with the uOPA front end configuration.

on the target front surface by a nanosecond ablation beam [55]. In neither case however, have the protons been observed to recover a larger maximum energy after an initial large decrease. At very long time delays, from 50 to 100 ps, the maximum proton energy is observed to be reduced once again.

Experimental measurements of the maximum proton energy of 25 μm gold foils are also presented in figure 6.2. This shows the maximum proton energy observed for 25 μm gold is slightly lower than for the 5 μm gold targets at a time delay of 30 ps, which would be expected due to refluxing [53]. However, for increased time delay of 100 ps, the maximum proton energy obtained from the 25 μm gold is significantly higher than for the 5 μm gold foil. Thicker targets producing higher energy protons is inconsistent with published experimental data, and so this strongly indicates that the target thickness is an important factor in the long time delay regime, and this is investigated further in section 6.3.2.

In the case where a 45 μm thick graphite target is used, similar general trends in maximum proton energy are observed. The data set is more sparsely populated, but the maximum proton energy is once again observed to reduce with a 3 ps time delay between pulses, before recovering a higher maximum energy, this time at time delays of 10 ps and larger.

There are two notable differences between the trends observed for the 5 μm gold and 45 μm graphite targets. Firstly, the late time recovery of the proton energy appears at different time delays for the different target materials, indicating that this process is linked to the target material expansion rather than the TNSA mechanism which is rather independent of target material. In section 6.4.2, estimates are made of the target material dependent expansion velocities.

Secondly, the trend in graphite foils late time maximum proton energy, more closely resembles that observed for 25 μm gold foils than 5 μm gold foils. Again this will show a strong correlation with data presented in section 6.3.2.

Estimates of the laser to proton energy conversion efficiency are presented in figures 6.4 and 6.5, in terms of a normalised integrated proton dose measurement. Both of the integrated dose measurements take a form similar to the maximum

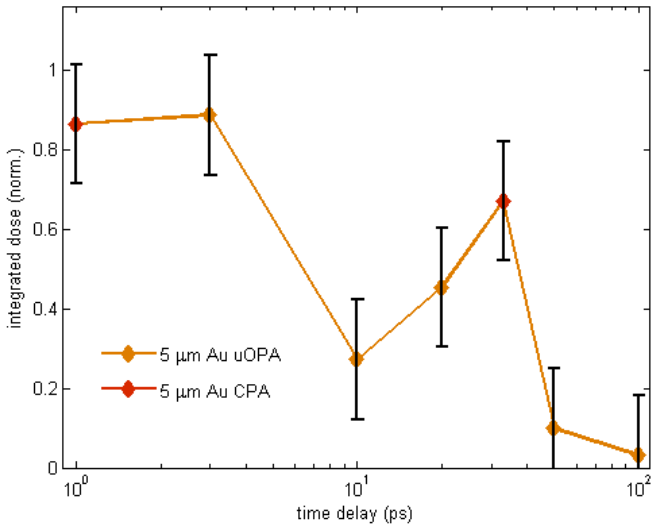

Figure 6.4: The variation in integrated proton dose, for protons of energy greater than 3 MeV for 5 μm gold foils. Each data point is normalised to the integrated proton dose measured on the corresponding single pulse shot. Error bars represent the estimated shot to shot variation.

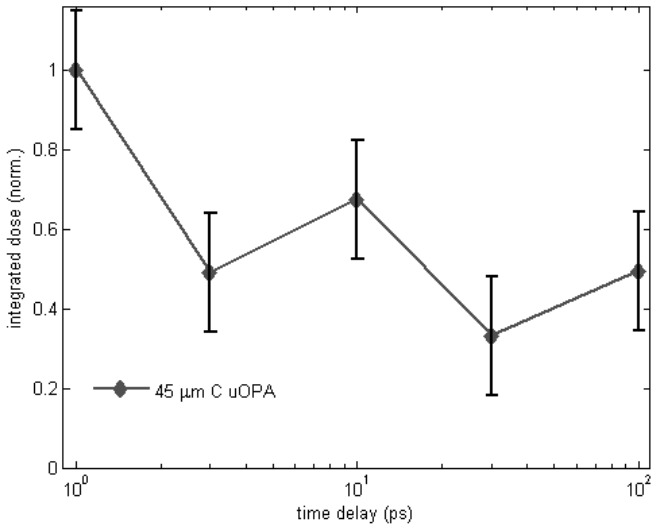

Figure 6.5: The variation in integrated proton dose, for protons of energy greater than 3 MeV for 45 μm graphite foils. Each data point is normalised to the integrated proton dose measured on the corresponding single pulse shot. Error bars represent the estimated shot to shot variation.

proton energy measurement for the target material, with the conversion efficiencies dropping at short time delay, before recovering at the same time delay as the maximum proton energies. The 5 μm gold foil conversion efficiencies are considerably reduced at long time delay, while the graphite foils yield an approximately constant dose.

The integrated dose of the 25 μm gold targets at time delay of 100 ps is 86 % of that measured at a 30 ps delay. This is a small reduction compared to the 5 μm case, where the integrated dose falls to 5 % of the 30 ps time delay measurement. As there is no zero time delay shot for 25 μm gold to normalise to, it cannot be included in figure 6.4.

An anomaly exists in the 5 μm gold scan in that the integrated proton dose obtained is higher for the 3 ps delay shot than in the 1 ps delay shot, while the maximum proton energy in the case of the 3 ps delay shot is observed to be reduced by around 50 %. This may be explained by a possible shock break out reducing the maximum energy as discussed in section 6.3.2, while the conversion efficiency is dominated by the low energy component of the spectrum which is effected less by the shock breakout.

The shot to shot laser energy variation across the data sets was found to be $\pm$ 7 %, and this was used to estimate the conversion efficiency variation expected by the experimental scalings of *Robson et al.* [115] and *Brenner et al.* [124].

6.3.2 Shock breakout diagnosed by the spatial profile of accelerated protons

In the past, the two dimensional spatial-intensity profile of the sheath accelerated protons have been shown to be useful as a diagnostic of shock breakout from the target rear surface. *Lindau et al.* [125] and *Lundh et al.* [114] observed that by controlling the contrast level, the ASE induced shock velocity could be controlled to arrive at the target rear at different times. When the shock wave arrived at the target rear, the target was deformed resulting in the highest energy protons being deflected from the normal direction, while the lower energy proton profile remained largely unaffected, due to their larger source size [126]. The deflected proton beams were also observed to have a reduced maximum energy, attributed to scale lengths developing on the target rear surface.

Additionally, *Lindau et al.* argue that the shock must not induce a phase transition in the bulk target to observe the beam deflection. Some of the relevant parameters for the target materials investigated here are listed in table 6.1. These indicate that a maximum prepulse or ASE level of around 10^{12} Wcm^{-2} could sustain the type of shock described in the literature.

Figure 6.6 shows the spatial distribution of both the low energy 3.2 MeV protons and maximum proton energies on the RCF stack, as a function of time delay between the main pulse and controlled prepulse and for the three different targets.

For single pulse interactions with 45 μm graphite foils, and double pulse shots with time delays of up to 30 ps, the highest energy proton beam has a small angular divergence, which is a typical feature of TNSA accelerated beams. The proton beam pointing varies, but this is due to small angle deviations in target alignment. However, on the 100 ps delay shot the divergence of the beam markedly increases, and perhaps begins to show the main proton signal to be deflected from normal.

The lower energy component of the beam is observed to vary in its spatial

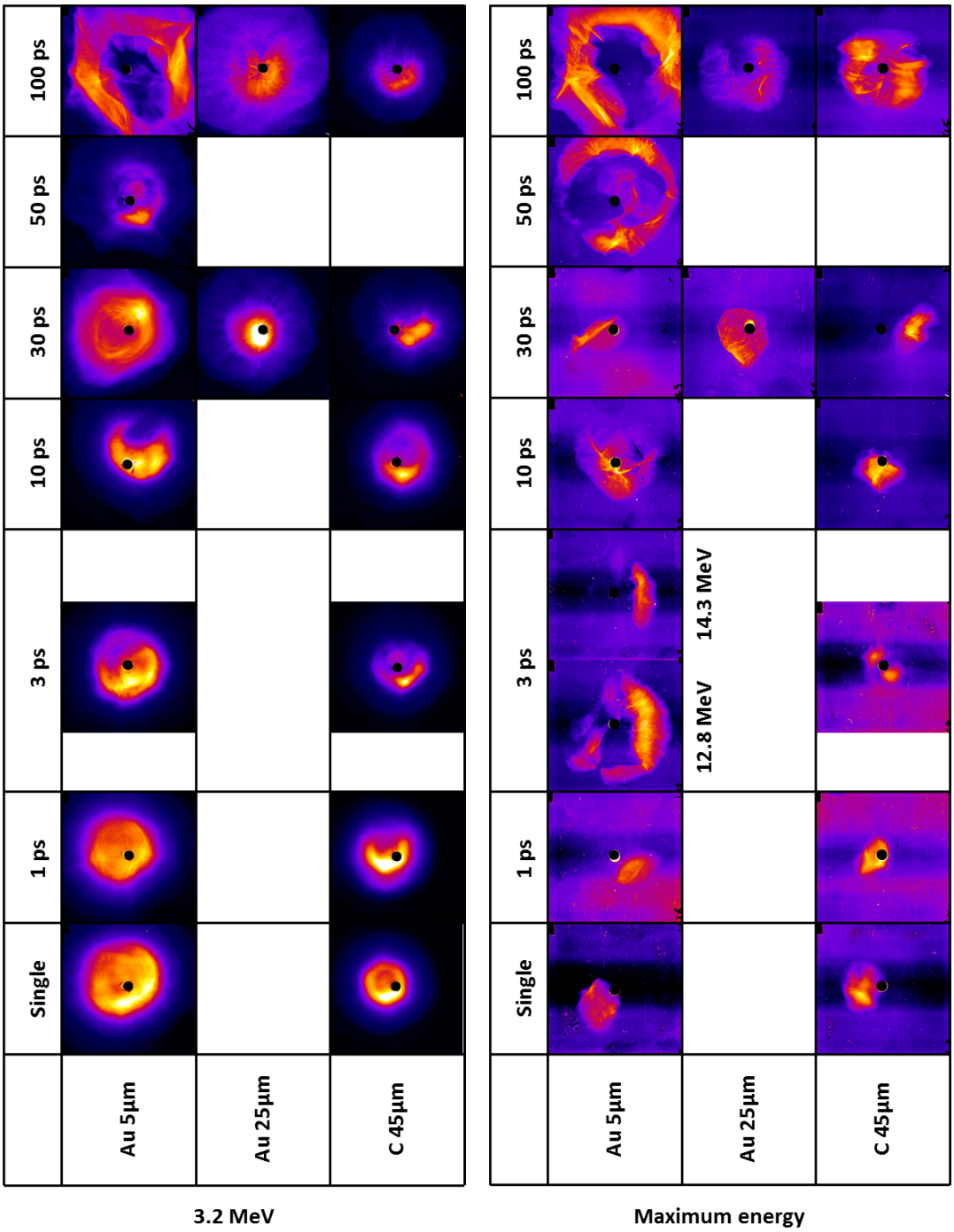

Figure 6.6: The two dimensional spatial intensity dose distribution of 3.2 MeV protons (left) and the maximum recorded proton energies (right), as a function of time delay between the main pulse and controlled prepulse and for the three different target types. Brighter coloured regions correspond to higher dose, and the colour scale is linear.

Material	P_m (GPa)	I_m (Wcm^{-2})	max v_s (μm ns^{-1})
Graphite	300	1.6×10^{12}	16
Gold	280	1.5×10^{12}	6.5

Table 6.1: Published values for melting pressure P_m, inferred laser intensity required to achieve the melting pressure, I_m, and maximum shock velocity v_s for the target materials used in this study [127, 128, 129].

distribution from shot to shot, but generally the divergence remains similar, until the distribution changes for time delays of 30 ps and longer. At a time delay of 100 ps the divergence of the low energy component of the beam is increased, but markedly more so for the higher energy component. This is consistent with the measurements of the type of shock breakout inferred by *Lindau et al.* [125] and *Lundh et al.* [114], where the divergence increases for high energies.

For 5 μm gold targets, a similar general trend is observed. A more divergent maximum energy proton beam is observed than compared with graphite targets, but is generally low in divergence up to a time delay of 30 ps. When the main pulse is delivered more than 30 ps after the controlled prepulse, a notable change in the proton beam distribution occurs. Here, instead of a low divergence beam, the bulk of the maximum energy proton beam is blown away from the centre and distributed in a ring like structure, which is consistent with the observations of a shock affecting the ion acceleration.

These combined observations from 5 μm gold and 45 μm graphite foils, would be consistent with a low intensity, $\sim 10^{12}$ Wcm^{-2}, prepulse around a nanosecond prior to the main pulse arrival, using the shock velocities in table 6.1, however, there is an anomalous shot in the 3 ps time delay. The high energy protons show a similar distribution to that of the 50 and 100 ps delays on gold. This indicates that if a prepulse is responsible for launching a shock, that there may be some quasi random nature to the time at which it is generated.

In addition to this, the distribution of the low energy proton beam indicate that the shock breakout is at a different stage at the 3 ps time delay compared to the 50 and 100 ps delays. At 3 ps the low energy proton beam is similar in

nature to the single pulse shot, where there is no evidence of a shock, and this is again consistent with the type of shock reported in the literature, where the lower energy protons are largely unaffected by the shock. However at 50 and 100 ps delays, the beam has a similar spatial profile to that at high energy, indicating that the shock has broken out over an extended region in these cases.

Distributions of the 25 μm gold foils is qualitatively more similar to the graphite foils, indicating no shock break out from the same extended region as for 5 μm foils. Accordingly, no significant reduction in the maximum proton energy is observed over this time delay for the thicker gold foils. With the main experimentally observed difference between thick and thin foils being the spatial profile of the protons, an extended shock breakout might be responsible for the marked reduction in maximum proton energy observed for 5 μm gold foils.

6.3.3 Time delay dependent proton beam filamentation

As the time delay between the prepulse and main pulse was increased, an increasing degree of fine structure was observed to be mapped on to the proton beam for both graphite and gold target foils, as shown in figures 6.7 and 6.8. For some time it has been assumed, and since experimentally verified that the shape [52] and structure [130] of the proton beam, from the target normal sheath acceleration mechanism, is determined by the electrostatic field gradients set up at the target rear. The field gradients are themselves determined by the fast electron density distribution at the rear surface.

The numerical code described by *MacLellan et al.* [131] has successfully reproduced the proton beam structure of many experiments, based on spatial modulations introduced to the electron density profile during transport through comparatively thick solid targets. Using this, *McKenna et al.* [132] have shown that an electron beam, filamenting into many smaller beamlets, results in acceleration of a filamented proton beam from the target rear, with a structure which is qualitatively similar to those reported here. The break up of the electron beam is attributed to conductivity differences of materials in the sub hundred electron-

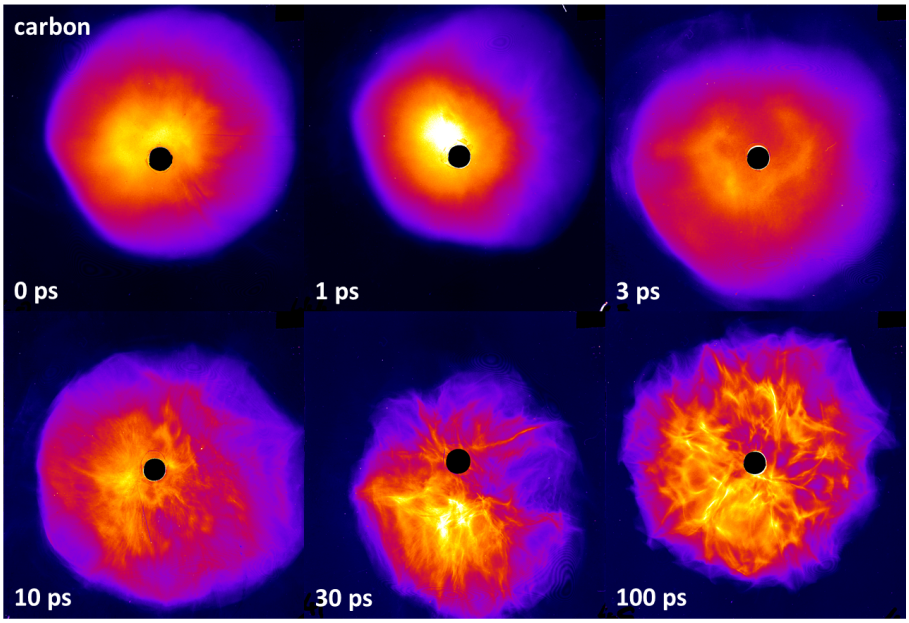

Figure 6.7: RCF dose maps show filamentation on proton beam structure emerging with increased temporal delay between the controlled prepulse and main pulse. The target here is 45 μm graphite.

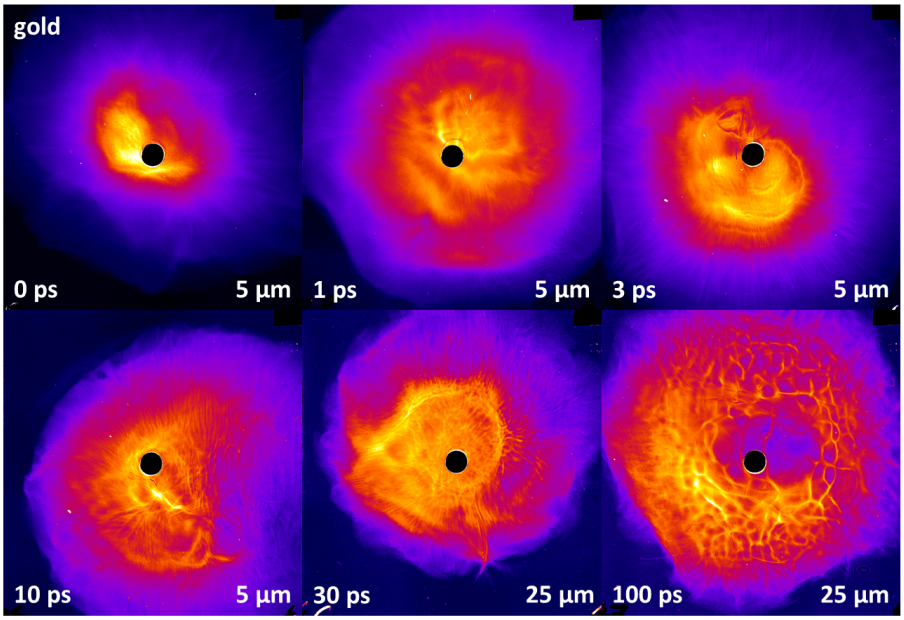

Figure 6.8: RCF dose maps show filamentation on proton beam structure emerging with increased temporal delay between the controlled prepulse and main pulse. The target here is 5-25 μm gold.

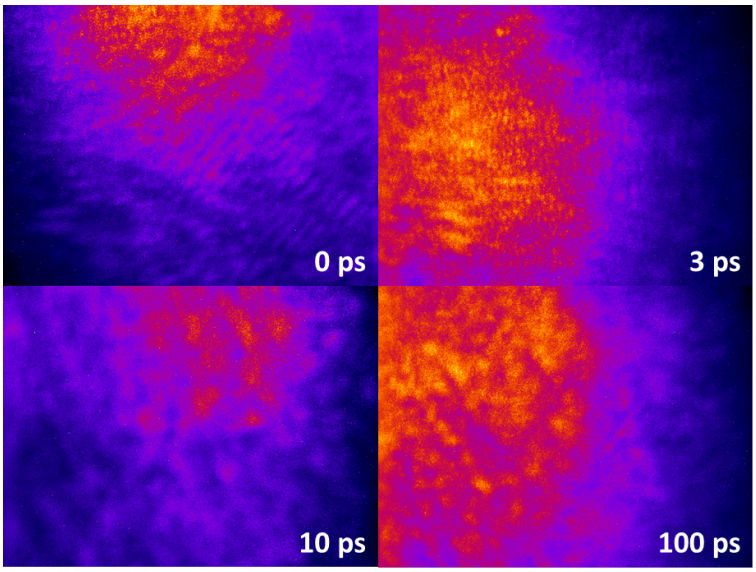

Figure 6.9: The two dimensional specularly reflected energy profile show that the bright region of the specularly reflected light becoming increasingly granular in structure, showing correlation with the proton beam structure.

volt temperature range, which is dependent on the differing lattice structures of the materials. To observe this effect, targets thicknesses in excess of 100 μm are required to ensure longitudinal temperature gradients exist such that the beam propagates through tens of microns of low temperature material [133].

The lattice structure dependent conductivity phenomenon is unlikely to explain the results observed here, as the targets were sufficiently thin that the bulk target temperature should be too high to observe this effect. It is also significant that this proton beam structure is observed in gold targets. *Quinn et al.* [134] found no proton beam structure from metallic foils up to 1 mm in thickness.

Filamentation of the electron beam being mapped on to the proton beam via the sheath field remains the most likely explanation for the observation. It is unlikely, however, that this filamentation arises from a transport effect and so an alternative mechanism for this electron density filamentation must be found.

Experimental measurements of the specularly reflected energy profile presents some evidence that the mechanism for the electron filaments may be taking place at the target front critical surface. The scatter screen measuring the specularly reflected laser energy in figure 6.9 provides some evidence for a change in the

spatial profile of the reflected light at the laser frequency. This light, being reflected from the critical surface carries some information about the conditions there, and in Appendix A, a strong correlation between the reflected quasi-near field intensity distribution and the condition of a perturbed critical surface is made. Figure 6.9 shows a qualitatively similar speckle structure emerging in the reflected laser light as the time delay between the pulses increases, indicating some change to the conditions of the critical surface over time.

Several mechanisms for rippling of the critical surface have been proposed, including surface wave generation [135], and the Weibel instability [136], which have been found in two dimensional PIC simulations. Recently, *Metzkes et al.* [137] have reported experimental findings where proton beams with similar filamentation structures to that here are observed, and are attributed to these mechanisms. Several similarities exist in the experiments, however there are also a number of differences. Interestingly, the observations are reported for 2-3 μm thick titanium foils, and so electron beam filamentation due to transport effects should not be significant, and so there may be a common physical process with these results. *Metzkes et al.* were also able to rule out the effect being dependent on target rear surface by changing the target rear material.

Metzkes finds a threshold prepulse intensity of 2×10^{14} Wcm^{-2}, 10 ps before the main pulse arrival. This timescale for the evolution of the structure in the proton beam is similar to that observed here, despite the prepulse intensity being much lower. Across this intensity range, the Weibel instability growth rate should be orders of magnitude greater for the higher intensity pulses, which generate faster electrons [138]. However, a lack of measurement of the relative scales at which the proposed instabilities grow makes this difficult to qualify.

Metzkes also finds a dependence on target thickness, with the effect being observed for 3 μm thick targets but not for 5.5 μm, which is not observed here when the target is changed from 5 μm to 45 μm.

With electron and proton beam filamentation having wider implications for applications, such as fast ignition or ion beam therapy, where the dose deposition

must be controllable and well known, the sources of this phenomenon is of interest and must be better understood. The number of free parameters that have been introduced between *Metzkes*' study and this do not allow for a complete isolation of the responsible mechanisms, and a dedicated study to the formation that further map the parameter space is required.

6.4 Modelling

6.4.1 Overview

In this section the nonlinearity of the time delay dependent maximum proton energy in section 6.3.1 is investigated through numerical and analytical modelling. It is the aim of this section to provide an overview of the key mechanisms and assumptions made at each stage, as they are considered individually in the proceeding subsections. Figure 6.10, diagrammatically splits the long time delay mechanism into four stages to aid discussion.

At t_0 in figure 6.10, a target with initially steep density gradients on both sides is assumed, and a controlled prepulse irradiates the target front at t_1, initiating two populations. The high density bulk target is the cold population, and the electron and ion species are denoted by n_{ec} and n_{ic} respectively. Additionally, the $\sim 10^{17}$ laser creates a hot population of electrons, which were experimentally observed to accelerate an ion population with maximum energy of 2.5±0.1 MeV, these species are denoted n_{eh17} and n_{ih17}.

Section 6.4.2 estimates the cold electron temperature seeded by the prepulse, and the average charge state of the ions at that temperature. This is important for an estimate of the front and rear surface scale length evolution for the two target materials investigated experimentally. The presence of the hot and cold density profiles either side of the target is briefly considered here in terms of its individual importance to the physical processes on each side.

The presence of an electron density scale length on the target front can cause the main pulse to relativistically self focus, provided the electron density is high

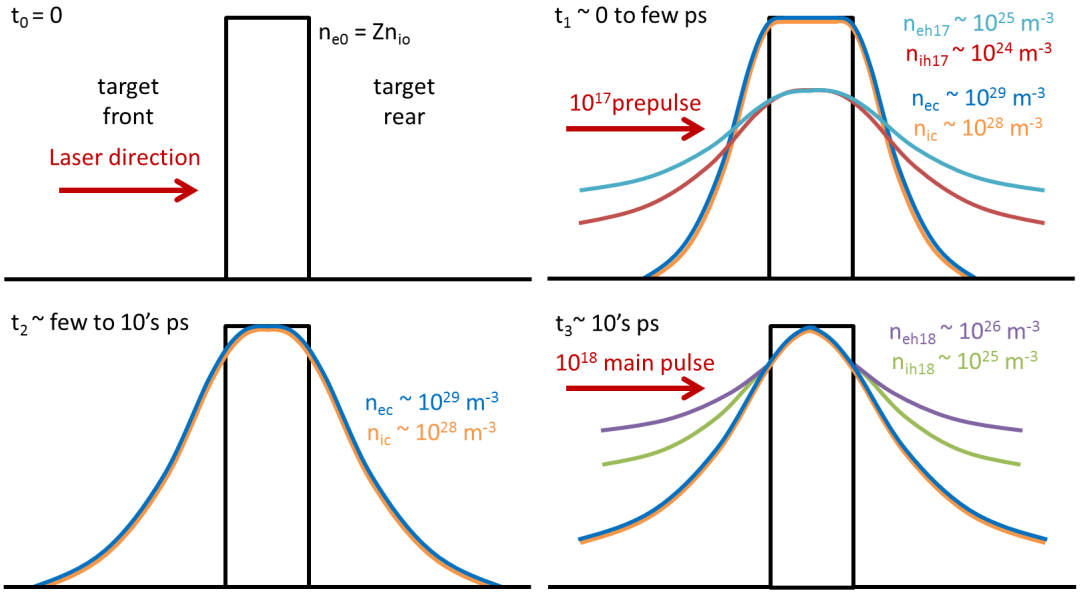

Figure 6.10: A visual aid for the discussion in the text of section 6.4.1. The electron and ion density gradients are visualised at four stages of the long time delay regime, and some estimates on the number densities are given.

enough that the laser meets the critical power criteria in equation 2.25. The low density hot electron population, n_{eh17} therefore does not significantly contribute to any induced self focussing in the preplasma. The higher density bulk plasma expansion, however, is important and its effect on the self focussing of the main pulse and generation of hot electrons is the subject of section 6.4.3.

For a two electron temperature plasma expansion where the density ratio of the cold to hot electron population is dominated by cold electrons, it has been found that the hot electron population cools much more rapidly than the bulk target, with the final temperature tending to a value closer to that of the cold population [139]. A similar but more simplistic approach is adopted here, where it is assumed that after tens of picoseconds, the scale lengths on both sides of the target are determined by the bulk target expansion alone, as at t_2 of figure 6.10.

Grismayer and Mora [49] modelled the ion acceleration from a hot electron population (from section 6.4.3) acting on a surface with existing cold plasma density gradients, and this was found to give good agreement with experimental results by *Fuchs et al.* [50]. Section 6.4.4 is concerned with applying this model to predict the maximum proton energies from scale lengths in section 6.4.2.

6.4.2 Bulk target properties induced by a controlled high intensity prepulse

As it was not possible to install optical diagnostics to experimentally measure the density gradients or target temperature, analytic and numerical modelling from the literature is relied upon to provide estimates of these. A two dimensional collisional particle in cell simulation which required significant resources far beyond that available for this study, but with similar laser and target conditions to the prepulse interaction reported here, were performed by *Sentoku et al.* [123] to investigate bulk target heating. This simulation looked at a 1 μm wavelength laser of intensity 7.5 $\times$ 10^{17} Wcm^{-2} and pulse duration of 500 fs, incident on a 5 μm thick plasma slab with a density of 140 n_{crit}.

In the collisional case, the resistive electric field induces a collimating magnetic field [140], of a magnitude which was found to complement the Larmor radius of the lower temperature hot electrons, and this acts to minimise transverse spreading of the beam in the target. It is then the lower energy hot electrons from the pulse that deposit their energy into the bulk target, and this gives a quasi-uniform heating of the plasma longitudinally over the central $\sim$ 10 μm to temperatures of 3-4 keV with little transverse temperature gradient across the 5 μm target width. This temperature compares well with experimental data, where the central laser spot region of an aluminium foil has been inferred to be 1.5 keV [122], for a 2×10^{18} Wcm^{-2} interaction.

The conditions of the collisional PIC model more closely match those of the controlled prepulse in the experiment, while the experimental data cited must be given weight as they report on real measurements for parameters close to that of those here. For this reason, the PIC values might be thought of as idealised, but the range of 1.5-4 keV provide a valuable range within which the temperature might can expected to realistically be bound within.

This range of experimentally measured to ideal plasma temperature can be used to estimate the plasma expansion velocity and resultant plasma scale length.

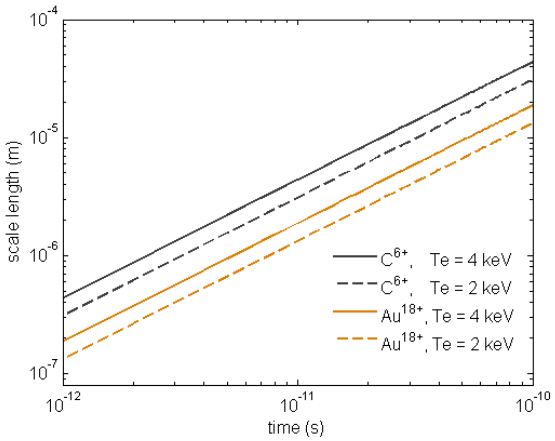

Figure 6.11: An estimate of the scale lengths as a function of time, due to the bulk target self similar expansion.

As shown in figure 6.11, the specific temperature of the plasma is not required to be precisely known for a first order estimate for a given charge state. The small change in scale length with temperature comes as a result of the expansion velocity scaling with the plasma electron temperature as $T_e^{1/2}$, and is therefore robust to changes in factors of two in the assumed temperature.

As well as the electron temperature of the plasma, an average ionisation state is needed to estimate the target expansion velocity. Theoretical methods of obtaining the mean ionisation state of ions in hot dense plasma is an ongoing area of research [141]. A typical method for deducing the ionisation state would be to solve the Saha-Boltzmann equation, however there are a few immediate problems with this approach. Firstly, for gold, which the problem is of principle interest, the high atomic number means that a very large number of excited states can exist, meaning that the coupled equations of the Saha-Boltzmann approach quickly become intractable. The fundamental premise of the Saha-Boltzmann approach is even called into question as it assumes a optically thick plasma which is in local thermodynamic equilibrium. This may not however be the case, as the dense laser plasma is transparent to its own radiation and often not in local thermodynamic equilibrium. This adds a further degree of complexity to the task, as atomic rate equations must be considered [142].

The charge state of gold is therefore estimated to a first order, and obtained

by finding the average number of electrons a 4 keV electron can liberate via collisional ionisation, where a simple Rydberg model [143] is used to estimate the ionisation energy of each gold ion. The ionisation energy, U_{ionis}, can be shown to be that in equation 6.1 [144], based on the atomic number, Z, and the quantum level, n_q, that the electron is being ejected from, where R_∞ is Rydberg's constant.

$$U_{ionis} = \frac{Z^2}{n_q^2} hcR_\infty \tag{6.1}$$

Equation 6.1 is known to underestimate the ionisation energy, especially for the lower levels of large Z ions, and so this may vary by up to a factor of two, but with gold having a high atomic mass, the expansion velocity obtained should vary by a small percentage as it is proportional to $\sqrt{Z/m_i}$. This simple method also indicates that the graphite foil will be fully ionised, and so an average charge state of 6 is assumed for graphite.

By using the sound speeds in a self similar expansion, the scale length of the plasma can be estimated with time. These are shown in figure 6.11 for the assumed charge states of the two target materials used in this chapter, and for two different temperatures, which reflect the purely theoretically expected temperature [123], and the typical experimentally measured temperature [122].

As figure 6.11 shows, the density gradients develop in shorter times on graphite foils, it is therefore expected that scale length effects will become important for shorter time delays than for gold foils. And the experimental results in section 6.3.1 have already shown that the maximum proton energy recovery has a very clear target material dependence.

6.4.3 Interaction of a high intensity pulse with target front plasma scale lengths

Particle in cell simulations were performed to investigate the effect of a preplasma scale length on hot electron generation. As multi dimensional effects such as relativistic self focussing, are expected to be significant the simulations were run in two dimensions.

The simulation box spans the coordinates $x = (-30) - 95$ μm, and $y = (-12) - 12\mu$m, with 25 nm resolution in each dimension. A 1.054 μm wavelength laser propagates in the x direction and is set to focus at an intensity of 10^{19} Wcm^{-2} centred on the origin, to a 7 μm full width at half maximum Gaussian spot. The Rayleigh length of the focussing laser is therefore around 50 μm. The laser has a trapezoidal temporal profile, with ramp up and down times of 100 fs, and remains at peak intensity for 500 fs.

A flat target foil is positioned between $x = 0 - 1$ μm, and an exponential preplasma scale length in the negative x direction is present, which is varied between simulations. To reduce computational demands, the target is assumed to be composed of fully ionised hydrogen and the bulk target density is set to 50 n_{crit}. The initial electron temperature is set to 5 keV, and while the cold Debye length of the bulk target is some ten times larger than the grid resolution, the cold Debye length of the preplasma is well resolved, as is that of the hot electron population.

From a computational stand point, having long scale length overdense plasma occupying large regions, is both demanding and wasteful on resources, for simulations that are already pushing the available resource limits, demanding many thousands of core hours to run for around 1 ps. For this reason, the plasma was chosen to have two scale lengths, a fixed scale length of 1 μm from the initial target edge down to critical density, and a second scale length which is varied to match the parameters from section 6.4.2.

With the simulation box being 30 μm long before reaching critical density

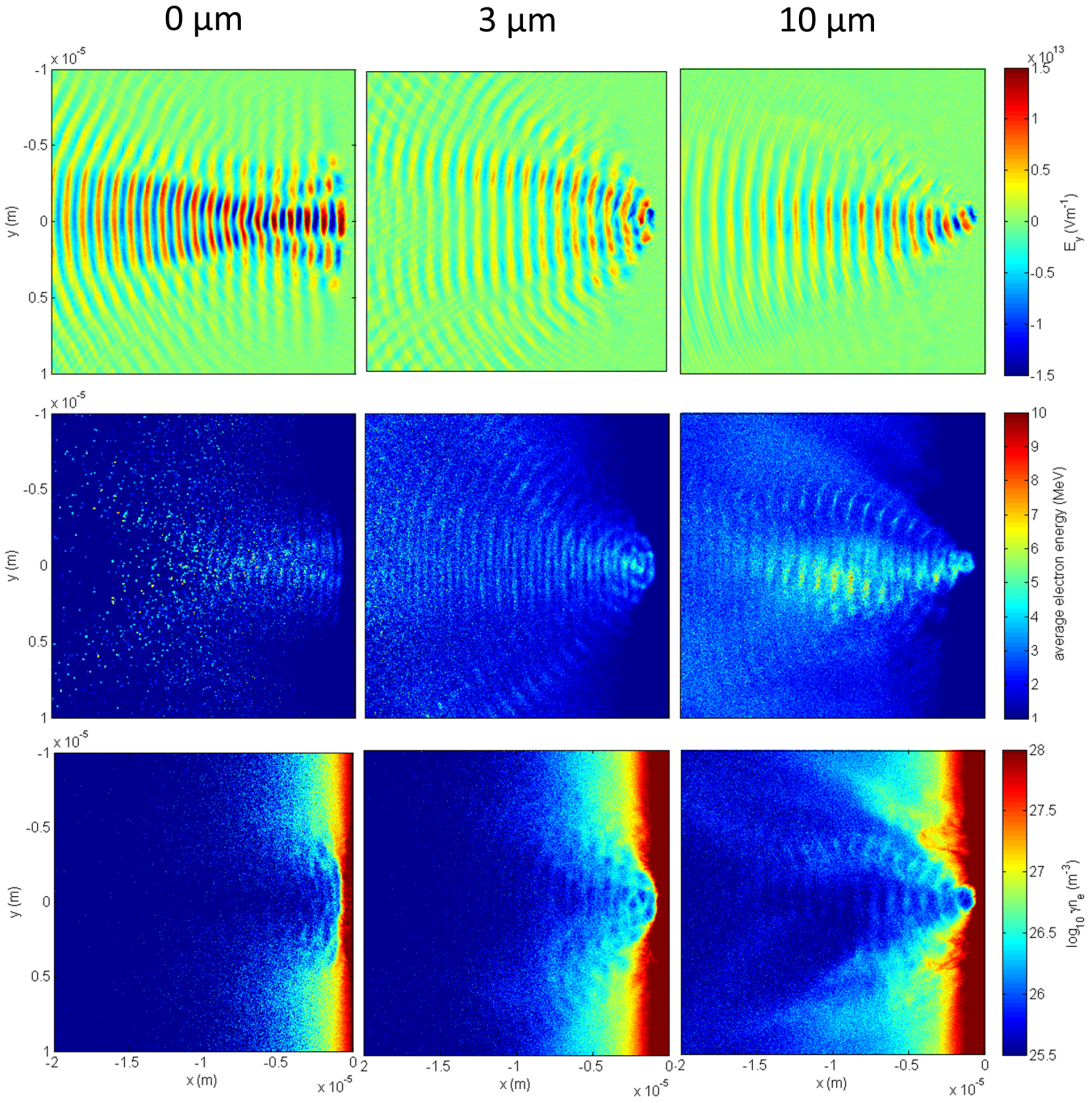

Figure 6.12: The electric field y-component, cell averaged electron energy and cell averaged electron density are presented in each row, for the two dimensional PIC simulations discussed in the text. The figures represent the cases of an initial density gradients of 0 μm (leftmost column), 3 μm (central column) and 10 μm (rightmost column), and are each obtained at 700 fs, where the end of the peak of the pulse is interacting with the overdense region.

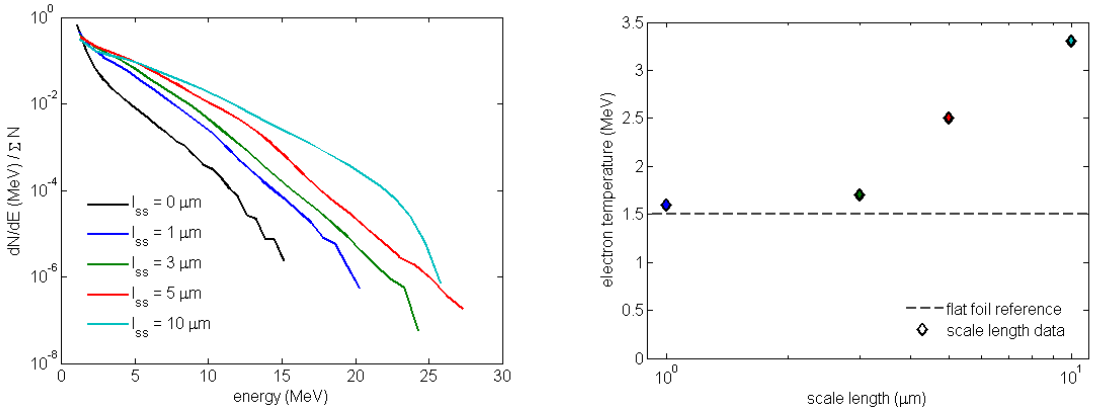

Figure 6.13: (left) The electron spectra in the central full width half maximum region of the pulse at 700 fs. (right) The fitted electron temperature to the spectra.

plasma, the laser power remains below the critical power for self focussing for scale lengths of up to 8 μm, and so the key physics of this interaction should be captured. In the case of the 10 μm scale length preplasma, the beam is injected into preplasma with a power of around twice critical for self focussing.

The main results from the numerical modelling are presented in figure 6.12 which shows laser and preplasma conditions 700 fs into the simulation for three different initial preplasma scale lengths of 0 μm, 3 μm and 10 μm.

In the case of the initial zero scale length case, the electric field of the laser gradually focuses to the position of the critical surface, which can be identified through the relativistically corrected density plots. The electric field transverse profile is distorted from its ideal Gaussian transverse profile, but this is due to interference between the incoming and reflected beam which is modulated by small perturbations in the critical surface.

Measuring the energy content of the reflected beam is not straightforward in this constrained setup. However at this point in time in the simulation, the leftmost portion of the electric field in figure 6.12 is dominated by the reflected beam, which gives some qualitative indication of the reflected energy portion. The cell averaged hot electron temperatures are shown in figure 6.12 and the spectrum over the full width at half maximum laser spot region is given in figure 6.13.

For an initial scale length of 10 μm, the electron density plot shows a depleted

density region in the centre of the pulse path, as the electrons are ponderomotively pushed from higher laser intensity regions. This is shown to cause significant self focussing of the laser as it propagates through the underdense region. The electric field of the pulse is observed to form a considerably tighter focus as it arrives at the critical surface. The nominal 7 μm full width at half maximum spot is focussed to a sub micron spot, giving electrons a larger energy as they are pushed across the critical surface. Note also the relative lack of reflected laser energy, which appears to be more efficiently coupled into the plasma electrons. There is also some evidence of the laser beam beginning to filament as has been observed to take place in longer scale length plasma.

As well as this effect at the critical surface, the electrons of the underdense plasma are also observed to obtain energy as they interact with the focussing laser in the following process consistent with that proposed by *Zheng et al.* [145] as discussed. Energetic electrons are observed to obtain high energies as they are ponderomotively accelerated, and the self generated electric and magnetic fields of the plasma become strong enough to confine the electrons through the Lorentz force to the central high intensity regions of the laser field. This results in high energy and high density electrons bunched at the laser period being carried to the critical surface by the laser acting as a series of potential wells.

In the intermediate case of a 3 μm scale length preplasma some of the preplasma effects observed in the long scale length case become evident. Some degree of self focussing is observed in the preplasma, with hotter electrons also observed than in the flat foil case. This roughly marks the onset of where the preplasma begins to significantly influence the hot electron generation.

The electron spectra from each of the simulations are shown in figure 6.13. This is representative of forward travelling electrons in a box the width of the full width at half maximum of the pulse, and within a few microns from the critical surface. The spectral shapes are different for each of the scale lengths investigated, however a good fit of the form $dN/dE \propto \exp(E/T_e)$ is found for each of the spectra for electron energies in the region of 3-15 MeV, giving the

average electron temperature shown in figure 6.13.

The fitted hot electron temperature is observed to only slightly increase for short scale length preplasma of up to 3 μm, compared to the case of the planar foil, which is itself consistent with the ponderomotive scaling. At scale lengths longer than 3 μm the hot electron temperature is observed to considerably increase to 3.3 MeV for a 10 μm scale length preplasma, which is more than double the temperature obtained from the flat foil. No evidence is found at this scale length of a reduction in electron temperature, which is expected for scale lengths longer than ~ 20 μm, as shown by *Gray* [146].

6.4.4 Effect of target rear plasma scale lengths on ion acceleration

To estimate the effect of a target rear scale length on ion acceleration, the results of *Grismayer and Mora's* model [49] are used, which describes ion acceleration driven by a hot electrons in the presence of an already present rear surface density scale length.

Figures 6.14 and 6.15 show plots of the maximum expected proton energy normalised to the planar foil case, for the five different electron temperatures in section 6.4.3 for the two different target materials. The two figures show slightly different dependence, as the model distinguishes between target thickness. To accommodate the scale lengths required in the case of the gold foil, a slightly thicker target had to be assumed, as the model only takes account of scale lengths up to half the target thickness.

Each plot represents the maximum proton energy expected for a single temperature electron population injected into the target. In the absence of preplasma on the target front, the electron temperature would be unchanged, and therefore the maximum ion energy could only be reduced as the rear scale length increases. However, when the target front scale lengths are taken into account, the maximum proton energy is not confined to a single electron temperature, but can vary according to the preplasma conditions.

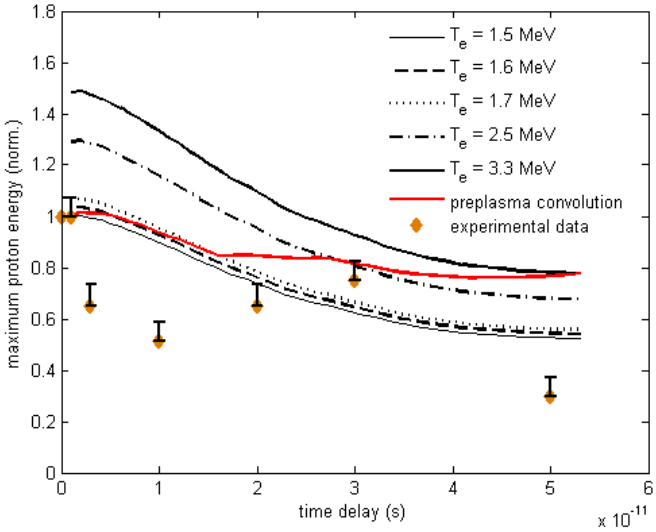

Figure 6.14: The maximum proton energy from TNSA in a rear surface density gradient, obtained for several electron temperatures (black), corresponding to those generated in the target front preplasma in PIC simulations. The expected maximum proton energy, is shown as a red line, with the experimental data for 5 μm gold foils also plotted. Analytical maximum energies are normalised to that obtained for zero scale length. Experimental maximum energies are normalised to those for single pulse interactions.

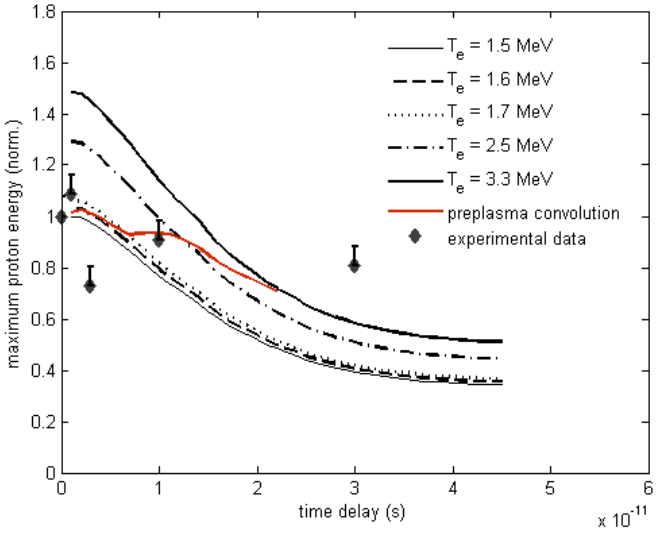

Figure 6.15: As in figure 6.14, but in this figure the modelling and experimental data are for 45 μm graphite foils.

By interpolating an electron temperature generated by the front surface pre-plasma expansion, the maximum proton energy generated by this electron temperature in the expected rear surface gradient is calculated, and the projected maximum proton energy is shown on each figure as a red line.

Some of the global features of the projected maximum proton energies are in agreement with experimental observations. For both target materials, the model predicts that the maximum proton energy initially decreases with an increasing rear surface scale length, because the electron temperature is initially only slightly increased by having larger front surface scale length. Experimentally, the reduction in maximum proton energy is observed to be much larger than is predicted by the model, but some degree of disagreement is expected here. The model is limited to a self similar type expansion, and at short time delay between the pulses, the expansion is dominated by kinetics. For longer time delays, where a self similar expansion assumption becomes valid, the recovered maximum proton energy is more adequately described by the model.

A target material specific maximum proton energy recovery time is also observed in the modelling. The differing sound speeds of the materials ultimately leads to differences in the scale length development from the self similar expansion, and so longer times are required for gold foils to acquire similar density gradients, compared to the graphite foils. The model therefore predicts a $c_s t$ invariance, which accounts for the experimental observations.

Modelling also suggests that the maximum proton energy will plateaux, if a state is reached where the detrimental rear surface scale lengths are only just countered by the increasing electron temperature. This matches experimental observations for both the 25 μm gold and 45 μm graphite foils. Only the 5 μm gold foils disagree with this, and given the spatial intensity distributions of the protons in section 6.3.2, this indicates that shock break out is the sole mechanism responsible for this decrease. This is why the experimental data at 50 ps time delay, does not match the expected trend.

The projected maximum proton energies for graphite foils are not predicted

beyond a time delay of approximately 20 ps in figure 6.15. At this time, the plasma scale lengths exceed the 10 μm scale length for which an electron temperature scaling has been obtained. Additionally, these scale lengths approach the experimental laser spot size, beyond which the assumed one dimensional geometry begins to become strongly violated. It is therefore possible that at long time delays, the three dimensional expansion reduces the growth rate of scale lengths allowing a higher maximum proton energy for longer times.

6.5 Conclusions and discussion

A proof of principle experiment has been presented, which shows for the first time that the maximum proton energy loss associated with long scale length target rear density gradients can be countered by enhanced absorption in long scale length preplasma at the target front surface.

Some of the experimental results strongly indicate that where the scale lengths are developed by the laser in this manner, thinner targets are vulnerable to unknown prepulses in the system. A sufficiently thick target choice, can be used to guard against shock breakout which would otherwise make the effect more difficult to measure.

By assuming a self similar expansion of the bulk target, the scaling of the electron temperature was used, and this electron temperature was approximated to predict the maximum proton energy expected by applying the formulae of *Grismayer and Mora*. The model predicts the general trend of the maximum proton energy, which is reduced at short time delay, before recovering for increasing time delay. It also accounts for this recovery time being target material dependent, and it is shown that this can be accounted for by differing bulk target expansion velocities.

The modelling however, appears to suggest that the effect is more subtle than is observed experimentally, where the proton energies are observed to be reduced more than predicted. There are probably two main sources of uncertainty con-

tributing to this effect. Firstly, the model assumes that the system evolves such that the electrons generated by the second pulse can be treated as a perturbation to the electron population of a quasineutral density scale length on the target rear surface. Clearly this is strongly violated at short time delay between the pulses, and experimental evidence showing that the prepulse seeds an MeV proton population, shows that there is a strong sheath field at early time. The problem at this stage is therefore of two kinetic electron populations, and not a single kinetic electron population. This is difficult to model even in one dimension, solely due to the number of macroparticles required to give adequate resolution of the sheath field behaviour at the long timescales required.

Secondly, the experimental measurement of the integrated proton dose becomes large for long time delay, indicate that the absorbed energy fraction of the laser might be increased in the preplasma scale lengths that develop on these timescales. This is in agreement with the two dimensional particle in cell simulations presented, which show qualitatively that in long scale length preplasma, the reflected energy fraction is very much less than in the steep density gradient case.

While theoretical expansion models do not typically show a strong scaling of proton energy with the number of hot electrons in the sheath, experimental scaling by *Brenner et al.* [124] and *Coury et al.* [147], show very clearly that maximum proton energies can be increased by defocussing the laser and maintaining the intensity. This is independent of the electron temperature, and was later attributed to the number of electrons in the sheath being maintained for longer time [58]. Therefore, an electron conversion efficiency enhancement may contribute to increasing the maximum proton energy at late time, which may account for the marked enhancement measured at late time.

Other two dimensional effects will undoubtedly become important at these late times, and the experimental observation that the maximum proton energies from graphite foils remain around the same at late time could be explained by multi dimensional expansion limiting the scale length development.

These results are of some importance in considering proton driven fast ignition schemes, as they show that if a single pulse laser can deliver a TNSA spectrum with the required conversion efficiency, that scale lengths present on both side of the target does not necessarily render the proton beam unusable, as the maximum proton energy and conversion efficiency can be kept close to the single pulse capability in the presence of long density gradients up to at least tens of microns.

Chapter 7

Summary and future work

As the field of laser driven ion acceleration has developed over the past decade, the initial excitement at the discovery of these unique ion sources has prompted many authors to speculate on the potential applications of these beams to various disciplines. This speculation has been accompanied by critical analyses in the literature from authors both within and outwith the immediate field, which have led to detailed descriptions of the proton beam requirements for many of these applications. A common feature is the need to increase the laser to proton energy conversion efficiency, whether this be for fundamental physics reasons or to make the acceleration method competitive.

As the matter of conversion efficiency is cited as a requirement for many applications to be realised, this is the matter on which this thesis has primarily focussed. This has been both directly, through novel targetry in chapter 5, and the investigation of methods to mitigate known ion acceleration hazards in chapter 6, and indirectly, in investigating the applicability of the plasma mirror for optical control via double pulse interactions, in chapter 4.

A summary of the findings of this thesis, and their context within the field of laser driven ion acceleration follows.

7.1 Plasma mirror lifetime characterisation by temporally controlled double pulse interactions

In chapter 4, the plasma mirror was characterised in the double pulse regime for the first time, where experimental measurements could be used to calculate the individual pulse reflectivities. From this, the probe pulse is found to have a reflected energy fraction of up to 96 % when the pulse separation time is 3 ps, which is significantly higher than the 85 % measured for a single pulse. This result alone warrants some further investigation into this mode of operation for optimising the reflectivity of the plasma mirror. As the reflectivity of the plasma mirror peaks a significant time after the probe pulse is switched off, this was also interpreted to provide some insight into the temporal dynamics of the ionisation mechanisms, which may be useful in any pursuit of reflectivity optimisation.

In addition, the on shot post plasma mirror far field was experimentally recorded, and it was found that this remains of high quality for pulse delays of up to 5 ps, with a significant fraction of the energy being contained in a spot size similar to a single pulse. This is an important result as it leads to the conclusion that the plasma mirror is suitable for delivering the laser spot quality required in double pulse ion acceleration experiments, a conclusion not achievable using only reflected energy fraction measurements.

The plasma mirror is therefore an optical tool appropriate for use in the sub 5 ps time delay regime of double pulse delivery. This is a significant conclusion as it is in this regime that the double pulse is possibly most powerful as a technique for enhancement of conversion efficiency of laser to proton energy.

Double pulses can also be useful for collimation of electron beams [91], which appear to be optimised for time delays in the region of 6 ps, for relatively high prepulse intensities of 10^{19} Wcm^{-2}, which may be close to the limit of the usable plasma mirror lifetime. As it has been shown here that this lifetime is determined

by the plasma expansion of the contaminant layer, removing the contaminant layer should result in the plasma mirror having a longer lifetime as the expansion of the higher inertia heavy ions that make the plasma mirror would be slower.

Removal of this contaminant layer has been of interest for heavy ion acceleration in laser driven ion acceleration studies, and cleaning techniques based on target heating [45, 119] and contaminant layer ablation [148] have been investigated, where significant reduction of the proton number was observed using both techniques. The high temperatures required to completely remove the contaminant layer by heating, however, might lead to destruction of the optical coating of the plasma mirror, and its antireflective properties at low intensity along with this, and so ablation may be the best technique.

7.2 Multi-pulse enhanced laser ion acceleration using plasma half cavity targets

Chapter 5, represents the first experimental investigation of a target design that reuses the significant reflected energy fraction from an ultrahigh intensity laser plasma interaction. By collecting the reflected light in a cavity with a refocussing element, a double pulse type interaction was attained. This interaction was found to enhance the conversion efficiency of laser to proton energy by half whilst preserving the quasi-Maxwellian TNSA spectrum, or by almost double with a large modification to the low energy proton spectrum.

The acceleration mechanism was investigated using PIC simulations which predicted the same order of conversion efficiency improvement as that measured experimentally. The PIC modelling predicts that the mechanism can be optimised by the introduction of the second pulse at a time such that the strong accelerating sheath field is prolonged in time. The PIC modelling also shows that the density scale length of the expansion is important at the time the post pulse introduced such that the enhanced field acts over a large number of protons. The PIC modelling also predicts that the staging of the laser energy delivery is more

efficient for the transfer of laser energy to protons than delivering the same total energy in a single pulse, although this was not experimentally verified.

On investigation of the reflected energy profile of the ultrahigh intensity interaction in Appendix A, the reflected beam is found to be significantly more divergent than the incident beam, going from around $f/10$ incident to $f/2.5$ reflected. This measurement highlights the need for a refocussing element in the cavity design, such that the post pulse retains the high intensity required for it to be effective in accelerating a hot electron population.

7.3 Double pulse ion acceleration in the long time delay regime

In chapter 6 a study is presented of ion acceleration from targets with significant plasma density scale lengths on both sides. Scale lengths on the target rear are known to reduce the maximum proton energy, as they prevent sheath fields from becoming as large as in the sharp density gradient case. However, with target front scale lengths, hotter electron populations can be generated due to the enhanced laser energy absorption and preplasma optical effects enhancing the laser fields through self focussing. When the density gradients reach several microns, hot electron populations in the preplasma are found to efficiently accelerate ion populations from the target rear, even in the presence of similar sized density scale lengths on the rear side of the target.

The result is that after an initial decrease in maximum proton energy and laser to proton energy conversion efficiency for short time delays between pulses, these parameters are observed to be enhanced at longer time delays as these scale lengths develop. The long time delay regime is identified where the proton energy and conversion efficiency in the presence of long scale lengths is similar to that obtained from single pulse interactions, where it may have otherwise have been expected to be non existent.

In absence of experimental measurements, some reports from the literature are

relied upon for estimates, such as bulk target temperature. However these successfully predict a target material dependence of the trends in maximum proton energy.

With these results being of potential importance to a proton driven fast ignition fusion scheme, a dedicated experimental study of the acceleration mechanism is warranted, with the necessary suite of experimental diagnostics to probe the plasma conditions on each face of the target. Measurements of the specific plasma density gradients are needed for the next stage of numerical modelling to replace some of the first estimate assumptions made here, in absence of experimental measurement.

Greater control over the plasma density gradient evolution on both sides of the target via dedicated heating beams would also allow experimental measurements to be made to verify modelling of the enhanced absorption and electron seeding on the target front. This would eliminate the need to rely on analytic or numerical modelling on the target rear, where this becomes impractical and encroaches on violation of the assumed analytic geometry.

Recently, highly efficient proton generation has been observed at the Astra-Gemini laser [149], with proton energies of interest to the fast ignition scheme, in the 3-28 MeV range. With the potential to upgrade this laser to a 10 Hz repetition rate through diode pumping [150], this may be the ideal facility to take this concept further and demonstrate high repetition rate, highly efficient ion acceleration in this regime of interest to fast ignition. High repetition rate targetry exists in the form of tape targets [151], for the necessary target thicknesses, and a defocussed geometry may help with the conversion efficiency scaling [124].

The nature of the proton beam filamentation observed in figures 6.7 and 6.8 with the time delay between the pulses in this experimental work also requires a more detailed experimental investigation with greater control and diagnosis of the plasma conditions. It is not yet clear whether this is an effect due to an instability seeded by the controlled prepulse or with the main pulse interaction with the plasma expansion, and the mechanism for this requires investigation.

This is a particularly important point of interest as the emerging filamentation may place limitations on the potential to focus the proton beam, and with the tens of picoseconds time at which it emerges coinciding with the tens of picoseconds ignition pulse duration it is important to identify the source to ascertain whether this may be a fundamental problem with the ignition pulse requirements.

A dedicated suite of diagnostics would be required to study this, which poses a challenge in itself to probe at the sub micron spatial scales at which a Weibel instability appears to exist according to PIC simulations [136]. However laser driven proton radiography [152] may provide a pathway to probing the field structure and evolution of a Weibel instability [153]. The reflectivity measurements also appear to be a promising approach to making measurements of the critical surface structure, and if a defocussed beam can be used to probe the interaction region, examining the reflected far field of the probe beam may provide a means to measure any periodicity within the structure.

A more exotic approach to diagnosing the small scale structures, is proposed by *Kluge et al.* [154], where the authors have shown how a variety of techniques utilising x-ray free electron lasers may provide means to measure these as the x-ray sources are developed in the future.

7.4 Outlook

The laser driven approach to ion acceleration is already widely recognised as having many inherent unique properties, and are unparalleled in their short bunch lengths, high brightness and laminarity. Adding to this, that many of the necessary beam parameter requirements for laser driven ion acceleration to become a competitive technique are now being experimentally demonstrated, such as beam focussing, spectral control and demands on conversion efficiency, which is central to this thesis, the potential to implement these beams in applications may be imminent.

For many years, the field has demanded higher powered lasers at higher rep-

etition rates, to demonstrate the capabilities of these sources, and now we sit at the precipice of the delivery of such systems within the next few years. These lasers might be capable of efficiently accelerating high energy protons, and could be capable of demonstrating systems that can be used for applications such as hadron therapy or isotope production. Upgrades, in terms of the laser beam parameters, beyond those planned at these facilities therefore may not be required for these applications to be realised. The inevitable march toward upgrading the laser systems further, however, might come with the benefit that these systems on the forefront of today's technology will become miniaturised, as they have in the past. Such progress can only further aid the delivery of the promise of a compact laser driven ion source.

Appendix A: On the specularly reflected energy spatial profile

Laser intensity dependence of the specularly reflected laser energy profile from the high to ultra-high intensity regime

In chapter 5 the concept of a focussing plasma half cavity target was introduced. For this work, the spatial distribution of the specularly reflected laser energy from a single laser pulse interaction is of particular interest. If the specularly reflected laser energy spatial distribution is mostly contained in the nominal focussing cone of the off axis parabola, then a long $f\#$ optic might be suitable to deliver the laser light to a much simpler wedge type target design, which would return the reflected light, but without the need for refocussing. A diffraction limited $f/20$ optic for example could deliver spot sizes similar to those here, and would have a suitable Rayleigh range of more than 500 μm.

To measure the spatial profile, several shots were taken at best focus on gold targets at the PHELIX laser system. The on target energy was varied allowing the intensity to be varied from $10^{15} - 10^{19}$ Wcm^{-2} with a nanosecond intensity contrast ratio of around 10^6. The beam is s-polarised and is delivered at a 45° angle of incidence, by an $f/9$ off axis focussing parabola. The simple experimental geometry, shown in figure 8.1 shows that the specularly reflected energy from the interaction is diverted to a polytetrafluoroethylene scatter screen, and the

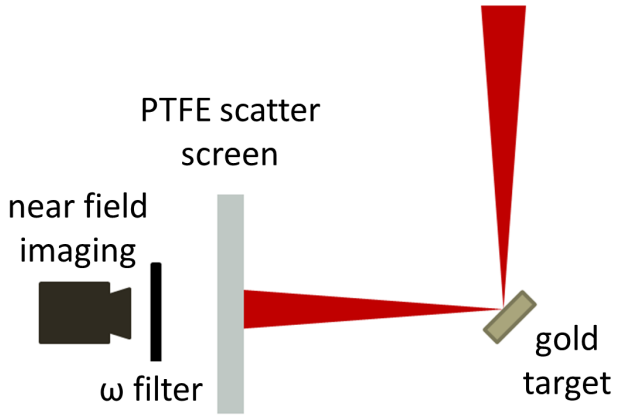

Figure 8.1: Schematic of experimental layout for reflected beam spatial profile measurements

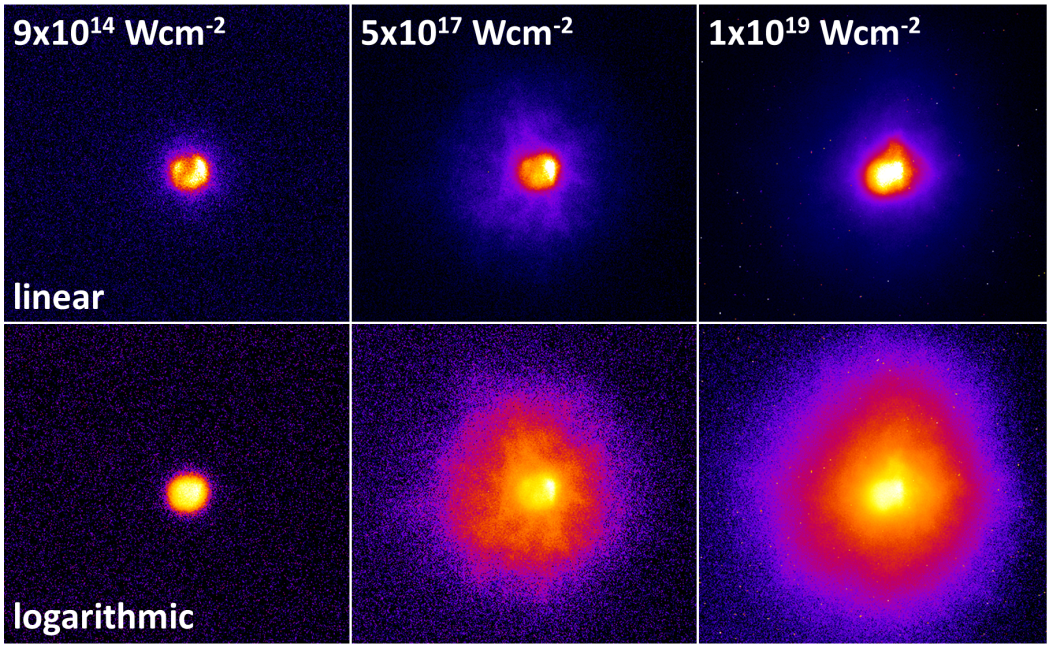

Figure 8.2: The reflected spatial intensity distributions for three shots across the intensity range scan. A linear scale and logarithmic scale are presented, which shows a significant fraction of the beam being scattered from the centre.

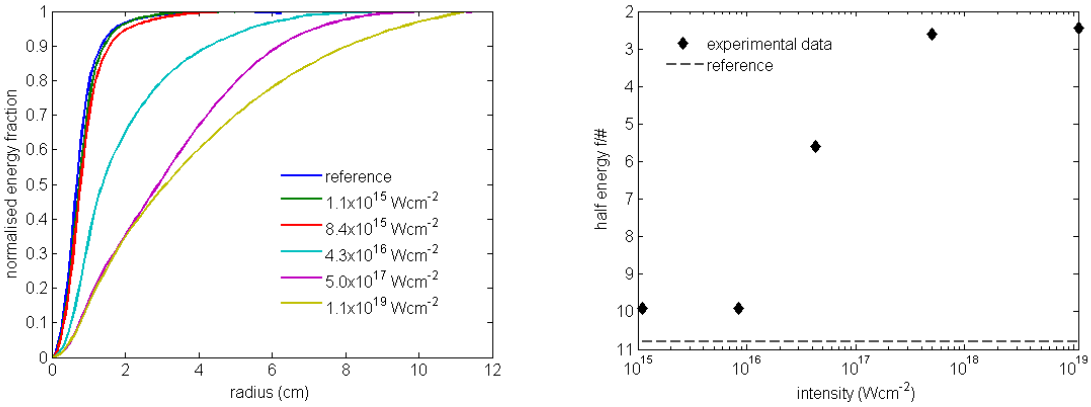

Figure 8.3: (left) The normalised radial integrals for a series of shots at the labelled intensities. A reference shot is also indicated which corresponds to the alignment beam being reflected from the gold target and is the reflection from gold as opposed to gold plasma. (right) The reflected beam half energy $f/\#$ versus intensity

spatial profile of the fundamental frequency reflected laser energy is captured by a triggered CCD.

Some of the reflected spatial intensity distributions are given in figure 8.2. These show that the reflection of the lower intensity laser to be reasonably well described as sharing the top hat transverse profile and $f\#$ of the pre-interaction beam delivered to the chamber. However, as the incident beam becomes higher in intensity the profile deviates considerably from the top-hat distribution and more energy is thrown into the wings of the beam as the interaction intensity increases. This is reflected in the radial integrals of the beams, presented in figure 8.3, which is in turn used to find the radius of the beam containing half the total energy. This shows that the half energy $f/\#$ of the beam is increased from an $f/10$ beam at lower intensity, to an $f/2.5$ at the highest intensities. It should be noted that the half energy $f/\#$ definition used accounts for discrepancy in $f/\#$ reported and the true $f/\#$ of the focussing parabola used. This result justifies the use of the refocussing element of the cavity targets in chapter 5.

The most likely explanation of the specularly reflected laser energy profile change over intensity is the phenomenon discovered by *Schumacher et al.* in PIC simulations [155]. Here it was found that the presence of a preplasma resulted

in self focussing of the laser, which had the effect of perturbing the relativistic critical surface into a concave profile, where the surface was deformed to a greater extent for longer scale lengths. This results in the reflected beam being scattered over a wider angle. *Schumacher* noted that the most intense parts of the beam deformed the critical surface, while the less intense part on the periphery did not, it is therefore the most intense part of the beam that is scattered to larger angles. The mechanism therefore requires both a preplasma and the laser to have sufficient power to self focus.

In the experimental results here, a $\sim 6\times10^{15}$ Wcm^{-2} pulse reaches the critical power for self focussing at the critical density. While the $\sim 8\times10^{15}$ Wcm^{-2} data shot meets the condition for self focussing, it is unlikely to have an appreciable scale of preplasma to propagate in, owing to the contrast of the laser. However, as the intensities increase above this, the experimental data indicates that enough preplasma has formed for self focussing to cause deformation of the relativistic critical surface. This explains the observed switch on of the effect, and with more energy being observed to be in the wings, this is also consistent with the larger perturbations to the relativistic critical surface expected from higher intensity pulses.

Picosecond temporal resolution of the specularly reflected laser energy profile from high intensity interactions

Chapter 4 showed that critical surface density gradients become large enough to distort the reflected wavefront of the probe beam as the plasma expansion time exceeds 5 ps. As well as the far field information that is presented in this chapter, the quasi near field intensity distribution was recorded from a glass scatter screen, shown on the experimental schematic, figure 4.1. The images taken of the quasi near field for the series of time delays, are presented in figure 8.4.

As the specularly reflected light at the fundamental frequency comes from the critical surface, it retains some information on the density gradients there in its angular profile, and it is clear that for longer time delays between the pulses, the quasi near field intensity distribution shifts from a locally smooth distribution to one which becomes increasingly speckled with increasing time. Only the preplasma conditions and critical surface shape will vary in this time, and given the close qualitative correlation with the near field quality becoming degraded at times similar to when the far field quality is degraded, it is reasonable to assume that the speckled pattern observed in the quasi near field gives at least some information on the critical surface density gradients, given that these gradients in turn could be used to explain the loss of far field quality in chapter 4.

Further investigation into how this pattern could be used as a diagnostic to measure critical surface gradients is warranted, as it is unclear exactly how this data could reliably be deconvolved to give information on the real critical surface density gradients, but for the moment at the least, they offer a qualitative insight into the conditions at the critical surface.

The images in figure 8.4, presents an opportunity to briefly consider the light collection of the system in figure 4.1. The limiting component in terms of light collection of the far field imaging and calorimetry system is the spherical mirror

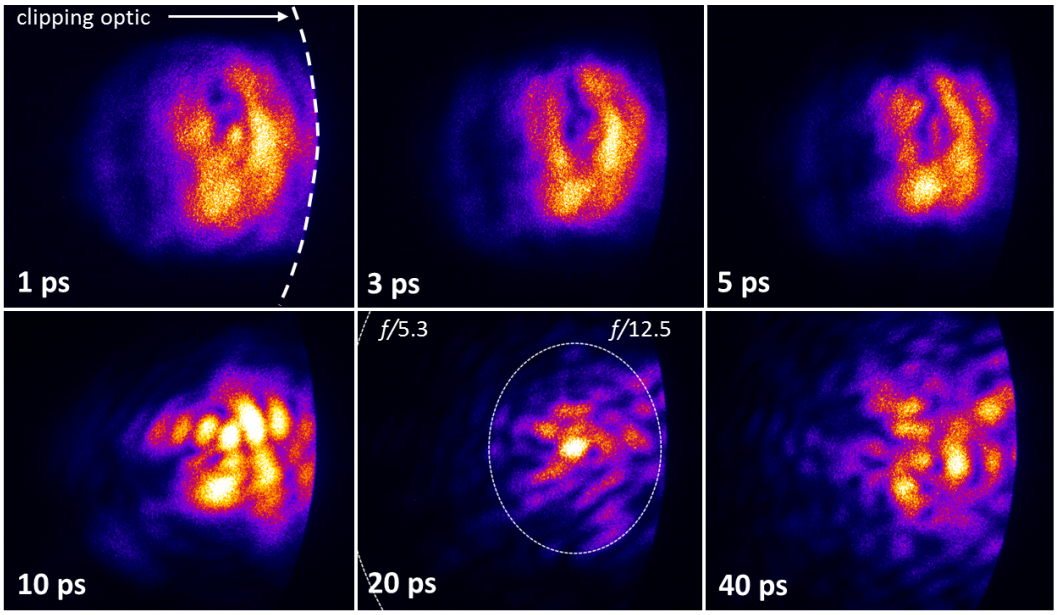

Figure 8.4: The near field intensity distribution for double pulse shots on the plasma mirror ranging from $\delta\tau$ 1 ps to 40 ps, collected on the glass scatter screen in figure 4.1. On the image of the 20 ps delay two ellipses are drawn corresponding to the nominal $f/\#$ of the specularly reflected beam and the collection aperture of the spherical mirror, which are discussed in the text. The distribution appears elliptical due to the scatter screen being at an angle to the incoming light, and the hard edge on the right hand side of each image is due to the transmitted light clipping the mount that houses the wedge. The near field imaging was filtered to image only the fundamental laser frequency.

aperture, which subtends an $f/5.3$ collection cone, and on the image corresponding to the 20 ps ionisation probe pulse delay a dotted line represents this aperture, and the nominal $f/12.5$ cone of the specularly reflected beam. In even the most extreme case, where most energy is reflected into the wings of the image, in the case of a 40 ps delay, it is estimated that less than 1 % of the total specularly reflected light lies outwith the $f/5.3$ collection aperture. For this reason, this is expected to be the maximum error associated with the calorimetry measurements of chapter 4, which were used to calculate the specularly reflected energy fraction from the plasma mirror interactions.

References

[1] E Rutherford. Address of the president, Sir Ernest Rutherford, OM, at the anniversary meeting, November 30, 1927. *Proceedings of the Royal Society of London. Series A*, 117(777):300, 1928.

[2] MH Key. Highlights of laser fusion related research by United Kingdom universities using the SERC Central Laser Facility at the Rutherford Appleton Laboratory. *Nuclear fusion*, 25(9):1351, 1985.

[3] WI Linlor. Ion energies produced by giant laser pulse. *Applied physics letters*, 3, 1963.

[4] CE Cook. Pulse compression-key to more efficient radar transmission. *Proceedings of the institute of radio engineers*, 48(3):310, 1960.

[5] D Strickland and G Mourou. Compression of amplified chirped optical pulses. *Optics communications*, 55(6):447, 1985.

[6] J-P Chambaret, O Chekhlov, G Cheriaux, J Collier, R Dabu, P Dombi, AM Dunne, K Ertel, P Georges, J Hebling, J Hein, C Hernandez-Gomez, C Hooker, S Karsch, G Korn, F Krausz, C Le Blanc, Z Major, F Mathieu, T Metzger, G Mourou, P Nickles, K Osvay, B Rus, W Sandner, G Szabo, D Ursescu, and K Varju. Extreme light infrastructure: laser architecture and major challenges. In *SPIE Photonics Europe*, page 77211D. International Society for Optics and Photonics, 2010.

[7] SV Bulanov, TZ Esirkepov, VS Khoroshkov, AV Kuznetsov, and F Pego-

raro. Oncological hadrontherapy with laser ion accelerators. *Physics letters A*, 299(2):240, 2002.

[8] U Linz and J Alonso. What will it take for laser driven proton accelerators to be applied to tumor therapy? *Physical review special topics-accelerators and beams*, 10(9):094801, 2007.

[9] KWD Ledingham, P McKenna, T McCanny, S Shimizu, JM Yang, L Robson, J Zweit, JM Gillies, J Bailey, GN Chimon, RJ Clarke, D Neely, PA Norreys, JL Collier, RP Singhai, MS Wei, SPD Mangles, P Nilson, K Krushelnick, and M Zepf. High power laser production of short-lived isotopes for positron emission tomography. *Journal of physics D: Applied physics*, 37(16):2341, 2004.

[10] M Roth, TE Cowan, MH Key, SP Hatchett, C Brown, W Fountain, J Johnson, DM Pennington, RA Snavely, SC Wilks, K Yasuike, H Ruhl, F Pegoraro, SV Bulanov, EM Campbell, MD Perry, and H Powell. Fast ignition by intense laser-accelerated proton beams. *Physical review letters*, 86(3):436, 2001.

[11] JC Fernández, BJ Albright, FN Beg, ME Foord, BM Hegelich, JJ Honrubia, M Roth, RB Stephens, and L Yin. Fast ignition with laser-driven proton and ion beams. *Nuclear fusion*, 54(5):054006, 2014.

[12] M Roth, D Jung, K Falk, N Guler, O Deppert, M Devlin, A Favalli, J Fernandez, D Gautier, M Geissel, R Haight, CE Hamilton, BM Hegelich, RP Johnson, F Merrill, G Schaumann, K Schoenberg, M Schollmeier, T Shimada, T Taddeucci, JL Tybo, F Wagner, and SA Wender. Bright laser-driven neutron source based on the relativistic transparency of solids. *Physical review letters*, 110(4):044802, 2013.

[13] M Borghesi, J Fuchs, SV Bulanov, AJ Mackinnon, PK Patel, and M Roth. Fast ion generation by high-intensity laser irradiation of solid targets and applications. *Fusion science and technology*, 49(3):412, 2006.

[14] PK Patel, AJ MacKinnon, MH Key, TE Cowan, ME Foord, M Allen, DF Price, H Ruhl, PT Springer, and R Stephens. Isochoric heating of solid-density matter with an ultrafast proton beam. *Physical review letters*, 91(12):125004, 2003.

[15] L Romagnani, J Fuchs, M Borghesi, P Antici, P Audebert, F Ceccherini, T Cowan, T Grismayer, S Kar, A Macchi, P Mora, G Pretzler, A Schiavi, T Toncian, and O Willi. Dynamics of electric fields driving the laser acceleration of multi-MeV protons. *Physical review letters*, 95(19):195001, 2005.

[16] H Daido, M Nishiuchi, and AS Pirozhkov. Review of laser-driven ion sources and their applications. *Reports on progress in physics*, 75(5):056401, 2012.

[17] U Masood, M Bussmann, TE Cowan, W Enghardt, L Karsch, F Kroll, U Schramm, and J Pawelke. A compact solution for ion beam therapy with laser accelerated protons. *Applied physics B*, 117:41, 2014.

[18] K Harres, I Alber, A Tauschwitz, V Bagnoud, H Daido, M Günther, F Nürnberg, A Otten, M Schollmeier, J Schütrumpf, M Tampo, and M Roth. Beam collimation and transport of quasineutral laser-accelerated protons by a solenoid field. *Physics of plasmas*, 17(2):023107, 2010.

[19] SN Chen, M Gauthier, DP Higginson, S Dorard, F Mangia, R Riquier, S Atzeni, J-R Marquès, and J Fuchs. Monochromatic short pulse laser produced ion beam using a compact passive magnetic device. *Review of scientific instruments*, 85(4):043504, 2014.

[20] R Orecchia, P Fossati, and S Rossi. The national center for oncological hadron therapy: status of the project and future clinical use of the facility. *Tumori*, 95(2):169, 2009.

[21] RJ Clarke, S Dorkings, D Neely, and I Musgrave. The production of patient dose level 99mTc medical radioisotope using laser-driven proton beams. *SPIE Optics + Optoelectronics*, page 87791C, 2013.

[22] M Madsen. Into eternity. Films Transit International, 2010.

[23] S Atzeni and J Meyer-ter Vehn. *The Physics of Inertial Fusion: Beam Plasma Interaction, Hydrodynamics, Hot Dense Matter*. Oxford University Press, 2004.

[24] OA Hurricane, DA Callahan, DT Casey, PM Celliers, C Cerjan, EL Dewald, TR Dittrich, T Döppner, DE Hinkel, LF Berzak Hopkins, JL Kline, S Le Pape, T Ma, AG MacPhee, JL Milovich, A Pak, HS Park, PK Patel, BA Remington, JD Salmonson, PT Springer, and R Tommasini. Fuel gain exceeding unity in an inertially confined fusion implosion. *Nature*, 506:343, 2014.

[25] M Tabak, J Hammer, ME Glinsky, WL Kruer, SC Wilks, J Woodworth, EM Campbell, MD Perry, and RJ Mason. Ignition and high gain with ultrapowerful lasers. *Physics of plasmas*, 1(5):1626, 1994.

[26] DS Clark and M Tabak. A self-similar isochoric implosion for fast ignition. *Nuclear Fusion*, 47(9):1147, 2007.

[27] A Einstein. Über einen die erzeugung und verwandlung des lichtes betreffenden heuristischen gesichtspunkt (Concerning an heuristic point of view toward the emission and transformation of light). *Annalen der physik*, 322(6):132, 1905.

[28] A Gold and HB Bebb. Theory of multiphoton ionization. *Physical review letters*, 14(3):60, 1965.

[29] P Gibbon. *Short pulse laser interactions with matter*. Imperial College Press London, 2005.

[30] LV Keldysh. Ionization in the field of a strong electromagnetic wave. *Soviet physics journal of experimental and theoretical physics*, 20(5):1307, 1965.

[31] P McKenna, D Neely, R Bingham, and D Jaroszynski. *Laser-Plasma Interactions and Applications.* Springer, 2013.

[32] SC Wilks, WL Kruer, M Tabak, and AB Langdon. Absorption of ultra-intense laser pulses. *Physical review letters*, 69(9):1383, 1992.

[33] SC Wilks and WL Kruer. Absorption of ultrashort, ultra-intense laser light by solids and overdense plasmas. *Journal of quantum electronics*, 33(11):1954, 1997.

[34] JR Davies. Laser absorption by overdense plasmas in the relativistic regime. *Plasma physics and controlled fusion*, 51(1):014006, 2009.

[35] NG Denisov. On a singularity of the field of an electromagnetic wave propagated in an inhomogeneous plasma. *Soviet physics JETP-USSR*, 4(4):544, 1957.

[36] F Brunel. Not-so-resonant, resonant absorption. *Physical review letters*, 59(1):52, 1987.

[37] P Gibon and AR Bell. Collisionless absorption in sharp-edged plasmas. *Physical review letters*, 68(10):1535, 1992.

[38] WL Kruer and K Estabrook. J×B heating by very intense laser light. *Physics of fluids*, 28(1):430, 1985.

[39] Y Ping, R Shepherd, BF Lasinski, M Tabak, H Chen, HK Chung, KB Fournier, SB Hansen, A Kemp, DA Liedahl, K Widmann, SC Wilks, W Rozmus, and M Sherlock. Absorption of short laser pulses on solid targets in the ultrarelativistic regime. *Physical review letters*, 100(8):085004, 2008.

[40] RJ Gray, XH Yuan, DC Carroll, CM Brenner, M Coury, MN Quinn, O Tresca, B Zielbauer, B Aurand, V Bagnoud, J Fils, T Kuhl, XX Lin, C Li, YT Li, M Roth, D Neely, and P McKenna. Surface transport of energetic electrons in intense picosecond laser-foil interactions. *Applied physics letters*, 99(17):171502, 2011.

[41] DC Barnes, T Kurki-Suonio, and T Tajima. Laser self-trapping for the plasma fiber accelerator. *Transactions on plasma science*, 15(2):154, 1987.

[42] D Jung. *Ion acceleration from relativistic laser nano-target interaction*. PhD thesis, Ludwig Maximilians Universität, 2012.

[43] EL Clark, K Krushelnick, JR Davies, M Zepf, M Tatarakis, FN Beg, A Machacek, PA Norreys, MIK Santala, I Watts, and AE Dangor. Measurements of energetic proton transport through magnetized plasma from intense laser interactions with solids. *Physical review letters*, 84(4):670, 2000.

[44] RA Snavely, MH Key, SP Hatchett, TE Cowan, M Roth, TW Phillips, MA Stoyer, EA Henry, TC Sangster, MS Singh, SC Wilks, A MacKinnon, A Offenberger, DM Pennington, K Yasuike, AB Langdon, BF Lasinski, J Johnson, MD Perry, and EM Campbell. Intense high-energy proton beams from petawatt-laser irradiation of solids. *Physical review letters*, 85(14):2945, 2000.

[45] M Hegelich, S Karsch, G Pretzler, D Habs, K Witte, W Guenther, M Allen, A Blazevic, J Fuchs, JC Gauthier, M Geissel, PT Audebert, Cowan, and M Roth. MeV ion jets from short-pulse-laser interaction with thin foils. *Physical review letters*, 89(8):085002, 2002.

[46] P Mora. Plasma expansion into a vacuum. *Physical review letters*, 90(18):185002, 2003.

[47] P Mora. Thin-foil expansion into a vacuum. *Physical review E*, 72(5):056401, 2005.

[48] J Fuchs, P Antici, E D'Humières, E Lefebvre, M Borghesi, E Brambrink, CA Cecchetti, M Kaluza, V Malka, M Manclossi, S Meyroneinc, P Mora, J Schreiber, T Toncian, H Pépin, and P Audebert. Laser-driven proton scaling laws and new paths towards energy increase. *Nature physics*, 2(1):48, 2005.

[49] T Grismayer and P Mora. Influence of a finite initial ion density gradient on plasma expansion into a vacuum. *Physics of plasmas*, 13(3):032103, 2006.

[50] J Fuchs, CA Cecchetti, M Borghesi, T Grismayer, E D'Humières, P Antici, S Atzeni, P Mora, A Pipahl, L Romagnani, A Schiavi, Y Sentoku, T Toncian, P Audebert, and O Willi. Laser-foil acceleration of high-energy protons in small-scale plasma gradients. *Physical review letters*, 99(1):015002, 2007.

[51] T Matsuoka, S Reed, C McGuffey, SS Bulanov, F Dollar, L Willingale, V Chvykov, G Kalinchenko, A Brantov, V Yu Bychenkov, P Rousseau, V Yanovsky, DW Litzenberg, K Krushelnick, and A Maksimchuk. Energetic electron and ion generation from interactions of intense laser pulses with laser machined conical targets. *Nuclear fusion*, 50(5):055006, 2010.

[52] O Tresca, DC Carroll, XH Yuan, B Aurand, V Bagnoud, CM Brenner, M Coury, J Fils, RJ Gray, T Kühl, C Li, YT Li, XX Lin, MN Quinn, RG Evans, B Zielbauer, M Roth, D Neely, and P McKenna. Controlling the properties of ultraintense laser–proton sources using transverse refluxing of hot electrons in shaped mass-limited targets. *Plasma physics and controlled fusion*, 53(10):105008, 2011.

[53] D Neely, P Foster, APL Robinson, F Lindau, O Lundh, A Persson, CG Wahlström, and P McKenna. Enhanced proton beams from ultrathin targets driven by high contrast laser pulses. *Applied physics letters*, 89(2):021502, 2006.

[54] DC Carroll. *Laser-driven ion acceleration: Source optimisation and optical control*. PhD thesis, University of Strathclyde, 2008.

[55] P McKenna, DC Carroll, O Lundh, F Nürnberg, K Markey, S Bandyopadhyay, D Batani, RG Evans, R Jafer, S Kar, D Neely, D Pepler, MN Quinn, R Redaelli, M Roth, CG Wahlström, XH Yuan, and M Zepf. Effects of

front surface plasma expansion on proton acceleration in ultraintense laser irradiation of foil targets. *Laser and particle beams*, 26(4):591, 2008.

[56] APL Robinson, D Neely, P McKenna, and RG Evans. Spectral control in proton acceleration with multiple laser pulses. *Plasma physics and controlled fusion*, 49(4):373, 2007.

[57] K Markey, P McKenna, CM Brenner, DC Carroll, M. M. Günther, K Harres, S Kar, K Lancaster, F Nürnberg, MN Quinn, APL Robinson, M Roth, M Zepf, and D Neely. Spectral enhancement in the double pulse regime of laser proton acceleration. *Physical review letters*, 105(19):195008, 2010.

[58] CM Brenner. *Laser-driven proton beams: Mechanisms for spectral control and efficiency enhancement*. PhD thesis, University of Strathclyde, 2012.

[59] CM Brenner, APL Robinson, K Markey, RHH Scott, RJ Gray, M Rosinski, O Deppert, J Badziak, D Batani, JR Davies, SM Hassan, KL Lancaster, K Li, IO Musgrave, PA Norreys, J Pasley, M Roth, HP Schlenvoigt, C Spindloe, M Tatarakis, T Winstone, J Wolowski, D Wyatt, P McKenna, and D Neely. High energy conversion efficiency in laser-proton acceleration by controlling laser-energy deposition onto thin foil targets. *Applied physics letters*, 104(8):081123, 2014.

[60] T Esirkepov, M Borghesi, SV Bulanov, G Mourou, and T Tajima. Highly efficient relativistic-ion generation in the laser-piston regime. *Physical review letters*, 92(17):175003, 2004.

[61] APL Robinson, M Zepf, S Kar, RG Evans, and C Bellei. Radiation pressure acceleration of thin foils with circularly polarized laser pulses. *New journal of physics*, 10(1):013021, 2008.

[62] A Henig, S Steinke, M Schnürer, T Sokollik, R Hörlein, D Kiefer, D Jung, J Schreiber, BM Hegelich, XQ Yan, J Meyer-ter Vehn, T Tajima, PV Nickles, W Sandner, and D Habs. Radiation-pressure acceleration of ion

beams driven by circularly polarized laser pulses. *Physical review letters*, 103(24):245003, 2009.

[63] S Kar, KF Kakolee, B Qiao, A Macchi, M Cerchez, D Doria, M Geissler, P McKenna, D Neely, J Osterholz, R Prasad, K Quinn, B Ramakrishna, G Sarri, O Willi, XH Yuan, M Zepf, and M Borghesi. Ion acceleration in multispecies targets driven by intense laser radiation pressure. *Physical review letters*, 109(18):185006, 2012.

[64] LO Silva, M Marti, JR Davies, RA Fonseca, C Ren, FS Tsung, and WB Mori. Proton shock acceleration in laser-plasma interactions. *Physical review letters*, 92(1):015002, 2004.

[65] APL Robinson, P Gibbon, M Zepf, S Kar, RG Evans, and C Bellei. Relativistically correct hole-boring and ion acceleration by circularly polarized laser pulses. *Plasma physics and controlled fusion*, 51(2):024004, 2009.

[66] CAJ Palmer, NP Dover, I Pogorelsky, M Babzien, GI Dudnikova, M Ispiriyan, MN Polyanskiy, J Schreiber, P Shkolnikov, V Yakimenko, and Z Najmudin. Monoenergetic proton beams accelerated by a radiation pressure driven shock. *Physical review letters*, 106(1):014801, 2011.

[67] RA Cairns. *Laser-plasma Interactions: Proceedings of the twentieth Scottish universities summer school in physics, St. Andrews, August 1979. (High-power pulsed lasers, JF Holzrichter).* Taylor & Francis, 1980.

[68] VV Ivanov, A Maksimchuk, and G Mourou. Amplified spontaneous emission in a Ti:sapphire regenerative amplifier. *Applied optics*, 42(36):7231, 2003.

[69] C Hooker, Y Tang, O Chekhlov, J Collier, E Divall, K Ertel, S Hawkes, B Parry, and PP Rajeev. Improving coherent contrast of petawatt laser pulses. *Optics express*, 19(3):2193, 2011.

[70] V Bagnoud, B Aurand, A Blazevic, S Borneis, C Bruske, B Ecker, U Eisenbarth, J Fils, A Frank, E Gaul, S Goette, C Haefner, T Hahn, K Harres, HM Heuck, D Hochhaus, DHH Hoffmann, D Javorkova, HJ Kluge, T Kuehl, S Kunzer, M Kreutz, T Merz-Mantwill, P Neumayer, E Onkels, D Reemts, O Rosmej, M Roth, T Stoehlker, A Tauschwitz, B Zielbauer, D Zimmer, and K Witte. Commissioning and early experiments of the PHELIX facility. *Applied physics B*, 100(1):137, 2010.

[71] G Cerullo and S De Silvestri. Ultrafast optical parametric amplifiers. *Review of scientific instruments*, 74(1):1, 2003.

[72] F Wagner, CP João, J Fils, T Gottschall, J Hein, J Körner, J Limpert, M Roth, T Stöhlker, and V Bagnoud. Temporal contrast control at the PHELIX petawatt laser facility by means of tunable sub-picosecond optical parametric amplification. *Applied physics B*, 116(2):429, 2013.

[73] V Bagnoud. Phelix laser system. `http://www.gsi.de/phelix`, March 2014.

[74] A Dubietis, R Butkus, and AP Piskarskas. Trends in chirped pulse optical parametric amplification. *Journal of selected topics in quantum electronics*, 12(2):163, 2006.

[75] IN Ross, P Matousek, M Towrie, AJ Langley, and JL Collier. The prospects for ultrashort pulse duration and ultrahigh intensity using optical parametric chirped pulse amplifiers. *Optics Communications*, 144(1):125, 1997.

[76] J Ziegler, MD Ziegler, and JP Biersack. SRIM–the stopping and range of ions in matter. *Nuclear instruments and methods in physics research section B: Beam interactions with materials and atoms*, 268(11):1818, 2010.

[77] MC Saylor, TT Tamargo, WL McLaughlin, HM Khan, DF Lewis, and RD Schenfele. A thin film recording medium for use in food irradiation. *International Journal of Radiation Applications and Instrumentation. Part C. Radiation Physics and Chemistry*, 31(4):529, 1988.

[78] MA Stevens, JR Turner, RP Hugtenburg, and PH Butler. High-resolution dosimetry using radiochromic film and a document scanner. *Physics in medicine and biology*, 41(11):2357, 1996.

[79] O Ettlinger, JS Green, S Green, D Parker, and D Neely. A comparison of different radiochromic film types. *Central laser facility annual report*, 2012.

[80] F Nürnberg, M Schollmeier, E Brambrink, A Blažević, DC Carroll, K Flippo, DC Gautier, M Geißel, K Harres, BM Hegelich, O Lundh, K Markey, P McKenna, D Neely, J Schreiber, and M Roth. Radiochromic film imaging spectroscopy of laser-accelerated proton beams. *Review of scientific instruments*, 80(3):033301, 2009.

[81] PR Bolton, M Borghesi, CM Brenner, DC Carroll, CD Martinis, A Flacco, V Floquet, J Fuchs, P Gallegos, D Giove, JS Green, S Green, B Jones, D Kirby, P McKenna, D Neely, F Nuesslin, R Prasad, S Reinhardt, M Roth, U Schramm, GG Scott, S Ter-Avetisyan, M Tolley, G Turchetti, and JJ Wilkens. Instrumentation for diagnostics and control of laser-accelerated proton (ion) beams. *Physica medica*, 30(3):255, 2014.

[82] DC Carroll, P Brummitt, D Neely, F Lindau, O Lundh, CG Wahlström, and P McKenna. A modified thomson parabola spectrometer for high resolution multi-MeV ion measurements Application to laser-driven ion acceleration. *Nuclear instruments and methods in physics reseach section A*, 620(1):23, 2010.

[83] C Ziener, PS Foster, EJ Divall, CJ Hooker, MHR Hutchinson, AJ Langley, and D Neely. Specular reflectivity of plasma mirrors as a function of intensity, pulse duration, and angle of incidence. *Journal of applied physics*, 93(1):768, 2003.

[84] G Doumy, F Quéré, O Gobert, M Perdrix, P Martin, P Audebert, JC Gauthier, JP Geindre, and T Wittman. Complete characterization of a plasma

mirror for the production of high-contrast ultraintense laser pulses. *Physical review E*, 69(2):026402, 2004.

[85] B Dromey, P Foster, S Kar, and M Zepf. The plasma mirror A sub-picosecond optical switch for ultrahigh power lasers. *Review of scientific instruments*, 75(3):645, 2004.

[86] Y Nomura, L Veisz, K Schmid, T Wittmann, J Wild, and F Krausz. Time-resolved reflectivity measurements on a plasma mirror with few-cycle laser pulses. *New journal of physics*, 9(1):9, 2007.

[87] Y Nomura. *Temporal characterization of harmonic radiation generated by intense laser-plasma interaction*. PhD thesis, Max Planck Institut für Quantenoptik, 2008.

[88] T Arber. EPOCH: Extendable PIC Open Collaboration. `http://ccpforge.cse.rl.ac.uk/gf/project/epoch/`, March 2014.

[89] CK Birdsall and AB Langdon. *Plasma physics via computer simulation*. Adam Hilger, 1975.

[90] GG Scott, V Bagnoud, C Brabetz, RJ Clarke, JS Green, RI Heathcote, HW Powell, B Zielbauer, TD Arber, P McKenna, and D Neely. Optimisation of plasma mirror reflectivity and optical quality using double laser pulses. *New journal of physics*, 17(3):033027, 2015.

[91] GG Scott, JS Green, V Bagnoud, C Brabetz, CM Brenner, DC Carroll, DA MacLellan, APL Robinson, M Roth, C Spindloe, F Wagner, B Zielbauer, P McKenna, and D Neely. Multi-pulse enhanced laser ion acceleration using plasma half cavity targets. *Applied physics letters*, 101(2):204101, 2012.

[92] APL Robinson, M Sherlock, and PA Norreys. Artificial collimation of fast-electron beams with two laser pulses. *Physical review letters*, 100(2):025002, 2008.

[93] PA Norreys, RHH Scott, KL Lancaster, JS Green, APL Robinson, M Sherlock, RG Evans, MG Haines, S Kar, M Zepf, MH Key, J King, T Ma, T Yabuuchi, MS Wei, FN Beg, P Nilson, W Theobald, RB Stephens, J Valente, JR Davies, K Takeda, H Azechi, M Nakatsutsumi, T Tanimoto, R Kodama, and KA Tanaka. Recent fast electron energy transport experiments relevant to fast ignition inertial fusion. *Nuclear fusion*, 49(10):104023, 2009.

[94] RHH Scott, C Beaucourt, H-P Schlenvoigt, K Markey, KL Lancaster, CP Ridgers, CM Brenner, J Pasley, RJ Gray, IO Musgrave, APL Robinson, K Li, MM Notley, JR Davies, SD Baton, JJ Santos, JL Feugeas, P Nicolaï, G Malka, VT Tikhonchuk, McKenna P, D Neely, SJ Rose, and PA Norreys. Controlling fast-electron-beam divergence using two laser pulses. *Physical review letters*, 109(1):015001, 2012.

[95] W Yu, L Cao, MY Yu, H Cai, H Xu, X Yang, A Lei, KA Tanaka, and R Kodama. Plasma channeling by multiple short-pulse lasers. *Laser and particle beams*, 27(1):109, 2009.

[96] L Yin, BJ Albright, BM Hegelich, and JC Fernández. GeV laser ion acceleration from ultrathin targets: The laser break-out afterburner. *Laser and particle beams*, 24(2):291, 2006.

[97] BC Stuart, MD Feit, S Herman, AM Rubenchik, BW Shore, and MD Perry. Nanosecond-to-femtosecond laser-induced breakdown in dielectrics. *Physical review B*, 53(4):1749, 1996.

[98] X Lu, Q Liu, Z Liu, S Sun, P Ding, B Ding, and B Hu. Measurement of nonlinear refractive index coefficient using emission spectrum of filament induced by gigawatt-femtosecond pulse in BK7 glass. *Applied optics*, 51(12):2045, 2012.

[99] PP Pronko, PA VanRompay, C Horvath, F Loesel, T Juhasz, X Liu, and G Mourou. Avalanche ionization and dielectric breakdown in silicon with ultrafast laser pulses. *Physical review B*, 58(5):2387, 1998.

[100] JWS Rayleigh. *The theory of sound*. Macmillan, New York, 1896.

[101] P Beckmann and A Spizzichino. *Scattering of electromagnetic radiation from rough surfaces*. Franklin Book Co., New York, 1963.

[102] N Pinel, C Bourlier, and J Saillard. Degree of roughness of rough layers: Extensions of the rayleigh roughness criterion and some applications. *Progress in electromagnetics research B*, 19:41, 2010.

[103] GJ Pert. Inverse bremsstrahlung in strong radiation fields at low temperatures. *Physical review E*, 51(5):4778, 1995.

[104] SJ Gitomer, RD Jones, F Begay, AW Ehler, JF Kephart, and R Kristal. Fast ions and hot electrons in the laser–plasma interaction. *Physics of fluids*, 29(8):2679, 1986.

[105] WL Kruer. *The physics of laser plasma interactions*. Addison-Wesley, New York, 1988.

[106] RL Martin. The ion beam compressor for pellet fusion. *Transactions on nuclear science*, 22(3):1763, 1975.

[107] M Temporal, JJ Honrubia, and S Atzeni. Numerical study of fast ignition of ablatively imploded deuteriumtritium fusion capsules by ultra-intense proton beams. *Physics of plasmas*, 9(7):3098, 2002.

[108] S Atzeni, M Temporal, and JJ Honrubia. A first analysis of fast ignition of precompressed ICF fuel by laser-accelerated protons. *Nuclear fusion*, 42(3):L1, 2002.

[109] MJV Streeter, PS Foster, FH Cameron, M Borghesi, C Brenner, DC Carroll, E Divall, NP Dover, B Dromey, P Gallegos, JS Green, S Hawkes, CJ Hooker, S Kar, P McKenna, SR Nagel, Z Najmudin, CAJ Palmer, R Prasad, KE. Quinn, PP Rajeev, APL Robinson, L Romagnani, J Schreiber, C Spindloe,

S Ter-Avetisvan, O Tresca, M Zepf, and D Neely. Relativistic plasma surfaces as an efficient second harmonic generator. *New journal of physics*, 13(2):023041, 2011.

[110] M Nakatsutsumi, A Kon, S Buffechoux, P Audebert, Fuchs J, and R Kodama. Fast focusing of short-pulse lasers by innovative plasma optics toward extreme intensity. *Optics letters*, 35(13):2314, 2010.

[111] J Badziak, S Borodziuk, T Pisarczyk, T Chodukowski, E Krousky, K Masek, J Skala, J Ullschmied, and Yong-Joo Rhee. Highly efficient acceleration and collimation of high-density plasma using laser-induced cavity pressure. *Applied physics letters*, 96(25):251502, 2010.

[112] J Badziak, S Jablonski, T Pisarczyk, P Raczka, E Krousky, R Liska, M Kucharik, T Chodukowski, Z Kalinowska, P Parys, M Rosinski, S Borodziuk, and J Ullschmied. Highly efficient accelerator of dense matter using laser-induced cavity pressure acceleration. *Physics of plasmas*, 19(5):051305, 2012.

[113] J Raczka and J Badziak. A simple model for cavity-enhanced laser-driven ion acceleration from thin foil targets. *CoRR*, 1205.3670, 2012.

[114] O Lundh, F Lindau, A Persson, C-G Wahlström, P McKenna, and D Batani. Influence of shock waves on laser-driven proton acceleration. *Physical review E*, 76(2):026404, 2007.

[115] L Robson, PT Simpson, RJ Clarke, KWD Ledingham, F Lindau, O Lundh, T McCanny, P Mora, D Neely, CG Wahlström, M Zepf, and P McKenna. Scaling of proton acceleration driven by petawatt-laserplasma interactions. *Nature physics*, 3:58, 2007.

[116] J Schreiber, F Bell, F Grüner, U Schramm, M Geissler, M Schnürer, S Ter-Avetisyan, BM Hegelich, J Cobble, E Brambrink, J Fuch, P Audebert, and D Habs. Analytical model for ion acceleration by high-intensity laser pulses. *Physical review letters*, 97(4):045005, 2006.

[117] M Roth, A Blazevic, M Geissel, T Schlegel, TE Cowan, M Allen, J-C Gauthier, P Audebert, J Fuchs, J Meyer-ter Vehn, M Hegelich, S Karsch, and A Pukhov. Energetic ions generated by laser pulses: A detailed study on target properties. *Physical review special topics-accelerators and beams*, 5(6):061301, 2002.

[118] P McKenna, F Lindau, O Lundh, DC Carroll, RJ Clarke, KWD Ledingham, T McCanny, D Neely, APL Robinson, L Robson, PT Simpson, C-G Wahlström, and M Zepf. Low-and medium-mass ion acceleration driven by petawatt laser plasma interactions. *Plasma physics and controlled fusion*, 49(12B):B223, 2007.

[119] P McKenna, KWD Ledingham, JM Yang, L Robson, T McCanny, S Shimizu, RJ Clarke, D Neely, K Spohr, R Chapman, RP Singhal, K Krushelnick, MS Wei, and PA Norreys. Characterization of proton and heavier ion acceleration in ultrahigh-intensity laser interactions with heated target foils. *Physical review E*, 70(3):036405, 2004.

[120] R Nuter, L Gremillet, P Combis, M Drouin, E Lefebvre, A Flacco, and V Malka. Influence of a preplasma on electron heating and proton acceleration in ultraintense laser-foil interaction. *Journal of applied physics*, 104(10):103307, 2008.

[121] Y Sentoku, VY Bychenkov, K Flippo, A Maksimchuk, K Mima, G Mourou, ZM Sheng, and D Umstadter. High-energy ion generation in interaction. of short laser pulse with high-density plasma. *Applied physics B*, 74(3):207, 2002.

[122] P Audebert, R Shepherd, KB Fournier, O Peyrusse, D Price, R Lee, P Springer, JC Gauthier, and L Klein. Heating of thin foils with a relativistic-intensity short-pulse laser. *Physical review letters*, 89(26):265001, 2002.

[123] Y Sentoku, AJ Kemp, R Presura, MS Bakeman, and TE Cowan. Isochoric

heating in heterogeneous solid targets with ultrashort laser pulses. *Physics of plasmas*, 14(12):122701, 2007.

[124] CM Brenner, JS Green, APL Robinson, DC Carroll, B Dromey, PS Foster, S Kar, YT Li, K Markey, C Spindloe, MJV Streeter, M Tolley, CG Wahlström, MH Xu, M Zepf, P McKenna, and D Neely. Dependence of laser accelerated protons on laser energy following the interaction of defocused, intense laser pulses with ultra-thin targets. *Laser and particle beams-pulse power and high energy densities*, 29(3):345, 2011.

[125] F Lindau, O Lundh, A Persson, P McKenna, K Osvay, D Batani, and CG Wahlström. Laser-accelerated protons with energy-dependent beam direction. *Physical review letters*, 95(17):175002, 2005.

[126] TE Cowan, J Fuchs, H Ruhl, A Kemp, P Audebert, M Roth, R Stephens, I Barton, A Blazevic, E Brambrink, J Cobble, J Fernández, JC Gauthier, M Geissel, M Hegelich, J Kaae, S Karsch, GPL Sage, S Letzring, M Manclossi, S Meyroneinc, A Newkirk, H Pepin, and N Renard-LeGalloudec. Ultralow emittance, multi-MeV proton beams from a laser virtual-cathode plasma accelerator. *Physical review letters*, 92(20):204801, 2004.

[127] SP Narsh. *Lasl shock Hungoniot data*, volume 5. University of California Press, 1980.

[128] WJ Nellis, AC Mitchell, and AK McMahan. Carbon at pressures in the range 0.1-1 TPa (10 Mbar). *Journal of applied physics*, 90(2):696, 2001.

[129] CW Greeff and MJ Graf. Lattice dynamics and the high-pressure equation of state of Au. *Physical review B*, 69(5):054107, 2004.

[130] M Schollmeier, M Roth, A Blazevic, E Brambrink, JA Cobble, JC Fernández, KA Flippo, DC Gautier, D Habs, K Harres, BM Hegelich, T Heßling, DHH Hoffmann, S Letzring, F Nürnberg, G Schaumann,

J Schreiber, and K Witte. Laser ion acceleration with micro-grooved targets. *Nuclear instruments and methods in physics research section A: accelerators, spectrometers, detectors and associated equipment*, 577(1):186, 2007.

[131] DA MacLellan, DC Carroll, RJ Gray, N Booth, B Gonzalez-Izquierdo, HW Powell, GG Scott, D Neely, and P McKenna. Fast electron transport patterns in intense laser-irradiated solids diagnosed by modeling measured multi-MeV proton beams. *Laser and particle beams*, 31(3):475, 2013.

[132] P McKenna, APL Robinson, D Neely, MP Desjarlais, DC Carroll, MN Quinn, XH Yuan, CM Brenner, M Burza, M Coury, P Gallegos, Gray RJ, Lancaster KL, YT Li, XX Lin, O Tresca, and Wahlström CG. Effect of lattice structure on energetic electron transport in solids irradiated by ultraintense laser pulses. *Physical review letters*, 106(18):185004, 2011.

[133] DA MacLellan, DC Carroll, RJ Gray, N Booth, Matthias Burza, MP Desjarlais, F Du, B Gonzalez-Izquierdo, D Neely, HW Powell, APL Robinson, DR Rusby, GG Scott, XH Yuan, CG Wahlström, and McKenna P. Annular fast electron transport in silicon arising from low-temperature resistivity. *Physical review letters*, 111(9):095001, 2013.

[134] MN Quinn, DC Carroll, XH Yuan, M Borghesi, RJ Clarke, RG Evans, J Fuchs, P Gallegos, L Lancia, K Quinn, APL Robinson, L Romagnani, G Sarri, C Spindloe, PA Wilson, D Neely, and P McKenna. On the investigation of fast electron beam filamentation in laser-irradiated solid targets using multi-MeV proton emission. *Plasma physics and controlled fusion*, 53(12):124012, 2011.

[135] A Macchi, F Cornolti, F Pegoraro, TV Liseikina, H Ruhl, and VA Vshivkov. Surface oscillations in overdense plasmas irradiated by ultrashort laser pulses. *Physical review letters*, 87(20):205004, 2001.

[136] Y Sentoku, K Mima, S Kojima, and H Ruhl. Magnetic instability by the

relativistic laser pulses in overdense plasmas. *Physics of plasmas*, 7(2):689, 2000.

[137] J Metzkes, T Kluge, K Zeil, M Bussmann, SD Kraft, TE Cowan, and U Schramm. Experimental observation of transverse modulations in laser-driven proton beams. *New journal of physics*, 16(2):023008, 2014.

[138] F Califano, F Pegoraro, and SV Bulanov. Spatial structure and time evolution of the Weibel instability in collisionless inhomogeneous plasmas. *Physical review E*, 56(1):963, 1997.

[139] A Diaw and P Mora. Thin-foil expansion into a vacuum with a two-temperature electron distribution function. *Physical review E*, 86(2):026403, 2012.

[140] AR Bell and RJ Kingham. Resistive collimation of electron beams in laser-produced plasmas. *Physical review letters*, 91(3):035003, 2003.

[141] MS Murillo, J Weisheit, SB Hansen, and MWC Dharma-Wardana. Partial ionization in dense plasmas: Comparisons among average-atom density functional models. *Physical review E*, 87(6):063113, 2013.

[142] YT Lee. A model for ionization balance and l-shell spectroscopy of non-lte plasmas. *Journal of quantitative spectroscopy and radiative transfer*, 38(2):131, 1987.

[143] JR Rydberg. On the structure of the line-spectra of the chemical elements. *The London, Edinburgh, and Dublin philosophical magazine and journal of science*, 29(179):331, 1890.

[144] G Woan. *The Cambridge handbook of physics formulas*. Cambridge University Press, 2000.

[145] FL Zheng, SZ Wu, H Zhang, TW Huang, MY Yu, CT Zhou, and XT He. Preplasma effects on the generation of high-energy protons in ultraintense laser interaction with foil targets. *Physics of plasmas*, 20(12):123105, 2013.

[146] RJ Gray. *On mechanisms of laser-coupling to fast electrons in ultraintense laser-solid interactions*. PhD thesis, University of Strathclyde, 2013.

[147] M Coury, DC Carroll, APL Robinson, XH Yuan, CM Brenner, M Burza, RJ Gray, MN Quinn, KL Lancaster, YT Li, XX Lin, O Tresca, CG Wahlström, D Neely, and P McKenna. Influence of laser irradiated spot size on energetic electron injection and proton acceleration in foil targets. *Applied physics letters*, 100(7):074105, 2012.

[148] M Allen, PK Patel, A Mackinnon, D Price, S Wilks, and E Morse. Direct experimental evidence of back-surface ion acceleration from laser-irradiated gold foils. *Physical review letters*, 93(26):265004, 2004.

[149] JS Green, APL Robinson, N Booth, DC Carroll, RJ Dance, RJ Gray, DA MacLellan, P McKenna, CD Murphy, D Rusby, and L Wilson. High efficiency proton beam generation through target thickness control in femtosecond laser-plasma interactions. *Applied physics letters*, 104(21):214101, 2014.

[150] K Ertel, S Banerjee, PD Mason, PJ Phillips, P Rice, S Tomlinson, C Sawyer, S Blake, C Hernandez-Gomez, JL Collier, T Davenne, M Fitton, J Hill, and A Lintern. The DiPOLE project: towards high energy, high repetition rate diode pumped lasers. *Central laser facility annual report*, 2013.

[151] T Nayuki, Y Oishi, T Fujii, K Nemoto, T Kayoiji, Y Okano, Y Hironaka, KG Nakamura, K Kondo, and K Ueda. Thin tape target driver for laser ion accelerator. *Review of scientific instruments*, 74(7):3293, 2003.

[152] AJ Mackinnon, PK Patel, RP Town, MJ Edwards, T Phillips, SC Lerner, DW Price, D Hicks, MH Key, S Hatchett, D Hey, DG Hicks, S Kar, and MH Key. Proton radiography as an electromagnetic field and density perturbation diagnostic. *Review of scientific instruments*, 75(10):3531, 2004.

[153] ES Weibel. Spontaneously growing transverse waves in a plasma due to an anisotropic velocity distribution. *Physical review letters*, 2(3):83, 1959.

[154] T Kluge, C Gutt, LG Huang, J Metzkes, U Schramm, M Bussmann, and TE Cowan. Using x-ray free-electron lasers for probing of complex interaction dynamics of ultra-intense lasers with solid matter. *Physics of plasmas*, 21(3):033110, 2014.

[155] DW Schumacher, GE Kemp, A Link, RR Freeman, and LD Van Woerkom. The shaped critical surface in high intensity laser plasma interactions. *Physics of plasmas*, 18(1):013102–1, 2011.